Master's thesis

NTNU
Norwegian University of Science and Technology
Faculty of Engineering
Department of Geoscience and Petroleum

Alena Chernyshova

An integrative modelling of the Vøring Basin to understand the observed temperature anomalies

Master's thesis in Petroleum Geosciences and Engineering
Supervisor: Kenneth Duffaut and Marco Brönner
June 2019

NTNU
Norwegian University of
Science and Technology

Alena Chernyshova

An integrative modelling of the Vøring Basin to understand the observed temperature anomalies

Master's thesis in Petroleum Geosciences and Engineering
Supervisor: Kenneth Duffaut and Marco Brönner
June 2019

Norwegian University of Science and Technology
Faculty of Engineering
Department of Geoscience and Petroleum

NTNU
Norwegian University of
Science and Technology

Abstract

Exploration wells in the Vøring Basin reveal highly varying thermal profile. High temperature and heat flow anomalies are detected at the Gjallar Ridge, on the Grønøy High and in the southern Vestfjorden Basin, while the observed temperatures at the Utgard High are significantly lower. Thermal modelling based on the well log data shows that the anomalies can not be explained by the Net-to-Gross variations within the sedimentary cover and the source of the anomalies lies in the deeper parts of the lithosphere.

Potential field modelling constrained by seismic interpretation, density and velocity studies and ocean bottom seismograph velocity profiles helps to define the crustal structure of the Vøring Basin which is divided into upper, middle and lower crust in addition to high velocity lower crustal body located at the western part of the basin. The low magnetic upper crust is interpreted to be the Caledonian metasediments and metamorphic rock of felsic composition. The middle crust, however, most likely is constituted of high grade metamorphic granitoid rocks of Precambrian age. The lower crust and the lower crustal body are interpreted as high grade older mafic to ultramafic rocks, with numerous igneous intrusions and significant eclogite content in the last one. Correlating these crustal units with the rocks discovered onshore helps to define reasonable thermal parameters and perform the thermal modelling of the deeper layers. Resulting temperature and heat flow profiles indicate that compositional variations across the basement and the lower crust can not explain the thermal deviations. However, this opinion can be debated if the upper and middle crust is proven to contain large amounts of granitoid rocks with exceptional radioactive properties. Nevertheless, the current study leads to the conclusion that temperature and heat flow trends across the Vøring Basin are likely to be related to the LAB position and a possible mantle anomaly below the Lofoten-Vestfjørden segment observed from S-wave traveltime tomography.

Sammendrag

Letebrønner i Vøringbassenget avslører svært varierende termisk profil. Høye temperatur- og varmestrømavvik er oppdaget på Gjallarryggen, Grønøyhøyden og i Vestfjordenbassenget, mens observerte temperaturer på Utgardhøyden er betydelig lavere. Termisk modellering basert på brønnloggdataene viser at anomalier ikke kan forklares med Net-to-Gross variasjoner i sedimentene, og at kilden til anomaliene ligger i de dypere delene av litosfæren.

Gravimetrisk og magnetisk modellering avgrenset med seismisk tolkning, tetthets- og hastighetsstudier og seismografiske hastighetsprofiler hjelper til å definere skorpestrukturen i Vøringbassenget. Skorpe er delt inn i øvre, midtre og nedre deler i tillegg til et høyhastighets nedre legeme lokalisert ved den vestlige delen av bassenget. Den lavmagnetiske øvre skorpen tolkes som Kaledonske metasedimeter og felsiske metamorfe bergarter. Den midterste skorpen består imidlertid av høy-grad metamorfe granittiske bergarter av Prekambrisk alder. Den nederste skorpen er tolket som høy grad eldre mafiske og ultramafiske bergarter, med betydelig eklogittinnhold i den siste. Korrelering av disse skorpedelene med bergarter som finnes på land, hjelper med å definere termiske parametre og lage en termisk modell av de dype lagene. Resulterende temperatur- og varmestrømsprofiler indikerer at komposisjonelle variasjoner i skorpen kan ikke forklare de termiske anomaliene. Likevel kan denne teorien bestrides dersom den øvre og midtre skorpen inneholder store mengder av granittiske bergarter med eksepsjonelle radioaktive egenskaper. Denne studien konkluderer likevel med at temperatur- og varmestrømsprofilene over Vøringbassenget vil være relatert til posisjonen til grensen mellom litosfæren og astenosfæren og en mulig mantelanomali under Lofoten-Vestfjørden-segmentet observert fra S-bølge gangtid tomografi.

Acknowledgement

I owe my deep and sincere gratitude to my supervisors Kenneth Duffaut, Associate Professor at the Norwegian University of Science and Technology, and Marco Brönner, Geophysics Team Leader at the Geological Survey of Norway and Associate Professor at the Norwegian University of Science and Technology, for inspiring me to work on this interdisciplinary and wide topic, patiently guiding me trough the process, and sharing with me their broad experience and knowledge through many extensive discussions. I also would like to extend my gratitude to Dicky Harishidayat, PhD Candidate at the Norwegian University of Science and Technology, for assisting me with gathering all the necessary data. In addition to that, I want to thank Geophysics Team at the Geological Survey of Norway and especially Senior Geophysicist Laurent Gernigon for answering all the possible questions I had and many long and fruitful discussions.

This projects would not be possible without several geophysical and petrophysical datasets made available to me. I would like to thank Norwegian Petroleum Directorate - DISKOS database, Schlumberger PETREL READY Database and NTNU - Department of the Geoscience and Petroleum for providing me with the well and seismic data and giving me the access to all the nessesary software packages. I also would like to thank the Geological Survey of Norway for sharing with me the gravity, magnetic and petrophysical data and providing me with an office space and the essential software licences.

Last but not least, I would like to thank my family for giving me the opportunity and motivation to pursue a Master's Degree in Norway and supporting me through many years of my studies.

Alena Chernyshova
11.06.2019

Table of Contents

List of Tables

List of Figures

Abbreviations

BCU	=	Base Cretaceous Unconformity
COB	=	continent-ocean boundary
DDMS	=	depth to deepest magnetic source
DGRF	=	Definitive Magnetic Reference Field
FFT	=	fast Fourier transform
Fm	=	formation
HF	=	heat flow
HVLC	=	high velocity lower crust
IGRF	=	Internal Geomagnetic Reference Field
LAB	=	lithosphere–asthenosphere boundary
MD RKB	=	measured depth below rotary table
MDSS	=	measured depth sub-sea
MOHO	=	Mohorovičić discontinuity
NCS	=	Norwegian continental shelf
NGU	=	Norges Geologiske Undersøkelse (Geological Survey of Norway)
NPD	=	Norwegian Petroleum Directorate
OBS	=	ocean bottom seismograph
ODP	=	Ocean Drilling Program
RMS	=	root mean square
SDR	=	seaward dipping reflectors
TCU	=	Top Cenomanian Unconformity
TD	=	total depth
TG	=	temperature gradient
TOC	=	total organic content

Chapter 1

Introduction

Understanding subsurface temperatures is crucial for petroleum industry. In order to make viable predictions of potential prospects, current and past temperatures within a basin need to be estimated. Being subjected to certain temperature and pressure over a long time window, source rocks are enabled to generate oil and gas in quantities large enough to fill existing reservoirs and result in very profitable production. In this case, temperature can be used to predict whether a rock is mature enough and whether it is generating oil, condensate or dry gas, but also to make a conclusion on the presence of producible hydrocarbons versus carbon residue. In addition to that, temperature has a profound effect on reservoir fluid properties and quality of a seal. Temperature influenced processes, such as fault reactivation, can influence seal integrity (Urpi et al., 2017).

Moreover, thermal state of a basin is related to tectonic history. High temperatures can indicate recent mafic intrusions, magmatic underplating or continental rifting. Furthermore, knowing properties of materials, certain geotherms are used to reveal important geological interfaces, such as lithosphere-asthenosphere boundary (LAB) (Beardsmore and Cull, 2001).

When working with the well data from the Vøring Basin, it becomes evident that there are several areas with remarkable temperature anomalies. Those include the Gjallar Ridge with an average temperature gradient (TG) above 50 °C/km for wells 6704/12-1 and 6604/2-1 and southern Vestfjørden Basin and adjacent Grønøy High with a gradient of 40 °C/km for wells 6610/2-1S and 6610/3-1R, while the remaining wells in the basin show values below 40 °C/km. As thermal gradient is correlated with basal heat flow (HF), radiogenic heat production within crust and thermal conductivity of rocks according to conductive heat equation (Chapter 2), studying effects of each of those variables becomes an important step towards understanding the thermal state of the Vøring Basin.

At the same time, the Vøring Basin remains rather unexplored when compared to neighbouring Trøndelag Platform and adjacent terraces. Many exploration wells failed to confirm a working play model: even though there are several wells verifying the presence of good reservoir rock, no producing source rocks have been detected (Brekke et al., 1999). This is challenged by complex tectonic and thermal history of the basin. While the

first issue has been addressed by many researchers such as Skogseid et al. (1992), Brekke (2000) and Gernigon et al. (2004), the second matter has been bypassed.

A few studies can be found, which analyze the heat flow across the Vøring Basin and the Norwegian continental shelf (NCS). Pascal (2015) offers heat flow estimations for 63 exploration wells located in the Norwegian Sea, the North Sea and the Barents Sea. The resulting surface heat flow map covers the whole NCS from the Norwegian North Sea and towards the Barents Sea, which is very valuable data for petroleum sector. However, no wells west of the Trøndelag Platform and its terraces have been considered. Another extensive research done by Ritter et al. (2004) presents surface heat flow estimates in the Vøring Basin and discusses several potential factors affecting these values. As a part of original data, the authors include both shallow probe measurements and deep well data. Wells included in the research are located on the eastern part of the basin, while shallow probe measurements are scattered west of 8°E parallel and are subjected to a high degree of uncertainty. Both papers reveal a heat flow trend across the area: surface heat flow is lowest above the deepest parts of the basin and elevated at the highs. In addition to that, Ritter et al. (2004) build a heat flow profile along the section stretching from northern part of the Vøring Escarpment and towards the edge of the Trøndelag Platform. While trying to match the observed profile, they test several scenarios making assumptions regarding heat generated within the crust. Even though the trend is confirmed, several measurements remain anomalous. Moreover, neither of authors addresses the thermal anomalies at the Gjallar Ridge or the Grønøy High specifically, which are important puzzles for the full thermal picture of the Vøring Basin.

On the other hand, Maystrenko and Gernigon (2018) and Maystrenko et al. (2018b) present 3D thermal models of the Vøring and Møre basins and the Lofoten-Vesterålen area. According to these models thermal anomalies are likely to be controlled by shallowing of the LAB towards the oceanic domain and a mantle anomaly below the Lofoten region, as well as complex erosional-depositional patterns. However some substantial misfits with the well temperatures are observed. Those are explained with possible fluid convection or advection, the effect of which is hard to model and validate.

Even though heat flow is an important variable correlated with thermal gradient, other factors may contribute. Varying thermal conductivity as a consequence of lithological change has a direct effect on temperature gradient. Given same surface heat flow, a decrease in thermal conductivity from one area to another will result in elevated gradient. At the same time, surface heat flow is a complex variable incorporating mantle heat flow and heat produced by radiogenic components within sediment column and crustal layers. All those factors play important part in framing thermal state of a basin and the main goal of the Specialization Project (Chernyshova, 2018) was to evaluate the importance of each of those. Thermal modelling based on the well data from the area shows that thermal conductivity and radiogenic heat produced in sediments do not impose a primary effect. On the contrary, trends in mantle and crustal heat production represent a principal cause for temperature variation across the basin: at the points of rising thermal gradient, projected top basement heat flow also increases. In this way, a key for understanding temperature deviations across the Vøring Basin is finding the reasons behind crustal and mantle heat flow anomalies.

In order to do that, crustal model of the section across the Vøring Basin is created in

Geosoft software based on magnetic and free air gravity data from Olesen et al. (2010c) and Olesen et al. (2010b). As potential field modelling involves high degree of ambiguity, the model is integrated with seismic interpretation of main stratigraphic boundaries along the composite seismic line. Furthermore, crustal boundaries are constrained with ocean bottom seismograph (OBS) profiles. Density trends inferred from well logs serve as an input for the modelling, and are based on statistical analysis of main sediment packages. As a next step, characteristics of the modelled basement rocks are correlated with onshore basement in order to determine basement type and its thermal features, namely radiogenic heat generation and thermal conductivity. The properties of deep sediments not logged by the wells are extrapolated to the top basement surface. This allows to extend the thermal modelling to deeper levels and establish whether heat generated within the basement rocks can explain existing temperature anomalies in the Vøring Basin. In addition to that, modelled temperatures are correlated with Curie depth point derived from magnetic data.

The project is structured in a conventional way in order to make the report easy to follow and understand. Chapter 2 covers the theoretical background of the project together with geology of the area and theories regarding deep crustal structures in order to give a reader a critical view on the ambivalence concerning geological development of the Vøring Basin. Chapter 3 focuses on methodology and workflow. Chapters 4 summarizes the potential field modelling results, while Chapter 5 discusses the model's geological concepts and the thermal modelling outcome. Chapter 6 presents the conclusion as well as recommendations for further work.

Chapter 2

Background

2.1 Theoretical Background

2.1.1 Potential Field Theory

Gravity Field

The basis of the gravity method is Newton's Law of Universal Gravitation which describes the force of attraction between two bodies (Hinze et al., 2013):

$$F = G\frac{m_1 m_2}{r^2}, \tag{2.1}$$

where F is force in $[\mathrm{N}]$, G is gravitational constant ($6.67 \times 10^{-11}[\mathrm{Nm}^2/\mathrm{kg}^2]$), m_1 and m_2 are masses in $[\mathrm{kg}]$ and r is the distance between the two masses in $[\mathrm{m}]$.

Gravitational acceleration is derived from this formula and represents the force of attraction experienced by a unit mass in the presence of a bigger mass:

$$g = G\frac{m}{r^2}, \tag{2.2}$$

where g is gravitational acceleration in $[\mathrm{m/s}^2]$ and m is a larger mass in $[\mathrm{kg}]$.

Gravimetry, consequently, is focused on measuring the gravitational acceleration, which reflects mass of the objects within the Earth's interior. However, in order to use measured signal to model crustal densities it is important to perform several corrections. The first step includes removing the theoretical gravity which is calculated in accordance with International Gravity Formula based on the Earth's ellipsoidal shape (Hinze et al., 2013):

$$g_\theta = 978.032677[\frac{1 + 0.0019131851353sin(\theta)^2}{\sqrt{1 - 0.0066943800229sin(\theta)^2}}] \tag{2.3}$$

where g_θ is gravitational acceleration in $[\mathrm{gal}]$ and θ is latitude.

As theoretical gravity is calculated at the sea level, the next step involves adjusting for the distance between the sea level and the datum. The resulting correction is called the Free Air correction (Hinze et al., 2013):

$$g_h = 0.03086h \tag{2.4}$$

where g_h is gravitational acceleration in $[\mathrm{mGal}]$ and h is height above the datum in $[\mathrm{m}]$.

It is important to note that there are several other corrections which can be applied, including Bouguer correction which accounts for the rock mass between the sea level and the datum, or less common corrections for tides and Eötvös effect. However, as the area of interest is located offshore, it is common to confine to Free Air corrected anomaly for the modelling.

Magnetic Field

Magnetic theory is based on the interaction between the Earth's magnetic field and magnetic materials in the subsurface. Earth's magnetic field exists due to electromagnetic currents of iron particles in the Earth's liquid outer core (Hinze et al., 2013). In addition to that, there is an external magnetic field created as the charged particles emitted from the Sun interact with Earth's internal magnetic field. Magnetic field is represented by the strength parameter H, while parameter B describes the induced magnetic field which depends on the properties of the material.

B is derived from Coulomb's law which defines magnitude of magnetic force between two point magnetic poles (Hinze et al., 2013):

$$F = C_m \frac{p_1 p_2}{r^2}, \tag{2.5}$$

where F is force in $[\mathrm{N}]$, C_m is Coulomb constant (equal to $\mu_0/4\pi$, $\mu_0 = 4\pi \times 10^{-7}[\mathrm{H/m}]$), p_1 and p_2 are point magnetic poles of strength p in $[\mathrm{Am}]$, and r is distance between them in $[\mathrm{m}]$.

B, in this case, is similar to g in Newton's law and represents magnetic force experienced by a unit pole in the presence of a stronger pole:

$$B = C_m \frac{p}{r^2}, \tag{2.6}$$

where B is magnetic induction in $[\mathrm{T}]$ and p is magnetic pole strength in $[\mathrm{Am}]$.

At the same time, the relationship between B and H is defined by the following formula:

$$B = \mu H, \tag{2.7}$$

where μ is magnetic permeability in $[\mathrm{H/m}]$ and H is Magnetic Field Strength in $[\mathrm{A/m}]$.

Furthermore, B can be expressed in terms of magnetization M, which is dependent on magnetic susceptibility of material χ (Hinze et al., 2013):

$$B = \mu H = \mu_r \mu_0 H = (1 + \chi)\mu_0 H = \mu_0 H + \mu_0 \chi H = \mu_0 H + \mu_0 M, \tag{2.8}$$

where μ_r is relative magnetic permeability, μ_0 is magnetic permeability in vacuum ($4\pi \times 10^{-7}[\mathrm{H/m}]$), χ is magnetic susceptibility and M is magnetization in $[\mathrm{A/m}]$.

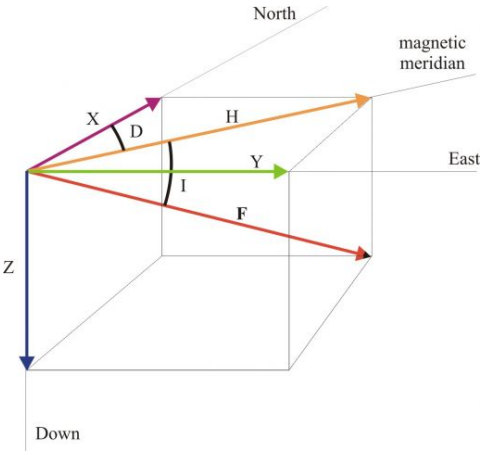

Figure 2.1: Inclination and declination after National Institute of Geophysics and Volcanology in Italy/Instituto Nazionale di Geofisica e Vulcanologia (2019). F shows magnetic field's direction, while I and D define inclination and declination.

Parameter χ is related to ability of a body to be magnetized. Magnetization is described by orientation of magnetic moments of material's elementary particles in a presence of external magnetic field. Depending on type of this material, magnetic moments can be aligned in different ways relative to the magnetic field. On this basis magnetic materials can be classified as paramagnetic, ferromagnetic, diamagnetic or ferrimagnetic (Hinze et al., 2013). Ferrimagnetic materials have adjacent magnetic moments oriented in opposite directions, however, unequal amounts result in one direction net magnetic moment parallel to the field. The most common magnetic material is magnetite, which has ferrimagnetic origin.

Magnetic surveys measure magnetic induction B, which is varying spatially due to variation in magnetization within the subsurface. Magnetization has two components: induced and remanent. Remanent magnetization represents a phenomena when a rock retains alignment of magnetic moments since the time the Earth's magnetic field was oriented differently (Hinze et al., 2013). Orientation of magnetic field is described by inclination and declination (Figure 2.1), which are important parameters affecting anomalies. On a geological time scale magnetic reversals occur rather often, and can be studied on the rocks of spreading ocean floors (McElhinny and McFadden, 1999).

The recorded magnetic signal is affected by the Earth's core field, external field and crustal field. In order to resolve the information about subsurface, the anomaly field needs to be corrected for the first two. Core field is modelled and removed either by Internal Geomagnetic Reference Field (IGRF) or Definitive Magnetic Reference Field (DGRF) models (Hinze et al., 2013). IGRF makes predictions for each 5 years based on ongoing satellite measurements and data from the worldwide network of geomagnetic observatories. DGRF is updated every 5 years on the basis of the actual changes since the recording of the magnetic field started and represents the more accurate version. What remains after the correction is magnetic signal of the crust and upper lithosphere down to the Curie depth, where magnetic materials loose their magnetization.

2.1.2 Spectral Method

Magnetic moments loose their specific orientations above the Curie temperature, and their magnetization becomes zero (Hinze et al., 2013). In order to calculate depth to the Curie isotherm it is possible to use spectral analysis.

Blakely (1996) defined power density spectrum of the magnetic total field:

$$\Phi(k_x, k_y) = \Phi_M(k_x, k_y) * F(k_x, k_y), \tag{2.9}$$

where Φ_M is power density spectrum of magnetization, while k_x and k_y are wavenumbers.

The Fourier transform, in this case, is represented by:

$$F(k_x, k_y) = 4\pi^2 C^2 M_d^2 G_d^2 e^{-2kz_t}(1 - e^{-k(z_b - z_t)})^2 S(a, b)^2, \tag{2.10}$$

where $k = \sqrt{k_x^2 + k_y^2}$, C is proportionality constant, M_d and G_d are factors accounting for magnetization and geomagnetic field directions, $S(a, b)$ is shape factor, z_t and z_b are depth to top and base of a magnetic source.

Assuming that magnetization is random and considering radial average of power density spectrum leads to the following simplification (Spector and Grant, 1970):

$$\Phi_{av}(k) \cong C_2 e^{-2kz_t}(1 - e^{-k(z_b - z_t)})^2, \tag{2.11}$$

where C_2 is a constant.

Taking the logarithm on both sides of Equation 2.11 and assuming medium to high wavenumbers results in linear relationship between logarithm of power density spectrum and depth to the source of magnetic anomaly, which is represented by an ensemble of blocks:

$$Ln(\Phi_{av}(k)) \cong C_2 - 2kz_t \tag{2.12}$$

According to Spector and Grant (1970) power spectrum from the deepest sources is strongest at low wavenumbers. As a consequence, measuring the slope at the smallest wavenumbers can indicate how deep the base of a magnetic source is. If the grid is large enough, this value can represent the Curie temperature depth (Spector and Grant, 1970).

2.1.3 Temperature and Heat Flow

Equations used for temperature and heat flow modelling are derived from the Fourier's law, which describes the relationship between heat flow and temperature gradient (Beardsmore and Cull, 2001):

$$Q = -k\Delta T, \tag{2.13}$$

where Q is heat flux density or heat flow in $[\mathrm{W/m^2}]$, k is thermal conductivity in $[\mathrm{W/(m^\circ C)}]$ related to ability of a material to conduct the heat, and T is temperature in $[^\circ\mathrm{C}]$.

This relationship is only valid for homogeneous media and fixed thermal boundaries. In case of unsteady state heat conduction Equation 2.13 can be transformed to the following form (Beardsmore and Cull, 2001):

$$\frac{\partial T}{\partial t} = \kappa \times \nabla T, \tag{2.14}$$

where $\kappa = k/(c \times \rho)$, while c is specific heat capacity in $[\mathrm{J/K}]$ and ρ is density in $[\mathrm{kg/m^3}]$.

Assuming that heat can be produced internally and considering 1D case, Equation 2.14 takes form of:

$$\frac{\partial T}{\partial t} = \kappa \times (\frac{\partial^2 T}{\partial^2 z}) + \frac{A}{\rho c}, \tag{2.15}$$

where A is radiogenic heat production in $[\mathrm{W/m^3}]$.

In steady state Equation 2.15 is equivalent to:

$$\frac{\partial^2 T}{\partial z^2} = -\frac{A}{k}. \tag{2.16}$$

With certain boundary conditions, Equation 2.16 can be used to derive formulas for temperature, temperature gradient, and heat flow profiles. Considering constant surface temperature and heatflow:

1. $T(z = 0) = T_0$,
2. $Q(z = 0) = -k\frac{\partial T}{\partial z} = -Q_0$,

equation 2.16 results the following formulas for T and $\frac{\partial T}{\partial z}$:

$$\frac{\partial T}{\partial z} = -\frac{A}{k}z + \frac{Q_0}{k}, \tag{2.17}$$

$$T = -\frac{A}{2k}z^2 + \frac{Q_0}{k}z + T_0. \tag{2.18}$$

Finally, given surface heat flow, heat profile can be modelled by:

$$Q = -Az + Q_0. \tag{2.19}$$

2.2 Study Area

The Vøring Basin is one of the two largest basins in the Norwegian Sea (Figure 2.2). It extends over 450 km in N-S direction and across 250 km in E-W direction covering latitudes from 64°N to 68°N and longitudes from 1°E to 8°E. It is bounded by the Vøring Marginal High to the west and the Trøndelag Platform to the east, while northern and southern boundaries are represented by the Bivrost Lineament and the Jan Mayen Lineament respectively.

2.2.1 Tectonic History

Roughly, geology of the Norwegian Sea can be can be traced back to three phases of tectonic development (Halland et al., 2013). In Late Silurian - Early Devonian times the region has experienced closing of the Iapetus Ocean and formation of the Caledonides. This was followed by the Caledonian collapse and numerous rifting episodes through Mesozoic era. The final phase involves opening of the North Atlantic Ocean in Early Eocene and subsequent ocean spreading until present day.

The Vøring Basin is represented by very thick Cretaceous deposits and uplifted flanks related to thermal subsidence following the major rifting episodes (Figures 2.3-2.4). Brekke

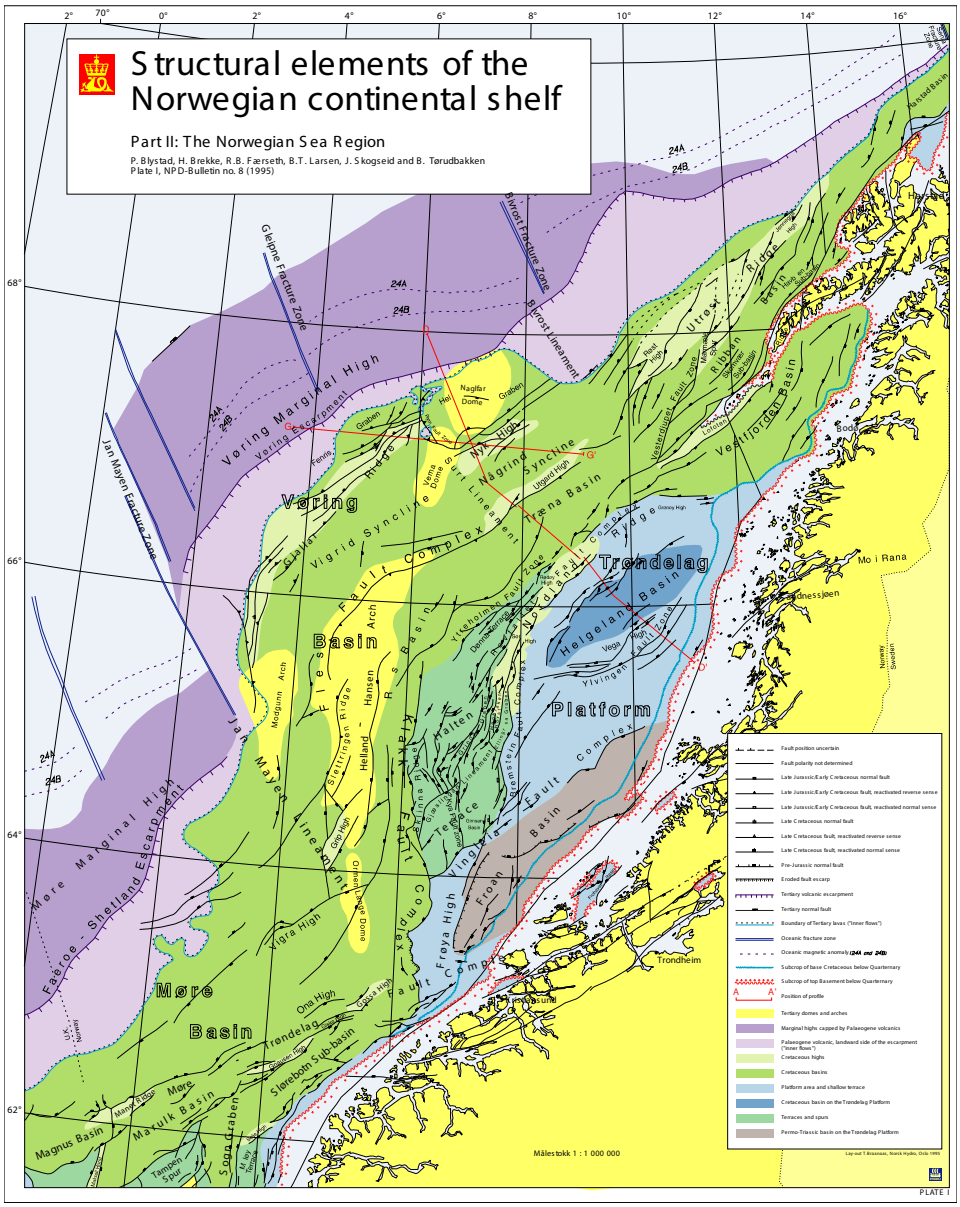

Figure 2.2: Structural elements of the Norwegian Sea modified after Blystad et al. (1995). Red lines indicate location of relevant geoseismic profiles from Blystad et al. (1995).

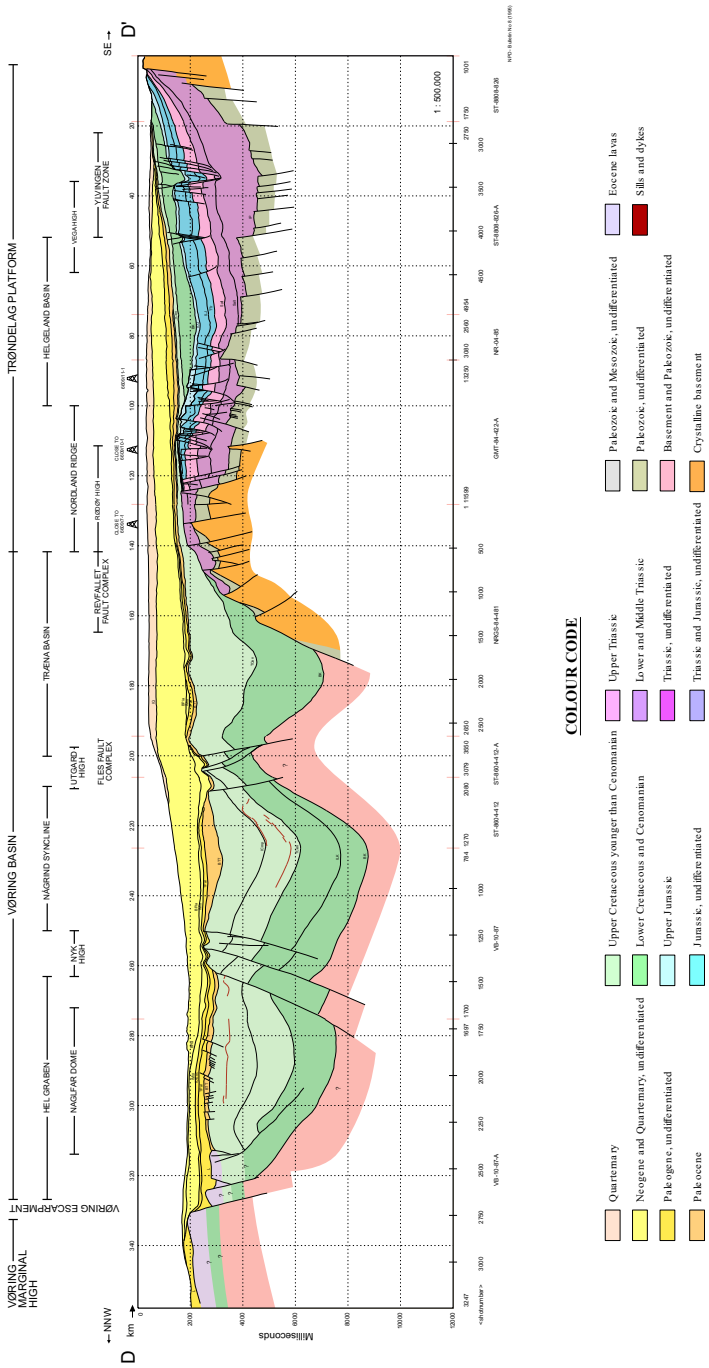

Figure 2.3: Geoseismic profile DD' across the northern Vøring Basin and the Trøndelag Platform modified after Blystad et al. (1995).

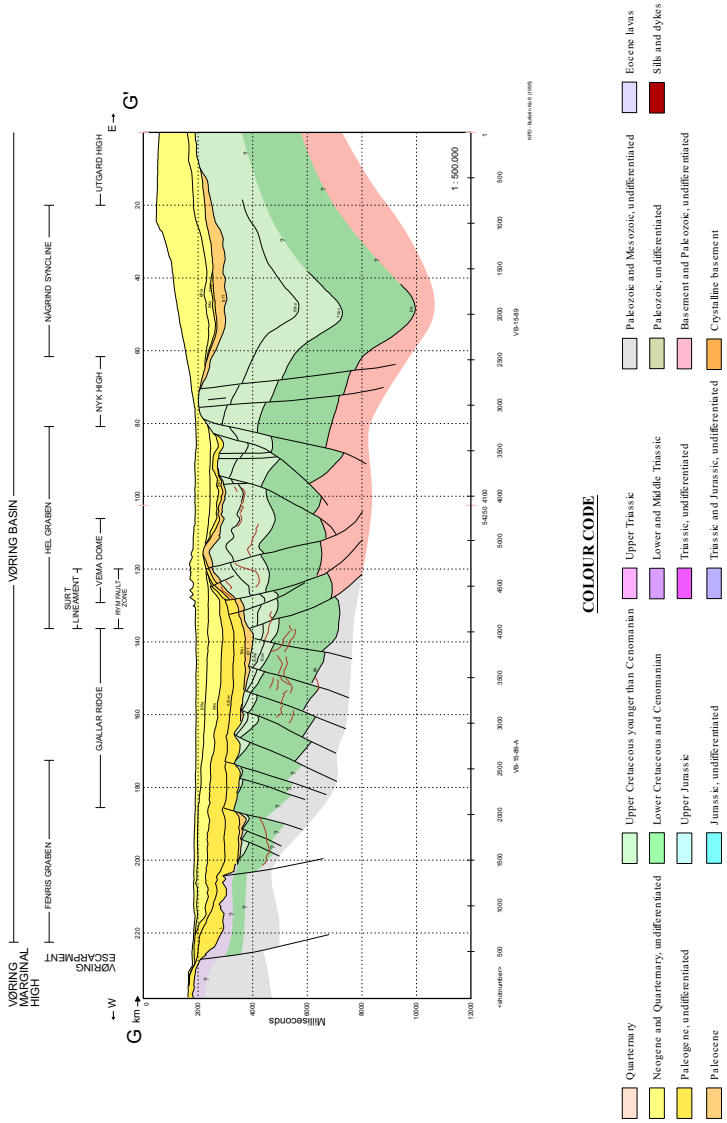

Figure 2.4: Geoseismic profile GG' across the northern Vøring Basin modified after Blystad et al. (1995).

(2000) divides the history of the Vøring Basin into three main stages: Late Middle Jurassic to Late Cenomanian, Late Cenomanian to Early Paleocene and Early Paleocene to Recent.

Following Brekke (2000) the first stage involves thermal subsidence after extensive Middle Jurassic-Early Cretaceous rifting. This led to the development of the Fles Fault Complex and substantial deposition of marine deposits in the Rås and Træna basins (Figure 2.3). Moreover, marine sediments were also deposited west of the Fles Fault Complex, where the Någrind and Vigrid synclines, the Hel Graben and the Nyk High comprised a single shallower basin (2.3-2.4). As evident from Figure 2.5, lithostratigraphically this period is related to organic rich shales of the Spekk Formation (Fm) deposited in anoxic marine environment, open marine marls and carbonates of the Lyr Fm, and claystones with thin sand and carbonate stringers of the Lange Fm (Dalland et al., 1988).

The second stage started with renewed tectonics and accelerated subsidence merging several depocentres into one basin - the Vøring Basin (Brekke, 2000). This was associated with uplift and tilt of the flanking Gjallar Ridge and the Frøya High in Late Cenomanian - Early Turonian times. Shortly after, extensive faulting occured at the Gjallar Ridge and along the western boundary of the Trøndelag Platform. During Late Cretaceous changing phases of compression and extension led to formation of main synclines and highs in the Vøring Basin, namely the Vigrid and Någrind synclines, the Træna Basin, the Nyk and Utgard highs (Figures 2.3-2.4). Post-Cenomanian Cretaceous strata contains sandstones of the Lysing Fm which can be related to submarine fan deposits and open marine claystones of the Kvitnos, Nise and Springar formations containing carbonate and sand interbeds (Dalland et al., 1988).

According to Brekke (2000) the third stage followed regional uplift at Cretaceous-Tertiary transition and resulted in erosion of the highs and deposition of Paleocene and Eocene deep marine claystones of the Tare and Tang formations (Figure 2.5). The rifting has continued and led to continental break up and formation of the Vøring Escarpment, which is related to increase in tuff content within the Tare Fm. Tectonism associated with continental separation reactivated major lineaments and faults including the Flex Fault Complex and the Surt Lineament and created the final structural picture of the Vøring Basin with the Vøring Escarpment and Teriary domes (Figures 2.2-2.4). During Eocene - Oligocene times marine claystones of the Brygge Fm were deposited across the Vøring Basin with major depocenter in the western part. These sediments were eroded by Middle Miocene submarine erosion unconformity and covered by marine claystones, siltstones and sandstones of the Kai Fm. In Pliocene times, the Vøring Basin has experienced hiatus and older deposits were downlapped by the Plio-Pleistocene Naust Fm sediments eroded from land.

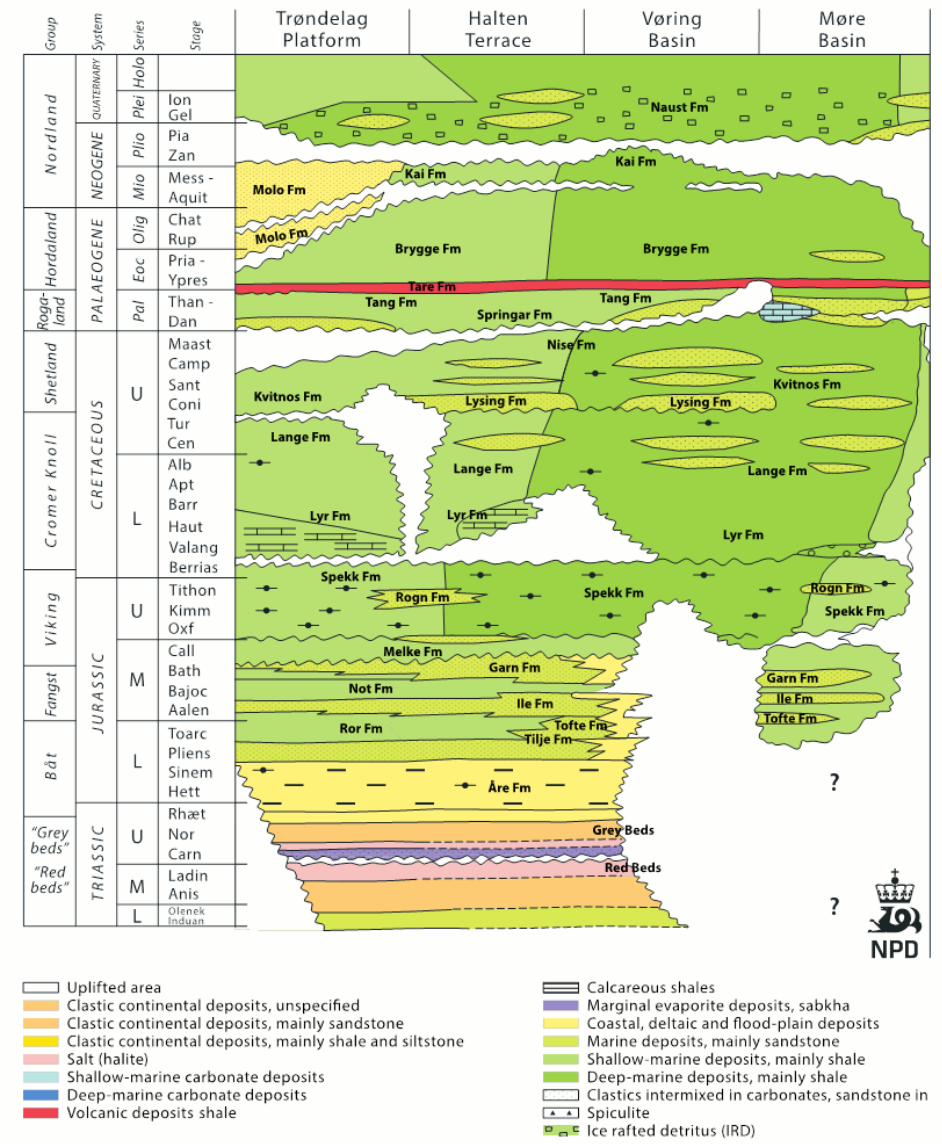

Figure 2.5: Lithostratigraphy of the Norwegian sea after the Norwegian Petroleum Directorate (Halland et al., 2013).

2.2.2 Basement Concepts

In contrast to the shallow Vøring Basin, deeper sediments and crystalline basement are poorly constrained by wells and different concepts of crustal settings are suggested.

Acquisition of OBS data in the area has helped to define crustal structure of the Vøring Basin. Based on seismic velocities, Mjelde et al. (1997) and Mjelde et al. (1998) suggest presence of the upper and lower continental crust beneath the sediments in the Vøring Basin, as well as local occurrences of a high velocity lower crustal body (HVLC). Generally, there are three main theories in regards to origin and composition of this body: underplating related to continental break-up, seprentinized peridotite or old high grade metamorphic rocks.

Mjelde et al. (2009) discuss this issue in detail and present their own interpretation. Based on the analysis of the multichannel seismic data and gravity modelling the authors have been able to split the high velocity lower crustal body into two units and provide interpretation for both. The first unit located south of the Rån Lineament has an extreme velocity above 8 km/s and is interpreted as Caledonian eclogites (Figure 2.6). The second unit with velocities above 7 km/s stretches along the whole Vøring Basin west of the Utgard High and is concluded to be mafic rocks intruded during the last episodes of rifting mixed with older continental crust.

Gernigon et al. (2004) challenge the amount of mafic materal involved in creating this lower crustal velocity and density anomaly. The authors focus specifically on the Gjallar Ridge area and combine seismic, gravity and magnetic interpretation and discuss different scenarios regarding formation and properties of HVLC. Favoured conclusion states that the body is likely to be high pressure granulites or eclogites updomed and injected by magmatic material prior to continental break-up. Ebbing et al. (2006) support this theory and claim that the lower crustal body is likely to be high-grade metamorphic rocks. Moreover, by analyzing the structure in combination with major lineaments in the area, the authors agree that the body could have a connection with the Caledonian root.

Recent studies reach similar verdicts. Abdelmalak et al. (2017) focuse on the regional interpretation of so-called T-reflection across the Vøring Basin which represents the top of the lower crustal high velocity body as identified by Gernigon et al. (2003). Analyzing the interpretation in conjunction with gravity, magnetic, and seismic refraction data has led to the conclusion that this body is a mixture of mafic and ultramafic rocks and older metamorphic rocks.

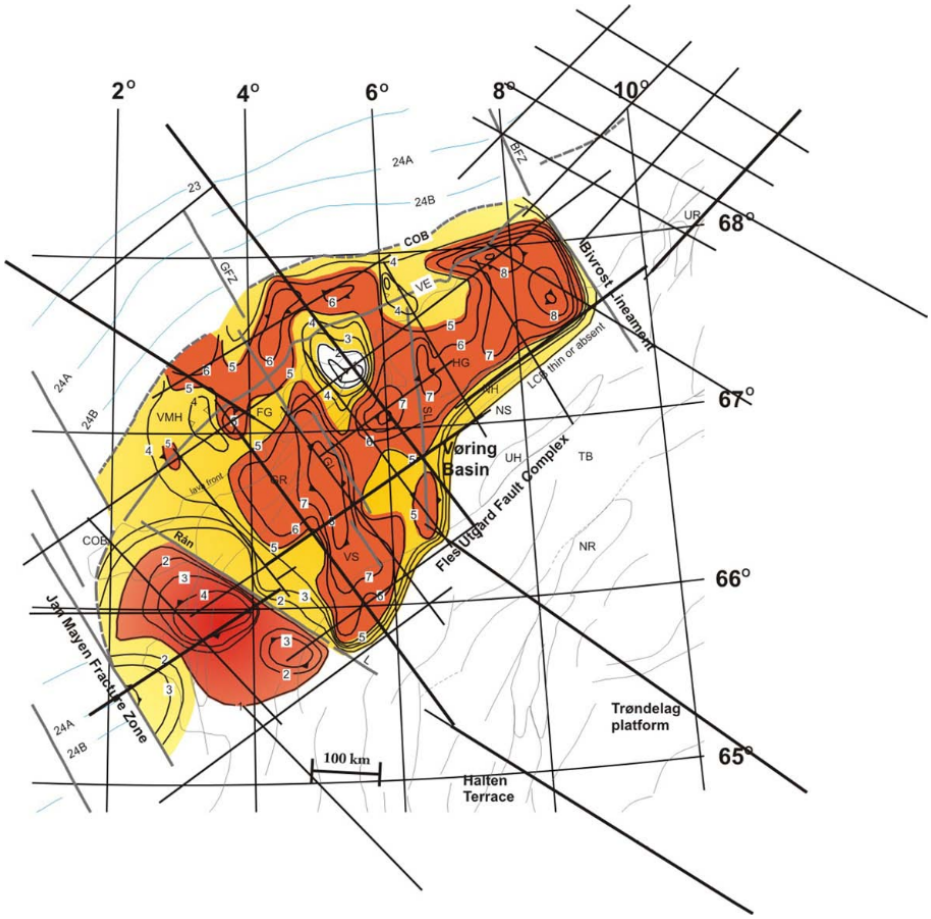

Figure 2.6: Geometry and thickness of the lower crustal body after Mjelde et al. (2009). Contours display thickness in $[\mathrm{km}]$. Red colored body south of the Rån Lineament is 8+ $[\mathrm{km/s}]$ velocity layer, while the remaining part represents 7+ $[\mathrm{km/s}]$ velocity unit.

Chapter 3

Methodology

Essentially, the methodology consists of 8 consequent steps presented below:

1. Revision of top basement surface interpretation based on additional seismic lines and wells
2. Thermal modelling of additional wells similar to Chernyshova (2018)
3. Study of density well logs to compute average density values
4. Velocity study based on check-shot data to determine average interval velocities in different units
5. Time to depth conversion of interpreted units
6. 2D modelling of gravity data
7. 2D magnetic modelling and Curie depth estimation
8. Modelling of temperature and heat flow profiles from the seabed to the Mohorovičić discontinuity (MOHO)

Subsequent sections describe some of these steps in detail.

3.1 Seismic Interpretation

Thermal analysis done in Chernyshova (2018) is implemented along the composite seismic profile composed of several reflection seismic surveys (Table 3.1). As shown on Figure 3.1 the profile is stretching from the Vøring Margin through the Gjallar Ridge, the Nyk and Utgard highs towards the Grønøy High and into the southern Vestfjørden Basin.

That study presents the interpretation of the main horizons done in Petrel software along with the thermal modelling for wells located at or close to the composite line (Table 3.2). However, the interpretation is revised in this work on the basis of several additional wells and seismic surveys (Tables 3.2-3.3).

Following that, the composite profile serves as a spacial constrain for further interpretation and thermal and potential field modelling presented here.

NPD-VB-89 line 14-89	SL99-110	SL99-114	SL99-204
SL99-209	TBS2000-114	TBS2000-128	TBS2000-201
TBS2000-202	TBS2000-211	N5-94-206	

Table 3.1: Seismic lines included in the composite line. Majority is zero phase normal polarity data, with the exception of N5-94-206 which is zero phase reverse polarity seismic.

6704/12-1	6604/2-1	6705/10-1	6605/1-1	6706/11-1	6707/10-1
6607/2-1	6607/5-2	6607/5-1	6608/2-1S	6609/7-1	6609/11-1
6610/7-1	6610/7-2	6609/5-1	6609/6-1	6610/2-1S	6610/3-1R

Table 3.2: Wells included in the project. Red color indicates wells used for the thermal modelling in Chernyshova (2018).

NRT94	N5-94	NH9706
NHE96	NPD-VB-89_PROC_WESTERN	SL99
N1N3C-94	NPD-NH-79_NPD-TR02-74	NH8102
GMNR-94	MV01RE-NPD-VRB-90-BP-R01	GVF2000
GVF2000	MV01RE-NPD-VRB-90-BP-R01	GRS98-GRS99-11
	TBS2000	

Table 3.3: Seismic surveys included in the project. Blue color indicates additional seismic data allowing better mapping of the principal horizons.

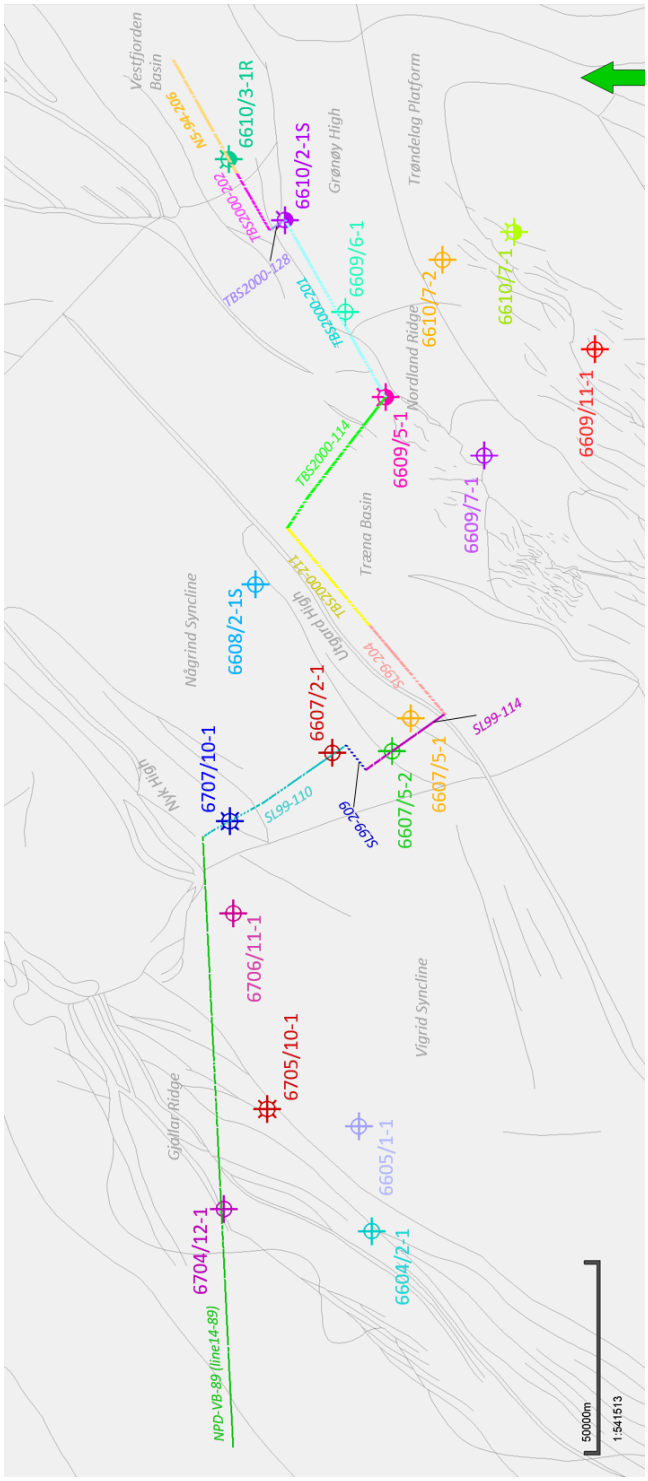

Figure 3.1: 2D Map of the composite seismic line and wells. Arrow points to North.

3.2 Potential Field Modelling

2D modelling is performed in Geosoft GM-SYS software. This is an interactive process, where gravity and magnetic responses are calculated based on user created geological model. According to GM-SYS guide (Geosoft Oasis Montaj, 2004), formulas and algorithms behind 2D modelling are introduced by Talwani et al. (1959), Talwani and Heirtzler (2010) and Won and Bevis (1987). The model is usually extended by 30000 km in both directions in order to avoid edge effects and is limited by an arbitrary depth with 50 km being the default value. In reality, the observed data cover larger and undefined volume relative to the restricted model, which leads to a natural shift between the observed and modelled signals. Therefore, a constant DC shift is applied to calculated gravity and magnetic curves, and its size can be estimated automatically from the root mean square (RMS) error.

Prior to modelling, Free Air gravity and magnetic grids extracted from Olesen et al. (2010b) and Olesen et al. (2010c) are loaded into Geosoft (Figures 3.2-3.3). Subsequently, anomaly data is sampled along the composite line extents. It is important to note that several kinks across the composite line are smoothed when extracting gravity and magnetic data, as these sharp boundaries produce some unexpected anomalies. Following that, GM-SYS allows to proceed with either time modelling or depth modelling.

When lacking good seismic velocity data the most convenient way to build a model is to start constructing interfaces in 2D time-domain and convert them to depth using assigned interval velocities. These interfaces are based on seismic interpretation loaded as a background. When interpreted surfaces are converted and cross-checked with the welltops, it is possible to add additional units as well as proceed with the modelling of deeper parts not visible to reflection seismic.

Velocities used for conversion are based on well check-shot data and reviewed in connection to values indicated by other authors (Zastrozhnov et al., 2018). Moreover, in order to constrain the model and control the conversion, velocity interfaces and their interpretation retrieved from OBS data were included. Owing to significant velocity contrasts, the crucial boundaries resolved by OBS are the sediment-basement border, top of the lower crust and the MOHO. Several profiles described by Mjelde et al. (1997), Mjelde et al. (1998) and Mjelde et al. (2003) cross the composite line used in this project (Figures 3.2-3.3). Their results are plotted in GM-SYS model as artificial wells. Additionally, the OBS MOHO is cross-checked with a surface from Grad et al. (2009), who compiled large quantities of various datasets to produce a high resolution MOHO depth map (Figure 3.4).

Densities are conditioned with well log density analysis and published work of other authors (Zastrozhnov et al., 2018; Ebbing et al., 2006; Maystrenko and Gernigon, 2018). Moreover, deeper densities are adjusted to match the anomaly. Similarly, initial magnetic susceptibilities are based on modelling done previously by Zastrozhnov et al. (2018), Ebbing et al. (2006), Maystrenko et al. (2018a). However, choice of crustal magnetic susceptibility depend on accepted theory explaining crustal composition. Consequently, modelling parameters are correlated with onshore measurements from the petrophysical database of the Norges Geologiske Undersøkelse (NGU) to support the favoured concept. Sedimentary rocks, on the contrary, are expected to have minimal contribution to magnetic signal and their susceptibility was chosen to be 0. Further, the parameters were calibrated relative to the magnetic response.

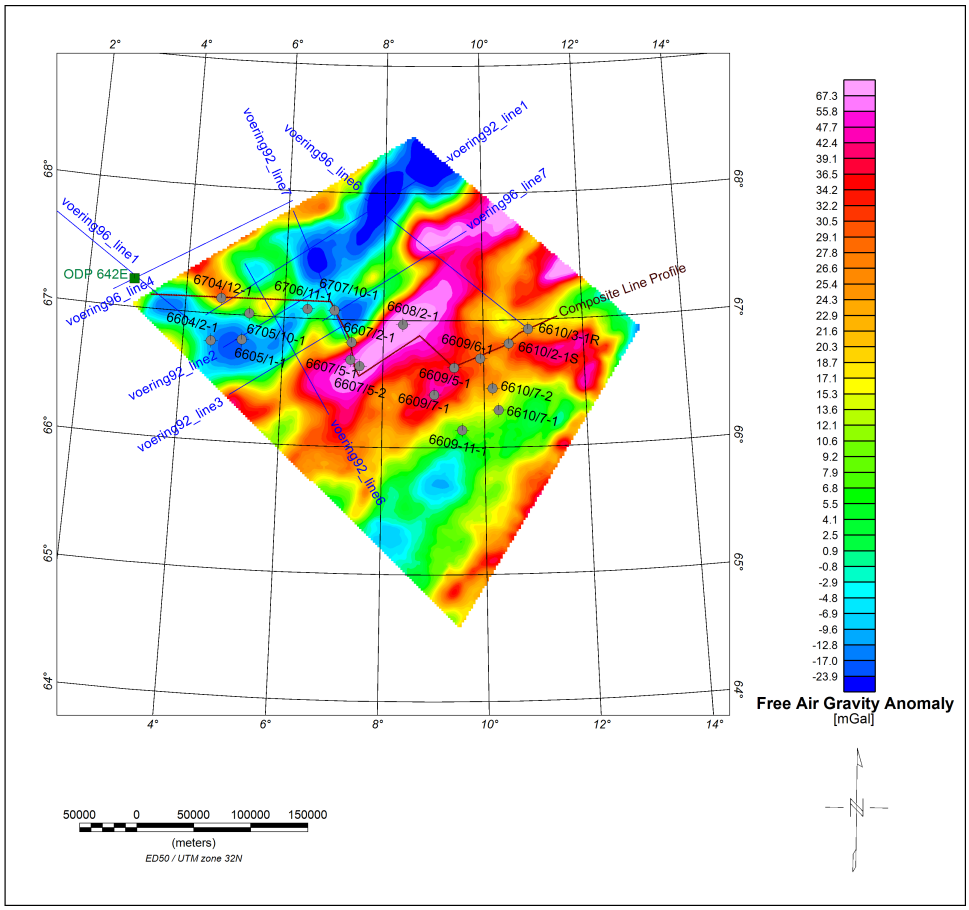

Figure 3.2: Free Air gravity anomaly modified after Olesen et al. (2010b). Locations of the composite line, wells and OBS profiles from Mjelde et al. (1997), Mjelde et al. (1998) and Mjelde et al. (2003) are included.

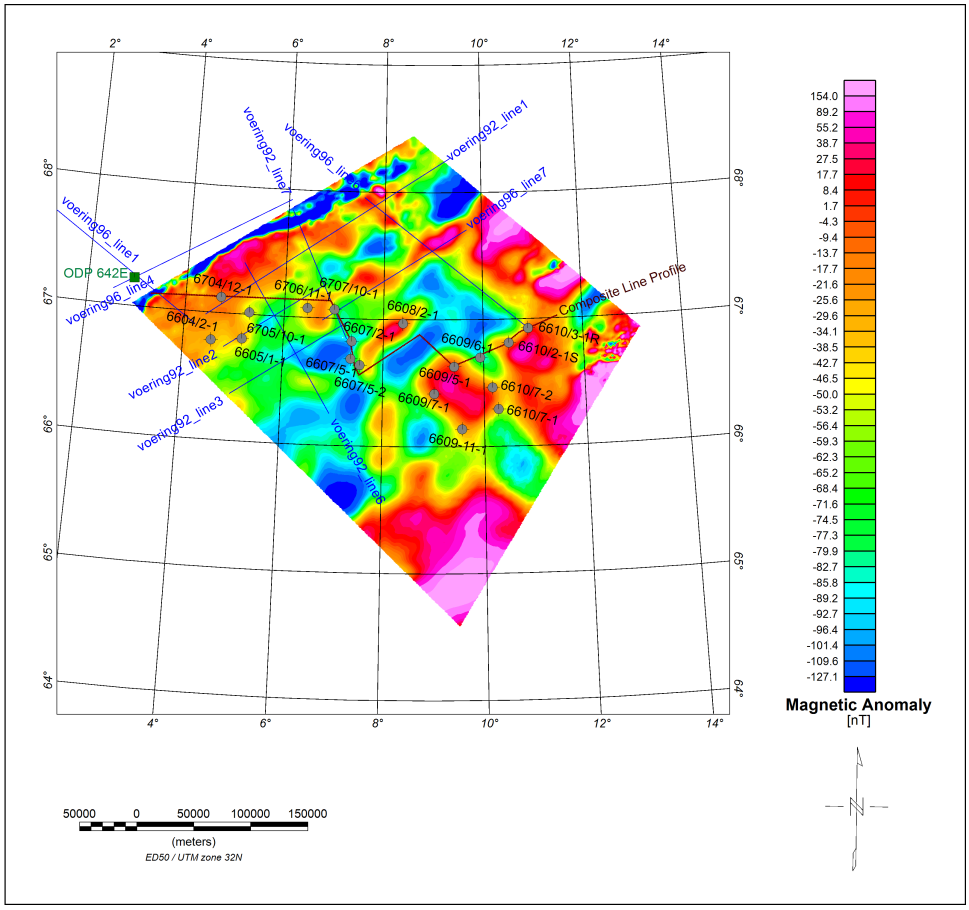

Figure 3.3: Magnetic anomaly modified after Olesen et al. (2010c). Locations of the composite line, wells and OBS profiles from Mjelde et al. (1997), Mjelde et al. (1998) and Mjelde et al. (2003) are included.

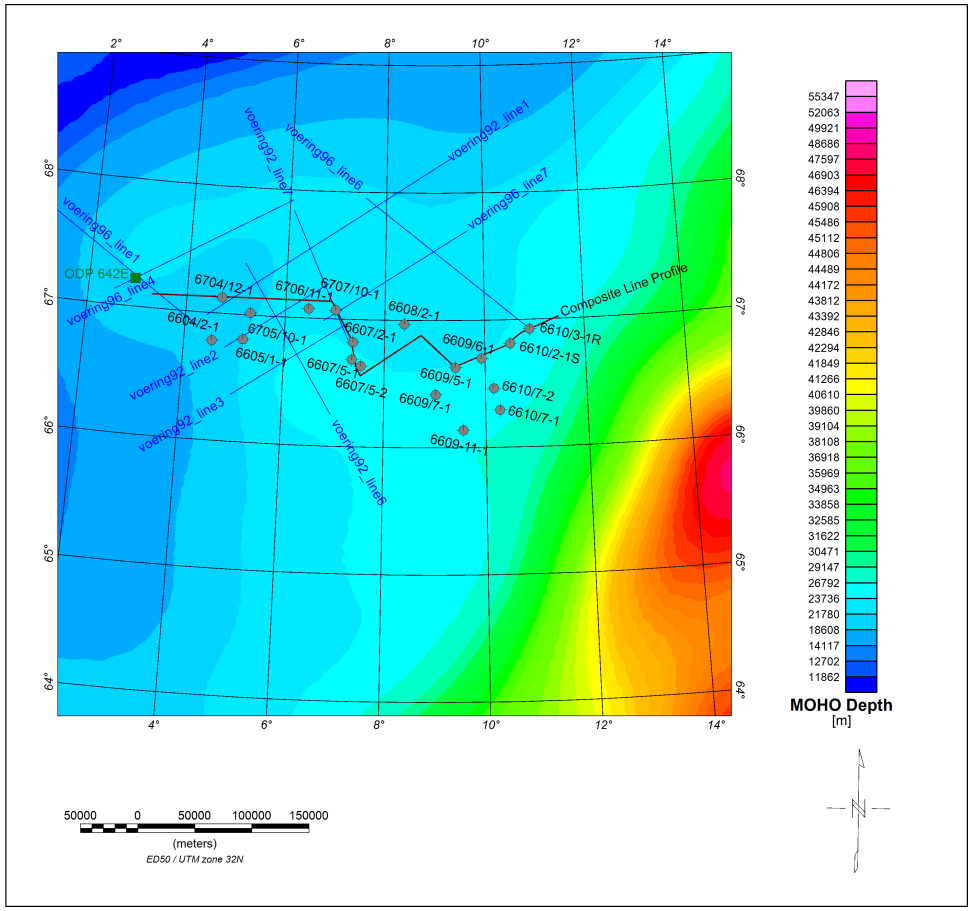

Figure 3.4: MOHO depth map modifed after Grad et al. (2009). Locations of the composite line, wells and OBS profiles from Mjelde et al. (1997), Mjelde et al. (1998) and Mjelde et al. (2003) are included.

3.3 Velocity and Density Study

Average velocities and velocity trends are important inputs when working with time to depth conversion. Check-shot velocities are closest to reflection seismic velocities, that is why they are used as a base for average velocity calculations. Interval velocity check-shot data is smoothed in Matlab by a moving median filter with a window size of 10 (example shown on Figure 3.5). Mean values are calculated and trends are analysed on the basis of first order polynomial fit. As check-shot depths are sparse, thin formations are not logged in some cases. Consequently, several units are merged together for simplicity.

Well log density analysis is done for all wells included in the project (Table 3.2). Densities of each formation are analyzed in a context of depth and lithology. Well log resolution is very high ($<$1 m), and while extreme peaks do not reflect regional trends, they can affect average values. For this reason, density logs are smoothed by a moving median filter with a window size of 100, as this gives the desired log appearance (Figure 3.5). Following that, depth trend of each formation is visualized by first grade polynomial fit and mean values are calculated.

3.4 Curie Depth Estimation

Radial average spectrum analysis is done in Geosoft with MAGMAP filtering extension. Essentially, it calculates 2D fast Fourier transform (FFT) followed by Radial Average Spectrum. Prior to applying FFT, it is crucial to window a grid according to chosen window size and perform the pre-processing. Pre-processing includes trend removal, expanding the grid to produce a perfect square shape and interpolating grid values across dummy points.[1]

Geosoft offers an opportunity to plot logarithm of the spectrum against spacial frequency. Assuming the relationship is defined by Equation 2.12, slope of the spectrum can be approximated by:

$$\frac{\partial Ln(\Phi_{av}(k))}{\partial k} \cong -2z_t, \tag{3.1}$$

or in case of spacial frequency ($f = k/2\pi$ [cycles/m]):

$$\frac{\partial Ln(\Phi_{av}(f))}{\partial f} \cong -4\pi z_t. \tag{3.2}$$

In that case, referring to Spector and Grant (1970) it is possible to estimate Curie depth by measuring the slope at lowermost wavenumbers. Moreover, Geosoft provides automatic depth calculation, which can be compared with manual technique results.

It is important to note that this method is extremely sensitive to grid size, as depth of penetration is limited by window length. In case of FFT spectral analysis, window length has to be at least 6 times the depth to deepest magnetic source (DDMS) (Personal communication, Saad, A. H., 2019). As an example, if Curie temperature is expected to be at 20 km depth, window size of minimum 120 km should be used. Taking this into

[1] For Curie depth estimation larger magnetic grid is extracted from Olesen et al. (2010c) (see Appendix C).

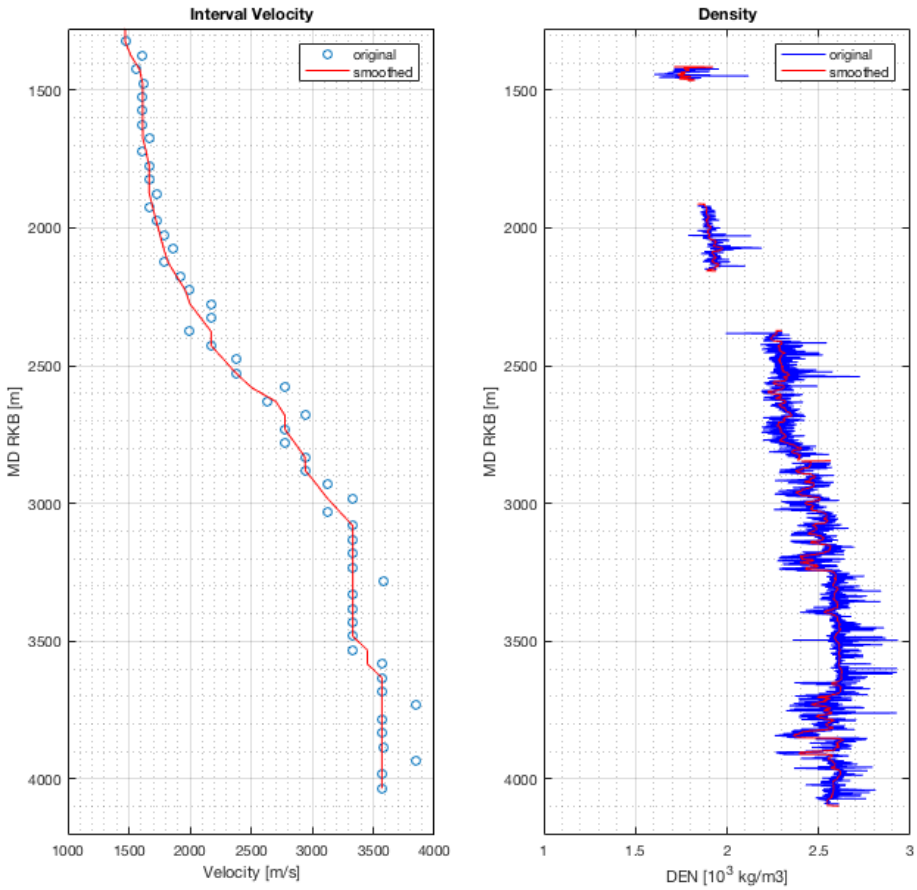

Figure 3.5: Velocity and density log smoothing example, well 6704/12-1. Moving median filters with sizes of 10 and 100 are used for velocity and density logs accordingly.

consideration, several window sizes are tested to see if depth estimates are consistent. The results are presented in Chapter 4.

3.5 Thermal Modelling

Thermal modelling is done according to equations described in Chapter 2. As mentioned previously, it is based on the work done during the Specialization Project (Chernyshova, 2018), where temperature, temperature gradient and heat flow profiles from the seabed to the wells' total depths (TDs) are calculated in Matlab software (Table 3.2). There, k is computed on the basis of its empirical correlation with V_p from sonic log (Duffaut et al., 2018), while A is estimated from GR log according to Bücker and Rybach (1996). Moreover, as modelling is constrained by surface temperature and heatflow, results are calibrated in order to fit the temperatures measured in the boreholes.

In this work, in order to confirm the trend observed in Chernyshova (2018), two additional wells are modelled using the same methodology: well 6607/5-1 located at the Utgard High and well 6609/6-1 positioned at the Grønøy High. Results are shown in Appendix A. Furthermore, thermal modelling is extended to 80 km depth, with k and A set according to expected lithologies and published data.

Chapter 4

Results: Gravity and Magnetic Model

4.1 Seismic Constraints

The results of Petrel seismic interpretation done in Chernyshova (2018) and reevaluated later are shown on Figure 4.2. Reflectors representing tops of the Naust Fm, Kai Fm, Brygge Fm, Paleocene sequence and Springar Fm are relatively simple to outline, as those are well constrained by the wells and are located at shallow times, where seismic has much higher signal to noise ratio. Well synthetic seismic created from convolving a wavelet with reflectivity series is used as a foundation for seismic interpretation (Table 4.1). The Naust Fm is the uppermost formation penetrated by all wells across the composite line. Naturally, both velocity and density of rocks are higher than that of water. Consequently, it is picked as first high amplitude positive reflection (hard kick). Based on the well logs the Kai Fm and Brygge Fm tops are represented by negative reflections (soft kick). Following the welltops and the fact that the Kai Fm is a base of prograding Naust Fm sedimentary wedges, it is traced across the Vøring Basin from the Vøring Marginal High to the Grønøy High where it is pinching out against the Brygge Fm. However, the Kai Fm is absent on the Vema Dome and the eastern Utgard High. The Brygge Fm, on the contrary, is more challenging to outline. It is distorted by polygonal faulting west of the Vema Dome, and affected by a large scale slump east of the Utgard High. Nevertheless, good well coverage allows to interpret the reflector across the whole Vøring Basin. As the Tare Fm seems to be absent on the northern Gjallar Ridge, top Paleocene is represented by the Tang Fm there, while remaining part of the Vøring Basin has the Tare Fm deposited on top of the Tang Fm, with the exception of the Utgard High where the Tang Fm is eroded. Well logs show both positive and negative reflections as evident in Table 4.1, and top Paleocene is interpreted as a surface where overlying Brygge Fm sediments downlap. Likewise, the Springar Fm is expected to exhibit both hard and soft reflection and is traced continuously as a major unconformity across the basin. Using this principle, at the location of well 6707/10-1 the

Springar Fm is interpreted above the indicated welltop.

Deeper interfaces are less prominent due to poor imaging as a result of insufficient acquisition or inadequate processing. Moreover, at the western part of the section the reflectors are obscured by magmatic intrusions, since high velocity igneous rock cause diffraction of seismic waves. Top of the Nise Fm is interpreted as hard reflector although it is showing weak soft kick in well 6610/3-1R (Table 4.1). The reflector is faulted at the Gjallar Ridge and masked by sills in the Någrind Synlcine and at the Vema Dome, which can be seen as very high amplitude positive reflections there (Figure 4.2). Across the Utgard High seismic lines are oriented parallel with internal bedding strike which makes it hard to resolve the Nise Fm top. Even though all these factors make the interpretation less curtain, on the regional level the geometry is expected to be accurate as it is well constrained by well data. Jurassic and Triassic sediments at the Nordland Ridge, the Grønøy High and the Vestfjørden Basin are outlined as distinct soft and hard reflections due to higher total organic content (TOC) in the first and high compaction low porosity sediments in the second. On the contrary, the Base Cretaceous Unconformity (BCU) at the western part of the composite line and the top basement surface are not penetrated by the wells. Therefore, additional seismic lines are used which connect the composite line with places of higher interpretation confidence. For example, well 6609/7-1 does reach top of the basement, and its representative reflection can be traced to the Utgard High through line 106A of GMNR-94 survey. Additionally, work done by Zastrozhnov et al. (2018) and Dalland et al. (1988) can serve as orientation when analysing the deepest units. Taking this into account, the BCU is interpreted as high amplitude reflector associated with regional unconformity, while top of the crystalline basement is interpreted on the basis of high positive amplitudes and change in seismic facies to chaotic and uniform. However, as deepest sediments reach high density and velocity values due to compaction, absence of substantial acoustic impedance contrast between sediments and basement can lead to lack of top basement seismic signature. In conclusion, current interpretation of the deepest reflectors constitutes preliminary result which is adjusted on the basis of regional OBS wide-angle profiles during the modelling stage. This data allows for better mapping of the units beneath the high reflectivity igneous rocks and has higher signal to noise ratio at the deeper levels.

In spite of uncertainties, it becomes evident that Cretaceous units constitute the largest part of the sediment column in the Vøring Basin (Figure 4.2). In addition to that, sediments are thickest in the Træna Basin and in the Någrind Syncline, while basement highs are expected at the Nordland Ridge, the Utgard High and the Gjallar Ridge (Figures 4.1-4.2).

Well	Top Kai	Top Brygge	Top Paleocene	Top Springar Fm	Top Nise Fm	Top Jurassic	Top Triassic
6704/12-1			hard kick (Tang Fm)	soft kick	hard kick	not penetrated	not penetrated
6707/10-1	soft kick	soft kick	soft kick (Tare Fm)	soft kick	hard kick	not penetrated	not penetrated
6607/2-1			hard kick (Tare Fm)	hard kick	not penetrated	not penetrated	not penetrated
6607/5-2	soft kick	soft kick	hard kick (Tare Fm)	soft kick	hard kick	not penetrated	not penetrated
6609/5-1	soft kick		hard kick (Tare Fm)	hard kick	hard kick	absent	hard kick
6610/2-1S	absent		hard kick (Tare Fm)	soft kick	hard kick	soft kick	hard kick
6610/3-1	absent		hard kick (Tare Fm)	hard kick	soft kick	soft kick (high TOC)	hard kick

Table 4.1: Well synthetic seismic response for main interfaces. Reflectively series are computed from acoustic impedance profile, which is based on sonic and density logs.

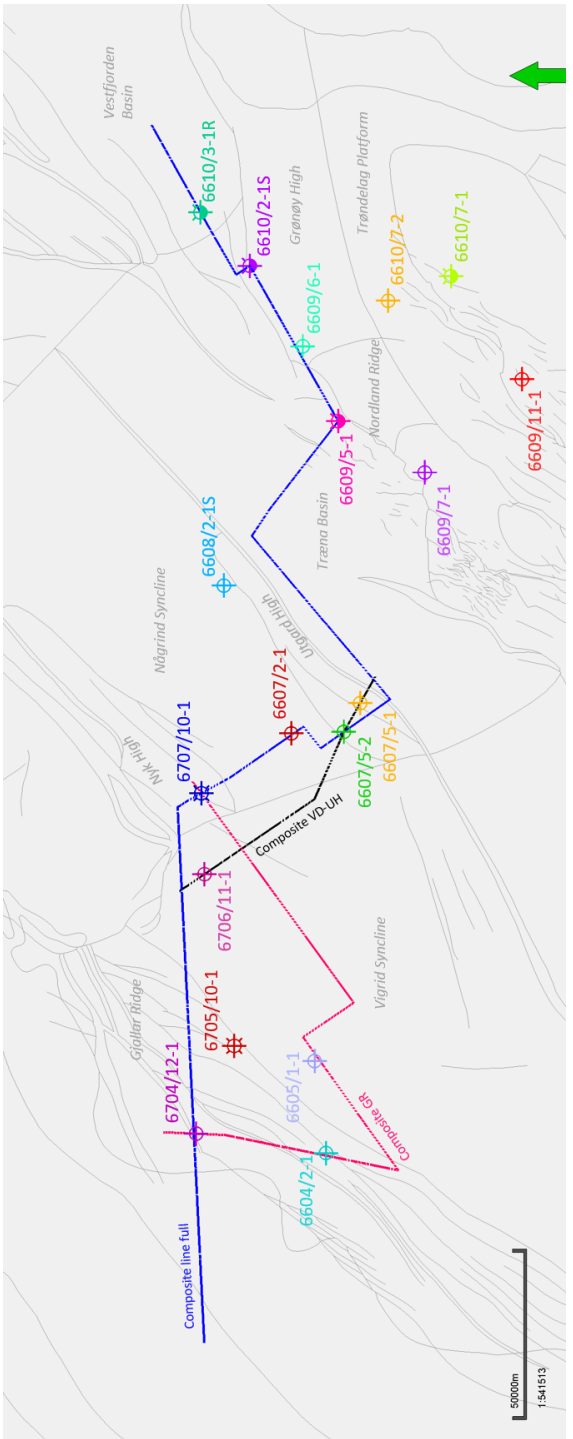

Figure 4.1: 2D Map of the composite lines and wells. Arrow points to North. *Composite line full* refers to Figure 4.2,4.5,4.7, *Composite VD-UH* is related to Figure 4.4, while *Composite GR* shows the profile from Figure 4.6.

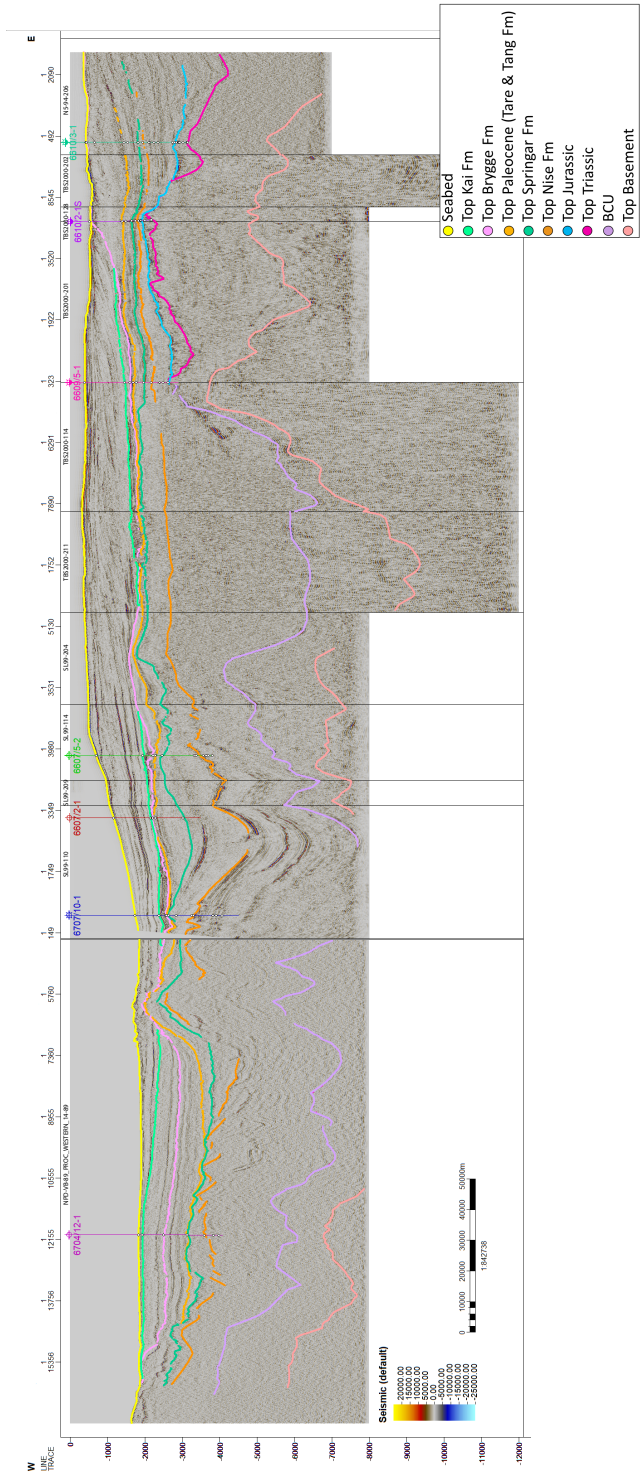

Figure 4.2: Seismic interpretation along the composite line. Location is shown on Figure 4.1 as *Composite line full*.

4.2 Density Trends

The main deposits in the Vøring Basin are deep marine shales (Figure 2.5). However, there are several sandstone units within Paleocene and Cretaceous sediments in addition to volcanic tuffs of the Tare Formation. None of the wells west of the Nordland Ridge have penetrated sequences older than Late Cretaceous, therefore it is unknown which sediments are located at the deepest parts of the western basin. At the same time, wells placed along the Grønøy High and on the Trøndelag platform have reached Jurassic and Triassic units (Figure 4.1). In this way, the presence of Jurassic and older rocks is expected across the basin, although as a result of active rifting through the Mesozoic era their thickness in the western part is questionable.

Nonetheless, as the Vøring Basin is represented by very thick Cretaceous shale packages, large density variations are not expected, except for depth trend related to chemical and mechanical compaction. The following section describes density log analysis for each individual formation and shows the reasoning behind chosen modelling densities.

Quaternary - Eocene Interval

Naust Fm

Figure 4.3a presents the results of density study for the Naust Fm. X-axis shows depth below the seabed and Y-axis indicates density estimates. Points represent mean values across the formation and are plotted at the mid-depth, while dashed line displays minimum and maximum densities across the interval. Solid line, at the same time, exhibits linear trend which is calculated on the basis of first order polynomial approximation.

Based on this result, the Naust Fm appears to have average densities of about 1.7 g/cm^3 west of the Vema Dome and 2.2 g/cm^3 to the east, with the exception of well 6609/6-1 which detects slightly higher values. Ottesen et al. (2009) point out that the Naust Fm contains several sub-units which are named N, A, U, S, T. Oldest N and A are represented by wedges prograding towards north-east and consisting of fluviomarine sediments and ice-rafted debris, U is composed of aggradational and slope building sequences of both glacial and marine origin, while S and T are related to 3 last glaciations with substantial amounts of glacially derived sediments (Ottesen et al., 2009). Possibly, conflicting densities are related to individual units logged by different wells. As lithology and chronostratigraphy information from cuttings is not available for shallowest intervals, it is possible to use seismic analysis to conclude whether these Naust Fm sub-units could have different densities.

The higher density Naust Fm at the Utgard High can be connected with the low density Naust Fm in well 6706/11-1 through a composite seismic profile composed of SL99-199 and GMNR-94-106 (Figure 4.1). Based on this seismic section the formation is subdivided into several informal units on the basis of the following reflectors:

- **intra Naust 1** - soft kick
- **intra Naust 2** - hard kick
- **intra Naust 3** - hard kick

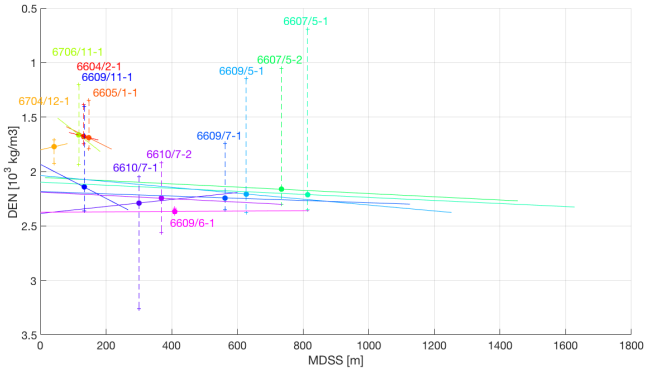

(a) Naust Fm

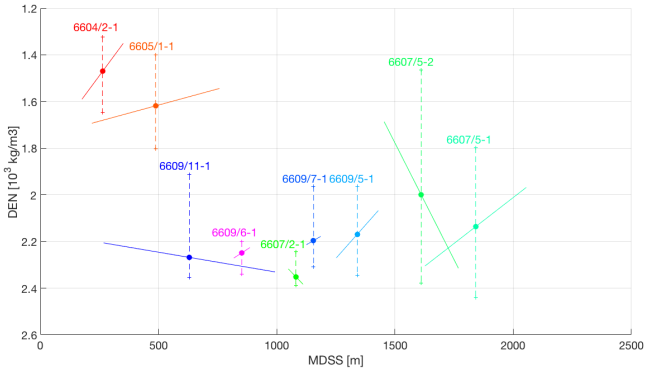

(b) Kai Fm

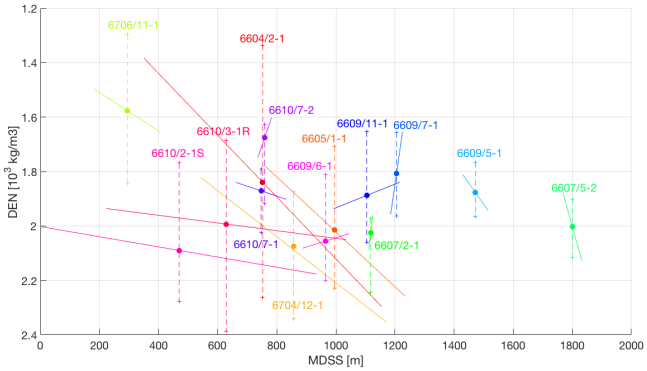

(c) Brygge Fm

Figure 4.3: Density trends for the Naust, Kai and Brygge formations. Points represent mean values, dashed lines display minimum and maximum densities across the interval, while solid lines show approximated linear trends.

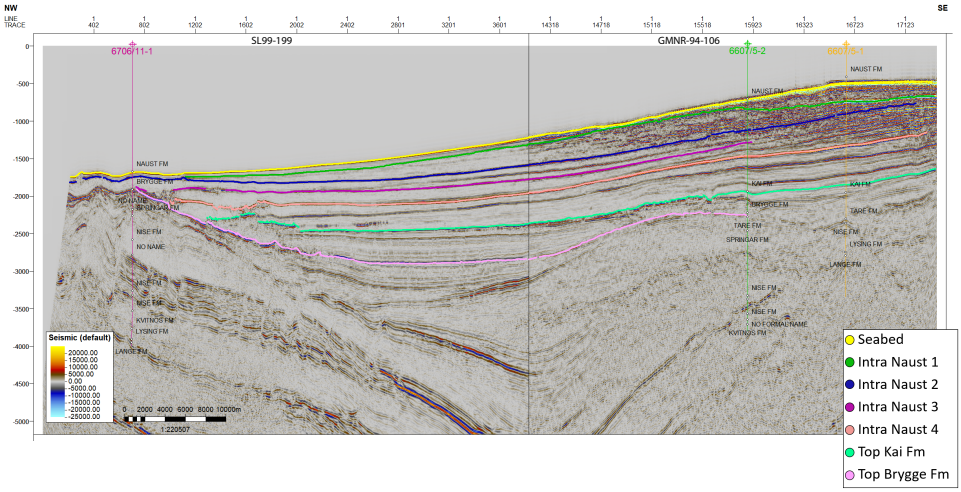

Figure 4.4: Naust Fm subdivision, from south of the Vema Dome to the Utgard High. Location is shown on Figure 4.1 as *Composite VD-UH*.

- **intra Naust 4** - hard kick

Although this subdivision is an attempt to replicate units identified by Ottesen et al. (2009), the main principles behind this subdivision are varying internal bedding angles, onlap of younger strata and high amplitudes indicating contrasts in properties. The result is shown on Figure 4.4. It becomes evident that only the uppermost part of the Naust Fm is logged by well 6706/11-1 when compared to wells 6607/5-2 and 6607/5-1. This sequence is likely to be equivalent to S, T and upper U units from Ottesen et al. (2009). Extending the interpretation to the full composite line indicates S and T segments in well 6704/12-1 (Figure 4.5).

This makes it possible to assume that only the shallowest S, T and upper U sections of the Naust Fm are penetrated by wells located on the Gjallar Ridge, which detect lower average densities. Even though those rocks are present to the east, higher densities of the lower Naust Fm affect the mean values there. Therefore, it could be argued to split the Naust Fm along the **intra Naust 3** reflector. At the same time, velocities from OBS profiles show rather sharp increase in the proximity of well 6707/10-1. 1992 OBS Line 7 (Mjelde et al., 1997) expresses velocity increase from 1.6-1.7 km/s to 1.9-2.3 km/s across the Nyk High area, while 1996 OBS Line 7 (Mjelde et al., 1998) shows velocity of 2 km/s at 2 km distance from well 6707/10-1 (Figure 3.2). As velocity is often correlated with density, an alternative model could be the lateral density change within the formation. However, both models lead to minor differences in gravity response. Consequently, for simplicity the Naust Fm is subdivided along the **intra Naust 3** reflector into upper unit with density of 1.7 g/cm^3 and lower unit with density of 2.2 g/cm^3. The contrast could be attributed to lithological shift, for example from glacial till at the top to marine shales and ice rafted

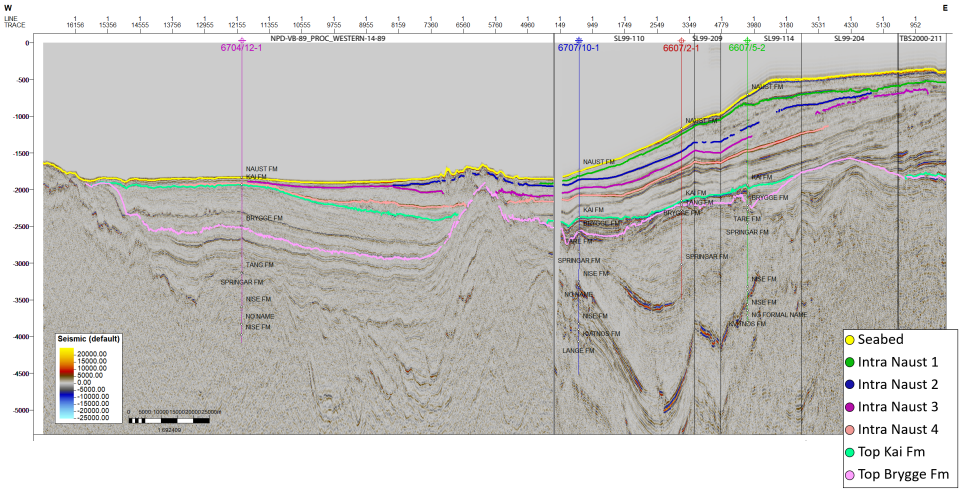

Figure 4.5: Naust Fm subdivision along the western part of the composite line. Location is shown on Figure 4.1 as *Composite line full*.

detritus at the bottom.

Kai Fm

The Kai Fm appears to express lithological variations as average values are inconsistent (Figure 4.3b).[1] Moreover, several wells show density decrease with depth, which is likely to be caused by lithological change. According to the Norwegian Petroleum Directorate's (NPD) completion information, for wells 6604/2-1 and 6704/12-1 the Kai Fm is almost entirely composed of biogenic ooze (Norwegian Petroleum Directorate, 2019a,b). This issue is addressed by Eidvin et al. (2014). The authors state that during Oligocene to Early Pliocene times the Vøring Basin was located in the distal position from the sediment source, which led to a significant deposition of ooze. As this lithology has much lower density compared to sand and shale, ooze presence could be a possible source of trends on Figure 4.3b.

Across the Gjallar Ridge a composite line incorporating GVF2000-301, GRS98-GRS99-11-303, GVF2000-118, GVF2000-214 and GVF2000-104 is used to outline and subdivide the ooze section through the Kai and Brygge formations on the basis of density and gamma ray logs and seismic responses (Figure 4.6). The following reflectors are identified:

- **inner ooze top low den** - soft kick
- **inner ooze base low den** - hard kick

[1] Kai Fm top pick is missing for well 6707/10-1. Consequently, quality check based on seismic interpretation was performed and top Kai Fm was added at 1940 measured depth below rotary table (MD RKB). On the same basis, Kai Fm top was shifted from 1380 MD RKB to 1932 MD RKB for well 6607/2-1.

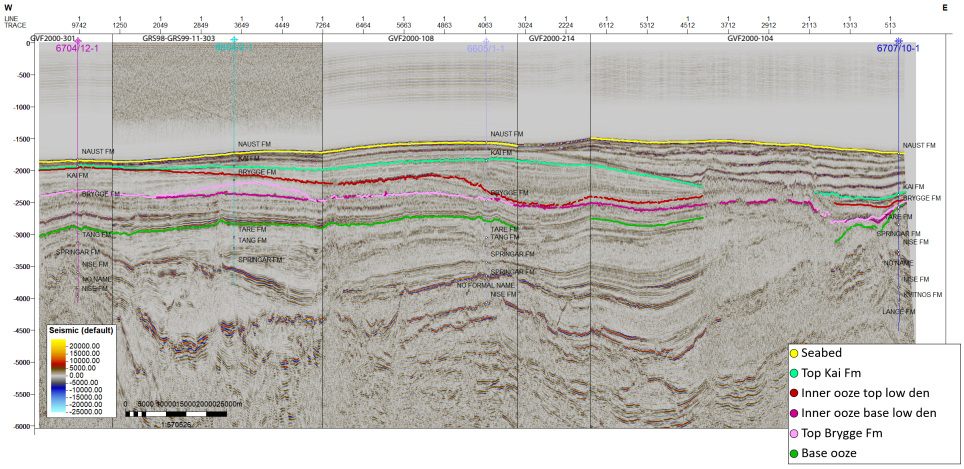

Figure 4.6: Ooze subdivision across the Gjallar Ridge. Location is shown on Figure 4.1 as *Composite GR*.

- **base ooze** - hard kick

The **Inner ooze top low den** and **inner ooze base low den** are upper and lower boundaries of very low density unit within the ooze section, while higher density ooze is expected above and below down to the **base ooze** limit.

This interpretation helps to identify corresponding reflectors along the main composite line (Figure 4.7). Note that top Kai Fm west of the Vema Doma coincides with the **inner ooze top low den**. The resulting Kai Fm ooze sections are upper unit with density of 1.6 g/cm^3 (between top Kai Fm and the **inner ooze top low den**) and middle unit with density of 1.4 g/cm^3 (between the **inner ooze top low den** and **inner ooze base low den**). Remaining parts of the Kai Fm express densities of 2.2 g/cm^3 with shale being the dominant lithology. In this way, for simplicity the Kai Fm is modelled with density of 1.6 g/cm^3 west of the Vema Dome, and 2.2 g/cm^3 to the east.

Brygge Fm

West of the Vema Dome ooze is also present within the Brygge Fm, which explains scattered average densities (Figure 4.3c). Similar to the Kai Fm, Brygge Fm is subdivided into two units: lower ooze with a density of 1.9 g/cm^3 (from top Brygge Fm to the **base ooze**) and the remaining shaly part with a density of 2.0 g/cm^3 (Figures 4.6-4.7).[2] As seen on Figures 4.6-4.7 indicated Brygge Fm welltops are concordant with the **inner ooze base low den** reflector for wells 6605/1-1 and 6707/10-1. However, the pick is below this reflector for well 6704/12-1 and above - for well 6604/2-1. Therefore, it is important

[2]Missing top Brygge Fm in well 6707/10-1 is added at 2120 MD RKB. In addition, Undefined Gp at 1994 MD RKB is changed to top Brygge Fm for well 6607/2-1.

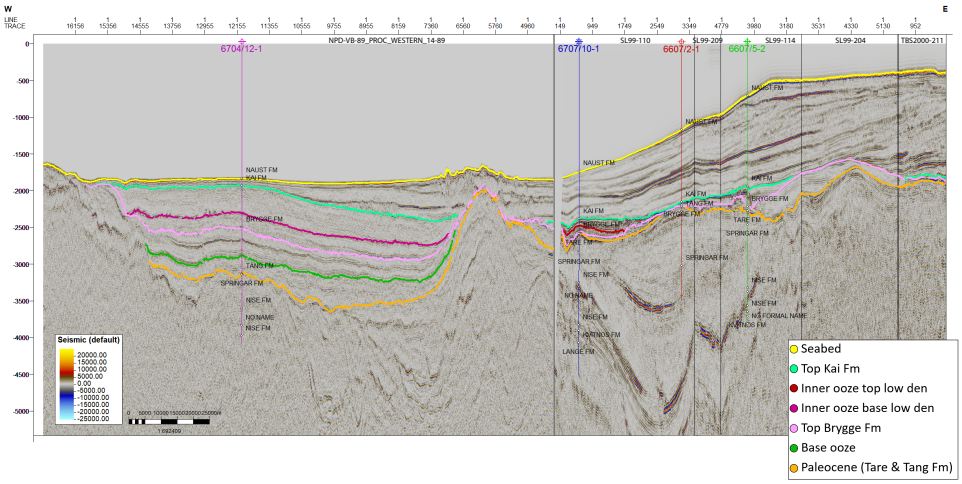

Figure 4.7: Ooze subdivision along the western part of the composite line. Location is shown on Figure 4.1 as *Composite line full*.

to consider a possibility of the **inner ooze base low den** being the upper boundary of the Brygge Fm despite of inconsistencies with the well data. Nevertheless, in order to simplify density modelling, a mean value of 2.0 g/cm^3 is taken across the formation.

Paleocene Interval

For most of the wells the Tare and Tang formations have average densities between 2.1 and 2.3 g/cm^3, with the exception of wells located in the proximity of the Trøndelag Platform (Figures 4.8a-4.8b). Lower values do not seem to have explicit lithological cause, as many wells penetrate shales with interbeds of sands and silts. Neither can they be related to depth as evident from Figures 4.8a-4.8b. Hence, when disregarding the anomalies average density becomes 2.2 g/cm^3.

Cretaceous Interval

Modelling each Cretaceous formation separately will have profound effect on model's complexity, which in its turn will increase number of variables and ambiguity. Therefore, as a starting point formations are evaluated individually and merged into larger units on the basis of density values.

Springar Fm densities express high variation between the wells (Figure 4.9a), which can be caused by presence of thin sands and intensified by a strong depth trend. Nevertheless, most of the wells located along the composite line show average densities close to 2.4 g/cm^3.

Similarly, values for the Nise Fm are scattered across the plot (Figure 4.9b). It is important to note that in the Vøring Basin a substantial part of the shaly Nise Fm contains

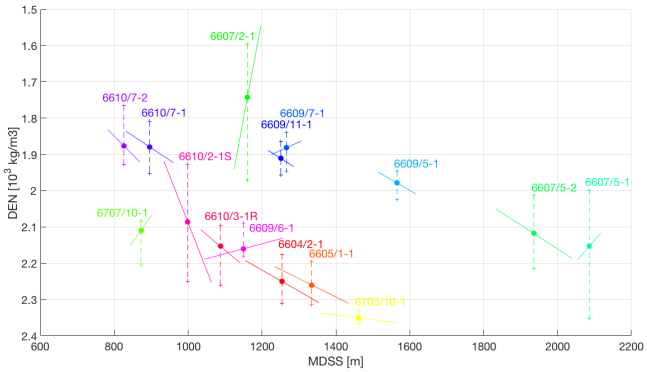

(a) Tare Fm

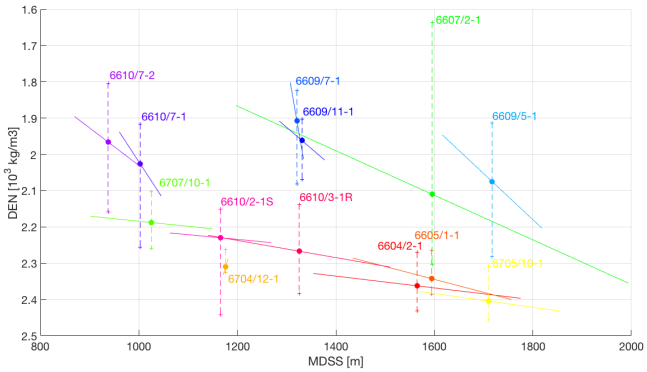

(b) Tang Fm

Figure 4.8: Density trends for the Tare and Tang formations. Points represent mean values, dashed lines display minimum and maximum densities across the interval, while solid lines show approximated linear trends.

rather thick sand bodies of the informal Delfin Fm, which have slightly lower densities. Moreover, complexity is escalated by the strong depth trend. Nonetheless, the effect of sands is minor and the majority of wells indicates an average of 2.5 g/cm^3.

Mean density of the Kvitnos Fm is also expected to be around 2.5 g/cm^3 (Figure 4.9c). At the same time, number is higher for well 6607/5-2 owing to presence of a dolerite sill, which exhibits values above 3 g/cm^3. However, due to insignificant thickness, sills' contribution to gravity response is considered to be minor.

In the western part of the section sandstones of the Lysing Fm are penetrated by well 6607/5-1, which is located at the Utgard High. However, existence of the Lysing Fm there is questionable, as this contradicts the information given in completion report (Fittall et al., 1988). Neglecting the estimate from this well, and taking into account the fact that the Lysing Fm is represented by sandstones across the section leads to an average density of 2.5-2.55 g/cm^3 (Figure 4.10a). However, lower readings in well 6610/2-1S could indicate that the Cretaceous sediments at the northern Grønøy High were never buried to the levels reached by the Cretaceous sequence in the synclines and within the subbasins.

An average density estimate for the Lange Fm is 2.5 g/cm^3 (Figure 4.10b), however several wells show values as high as 2.6 g/cm^3. In addition to that, the shallowest Lange Fm in the vicinity of the Trøndelag Platform reaches densities as low as 2 g/cm^3.

The Lyr Fm, at the same time, is only logged by two wells in the project: 6609/11-1 and 6610/3-1R. While the first well shows an average density of 2.4 g/cm^3 and is located on the high, the second one has a density of 2.6 g/cm^3 and is positioned at a greater depth (Figure 4.10c). As composite section does not cover areas across the Trøndelag Platform, it is adequate to trust density reading from well 6610/3-1R.

In this way, the whole Cretaceous unit is expected to have densities between 2.4 to 2.6 g/cm^3 from the Base Tertiary Unconformity and down to the Base Cretaceous Unconformity: 2.4 g/cm^3 within the Springar Fm, 2.5 g/cm^3 within the Nise Fm - Lysing Fm interval, and 2.6 g/cm^3 below. However, as deepest parts of the synclines are not logged by the wells, it is possible that deep Cretaceous sediments can reach even higher density values.

Jurassic Interval

As mentioned previously, Jurassic rocks are likely to be present across the Vøring Basin. However, due to extensive continental rifting their thickness at the western part within the sag subbasins is expected to be insignificant. Having said that, Jurassic interval has only been proven at the eastern part of the Vøring Basin within the Vestfjørden Basin and on the Trøndelag Platform. Consequently, this analysis is focused on the eastern part of the profile.

Starting with very high TOC shales of the Spekk Fm, densities are expected to be low compared to adjacent units (Dalland et al., 1988). Along the composite line the formation is penetrated by well 6610/3-1, while on the Trøndelag Platform wells 6609/11-1 and 6610/7-1 log the interval. Average values from the two areas are different and are likely to be depth dependent (Figure 4.11a). In this way, density of 2.4 g/cm^3 is expected north of the Nordland Ridge.

The shaly Melke Fm is detected by the same wells and also exhibits the depth trend (Figure 4.11b). It is unclear what causes very low densities in well 6610/7-1 as lithology is

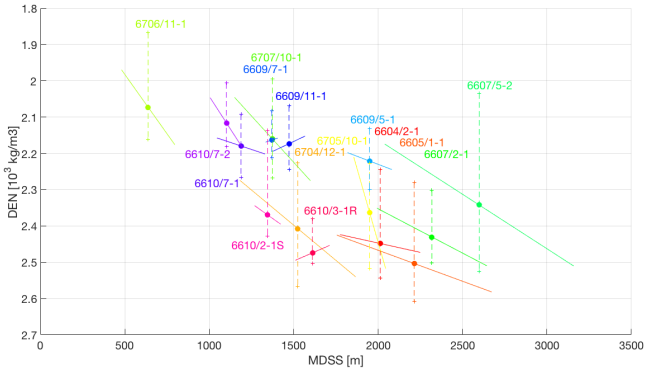

(a) Springar Fm

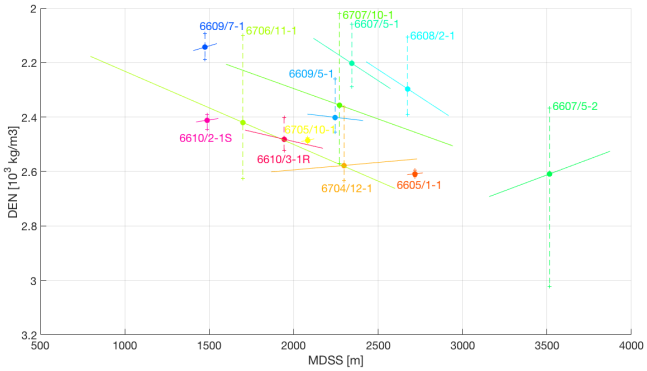

(b) Nise Fm

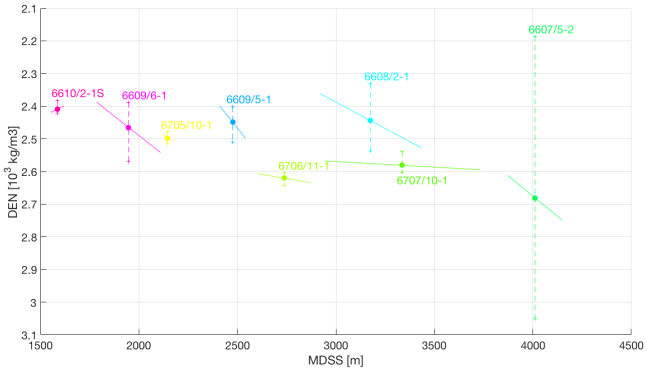

(c) Kvitnos Fm

Figure 4.9: Density trends for the Springar, Nise and Kvitnos formations. Points represent mean values, dashed lines display minimum and maximum densities across the interval, while solid lines show approximated linear trends.

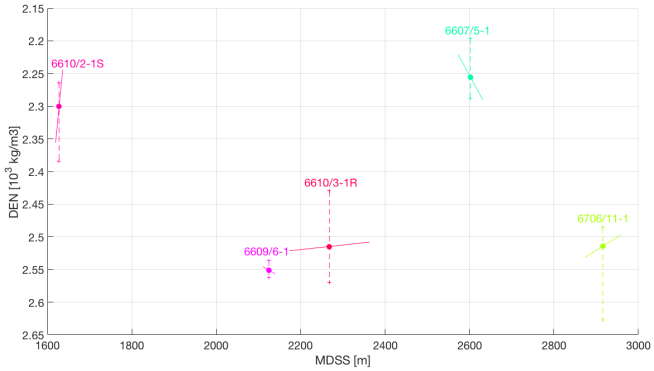

(a) Lysing Fm

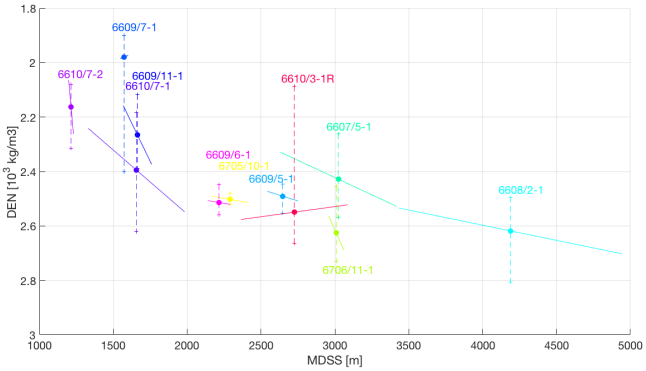

(b) Lange Fm

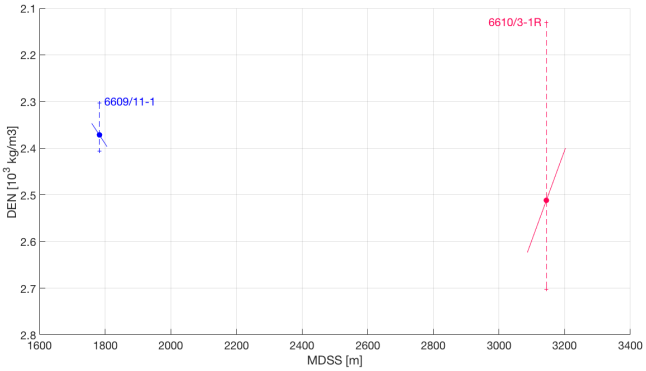

(c) Lyr Fm

Figure 4.10: Density trends for the Lysing, Lange and Lyr formations. Points represent mean values, dashed lines display minimum and maximum densities across the interval, while solid lines show approximated linear trends.

relatively uniform (claystone with limestone stringers according to Hellestrand and Larsen (n.d.)). However, along the composite line the Melke Fm is thin and is only drilled by well 6610/3-1. Therefore density of 2.5-2.6 g/cm^3 is expected.

Claystones of the Not Fm and sandstones of the Ile Fm are penetrated by two wells in the project: 6610/7-1 and 6610/3-1R (Figures 4.11c, 4.12a). While averages of two formations vary with approximately 0.1 g/cm^3 for well 6610/7-1, misfit for well 6610/3-1 is less than 0.05 g/cm^3 as differences between shale and sand densities tend to decrease with compaction degree. In this case, the Not and Ile formations in the southern Vestfjorden Basin are likely to have densities of 2.55 g/cm^3.

Similarly, the Tofte Fm sands which are only proven by well 6610/3-1 show density range from 2.45 g/cm^3 to 2.55 g/cm^3 with an average of 2.5 g/cm^3 (Figure 4.12b). Note the negative depth trend which is caused by sand grading into shaly silt (Fristad et al., 1994).

As for other Jurassic units, density of the Tilje Fm sandstone expresses strong depth dependency: from 2.15 g/cm^3 at 1250 m measured depth sub-sea (MDSS) to 2.55 g/cm^3 at 3500 m MDSS (Figure 4.12c). On this basis, it could be argued that Tilje Fm density is increasing with 0.15 g/cm^3 per 1 km.

Unsurprisingly, depth trend persists in the Åre Fm (Figure 4.13a). Scattering of density values is likely to be related to interchanging sand, shale and coal beds. Coal densities reach extremely low values of 1.5-1.7 g/cm^3 and are expected to affect the averages. Hence, mean density of the Åre Fm is believed to be around 2.35 g/cm^3 at the Nordland Ridge and 2.5 g/cm^3 in the Vestfjorden Basin.

In conclusion, Jurassic interval should be viewed in a context of depth and location. The low density organic rich Spekk and Åre formations are thin and are not expected to affect the modelling results noticeably. As a consequence, western Jurassic sequence is split in two parts: shallow Jurassic units along the Nordland Ridge with a density of 2.4-2.45 g/cm^3 and the deeper segment to the north with an average density of 2.55 g/cm^3.

Triassic Interval

Density readings for the Grey Beds show slightly dispersed distribution with evident depth trend (Figure 4.13b). Well 6610/7-2 has broad range of values from around 2 g/cm^3 to 2.8 g/cm^3, which can be attributed to presence of coal and salt units (Rasmussen and Larsen, n.d.). Nevertheless, the lithology is mainly represented by mixture of shale, silt and sand, and average density is assumed to vary from 2.4 g/cm^3 to 2.6 g/cm^3 depending on depth.

The Red Beds deposits are similar to the Grey Beds, and consequently, they express analogous trend with an increase from 2.4 g/cm^3 to 2.6 g/cm^3 (Figure 4.13c). Extremely low values in well 6610/2-1S is a bottom hole artifact.

In order to simplify the density model the Grey Beds and Red Beds are merged into one unit with a density of 2.55-2.65 g/cm^3. Moreover, as rifting has started during the late Permian time (Halland et al., 2013), thin Permian deposits are expected across the Vøring basin. However, their petrophysical characteristics are likely to be similar to deep Triassic rocks. Consequently, this unit is expected to include deeper undifferentiated sediments in addition to Triassic Grey Beds and Red Beds.

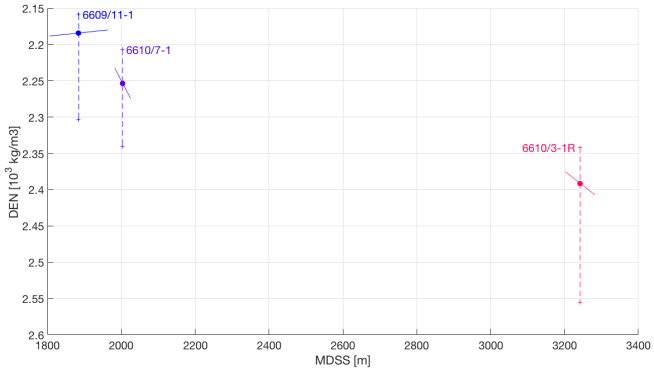

(a) Spekk Fm

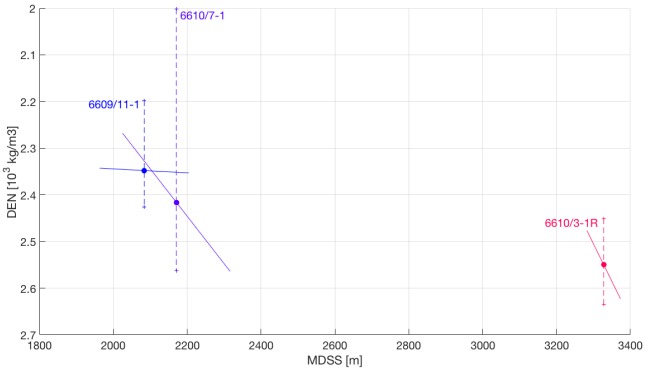

(b) Melke Fm

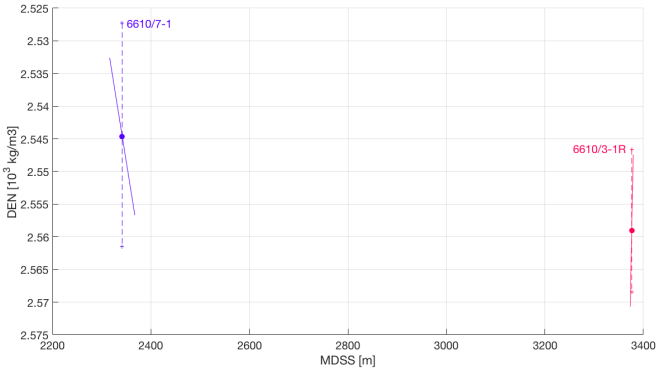

(c) Not Fm

Figure 4.11: Density trends for the Spekk, Melke and Not formations. Points represent mean values, dashed lines display minimum and maximum densities across the interval, while solid lines show approximated linear trends.

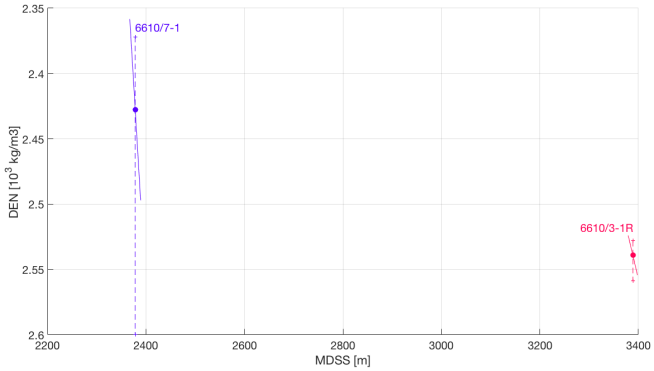

(a) Ile Fm

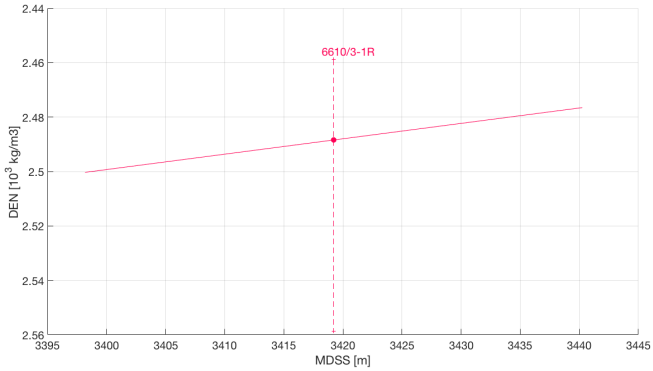

(b) Tofte Fm

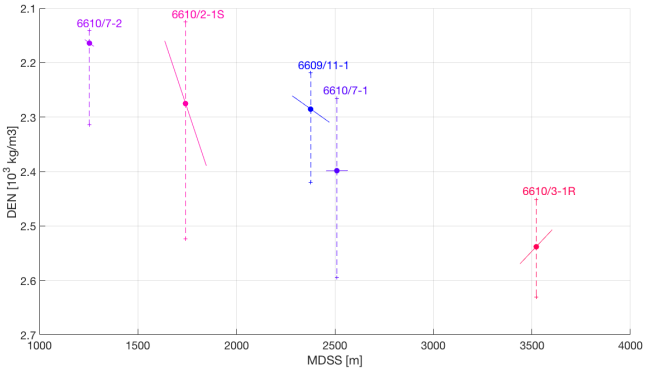

(c) Tilje Fm

Figure 4.12: Density trends for the Ile, Tofte and Tilje formations. Points represent mean values, dashed lines display minimum and maximum densities across the interval, while solid lines show approximated linear trends.

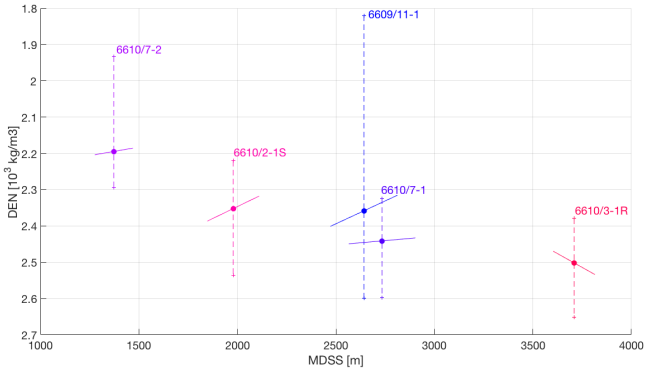

(a) Åre Fm

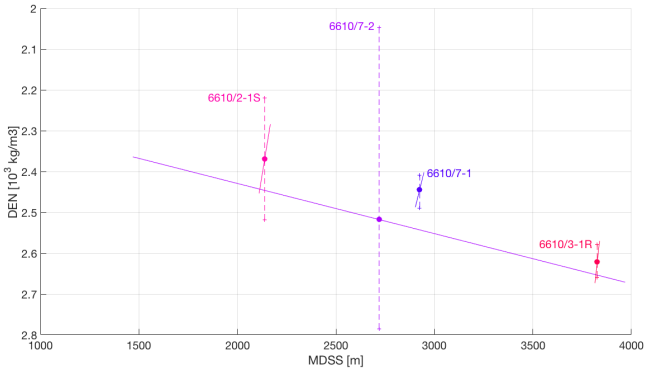

(b) Grey Beds

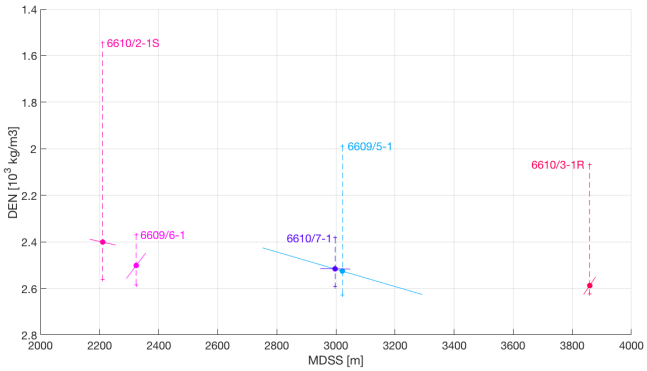

(c) Red Beds

Figure 4.13: Density trends for the Åre Fm, Grey Beds and Red Beds. Points represent mean values, dashed lines display minimum and maximum densities across the interval, while solid lines show approximated linear trends.

4.3 Velocity Trends

Interval velocities serve as a main input controlling time to depth conversion. In order to build velocity model in Geosoft GM-SYS, available check-shot interval velocities are studied. Figure 4.14 shows approximated linear velocity trends and average values for the main units.

It could be argued that check-shot velocities are not fully representative of regional velocities as wells are scattered across large areas and are likely to show local trends. That is why check-shot data is analyzed in conjunction with OBS data (Table 4.2). However, it should be taken into account that OBS velocities are slightly higher than reflection wave velocities as experience shows (Gernigon et al., 2004).

Both OBS and check-shot data indicate that the Naust and Kai formations west of the Vema Dome have low velocities ranging between 1400 and 1800 m/s. Across the Nyk High and further to the east the values are increasing to 2200 m/s with an extreme of 3000 m/s in well 6608/2-1. Converting the unit with 1700 m/s in the western part and 2200-2300 m/s in the eastern part results in good match with the welltops. The Brygge Fm velocities, at the same time, vary from minimum of 1700 m/s to exceptional 2600 m/s, while the most common estimate appears to be 2200 m/s. Similarly, Paleocene Tare and Tang Fm express both low (1800 m/s) and high (3200 m/s) numbers, with mean value of 2500 m/s. Using 2200 m/s and 2500 m/s for the Brygge Fm and Paleocene unit accordingly gives reasonable fit with the welltops. Finding appropriate velocities for conversion of Cretaceous segments is less straightforward due to several reasons. First of all, the depth trend is expected as Cretaceous sequence is very thick. In addition to that, in the western part of the section the oldest Cretaceous formation penetrated by wells is the Kvitnos Fm, and velocity analysis for units below is solely based on OBS profiles. Moreover, seismic interpretation did not resolve uncertainties related to the BCU, presence of older sediments below the deep Cretaceous subbasins and sediment-basement interface. Taking all this information into consideration, Cretaceous package is split into three different parts: the Springar Fm with velocity of 2800 m/s, Upper Cretaceous unit including the Nise, Kvitnos and Lysing Fm with velocity of 4000 m/s, and Older Cretaceous with an average velocity of 5000 m/s. Jurassic and Triassic components are converted with 4400-4500 m/s, while undifferentiated older sediments across the Nyk High and the Træna Basin are converted with 5500 m/s. The resulting depth model is modified and appended with crustal boundaries based on the OBS interfaces.

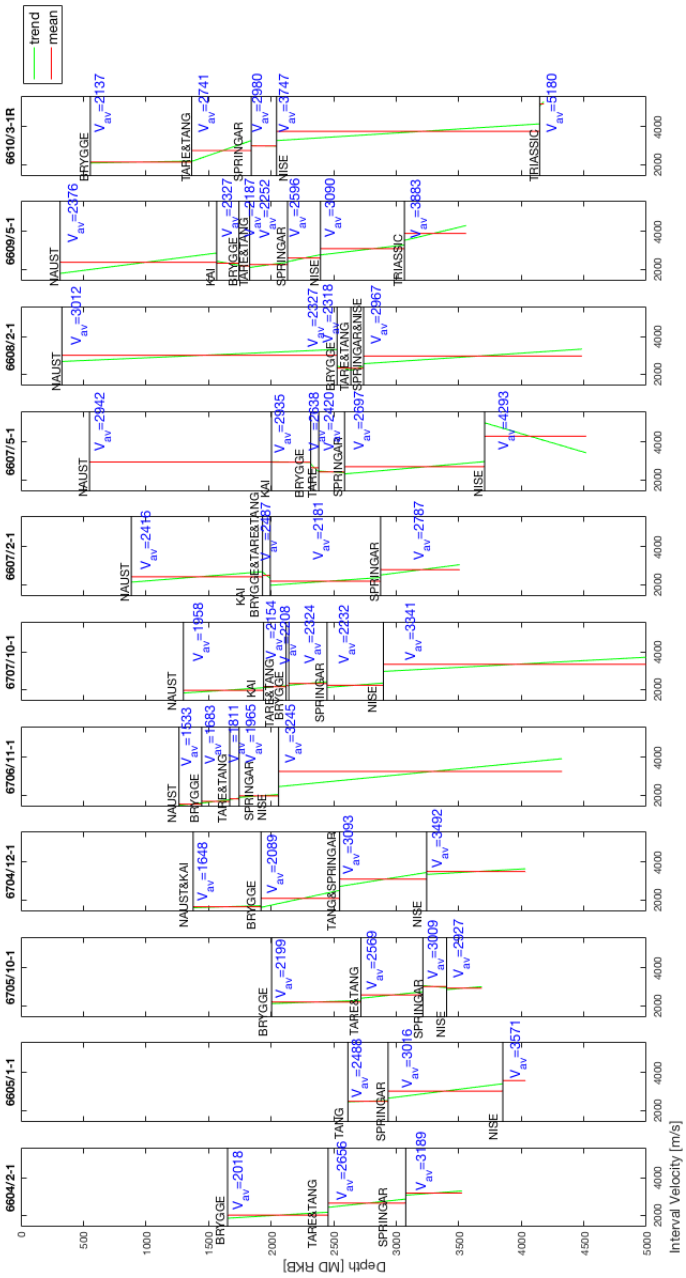

Figure 4.14: Velocity trends based on available check-shot data.

Fm	96-4	96-1	92-1	92-6	92-2	92-7	96-7	92-3	96-6
Naust			1.4			1.6-1.7	2.05-1.96		
Kai			1.6-1.7			1.7	1.71		
Brygge			2-3.2			1.8-2	1.71		2.1-2.15
Tare and Tang			3.2			2	2.11		2.52
Cretaceous above TCU		4.1	3.8-4.1			2.7-4.4	2.6-4.35		3.7-4.3
Cretaceous below TCU			4.8-5.3	5.3-5.5	5-5.6	5-5.6	4.6-4.85	5.1-5.6	4.4
Jurassic									4.4-4.55
Triassic									4.4-4.55
Basalt 1									
Basalt 2	5.9								
Upper and Middle Crust	6.2-6.85	5.95-6.25	6.2	6.2-6.6	6.2-6.6	6.2-6.6	5.9-6.5	6.2-6.6	6-6.5
HVLC	7.35-7.8	7.2	7.1-7.3	7.2-7.4	7.2-7.4	7.2-7.4	6.9-7.1	7.2-7.4	6.8-7.1
MOHO		7.85	8.2	8.2	8.2	8.2	7.8	8.2	8.2

Table 4.2: P-wave velocities for modelled units in [km/s] inferred from OBS profiles (after Mjelde et al. (1997), Mjelde et al. (1998), Mjelde et al. (2003)). Column legend indicates different OBS profiles as A-B, where A is two last digits in survey's year and B is a line number. TCU is used for the Top Cenomanian Unconformity.

4.4 Curie Depth

This section describes an attempt to calculate Curie depth from magnetic data grids by measuring the slope of radial average power spectrum as described in Chapter 3. As window size is a crucial parameter defining the method's penetration depth, several alternatives are tested. Figures 4.15-4.17 present the results for 170×170 km^2, 230×230 km^2 and 300×300 km^2 window sizes.[3]

According to Figure 4.15, when using a window size of 170×170 km^2 DDMS deepens from 11-12 km at the Gjallar Ridge to 17 km at the Utgard High and shallows again to 11-13 km at the Grønøy High. Increasing the window size to 230×230 km^2 results in deeper DDMS ranging from 12-14 km at the flanks of the Vøring Basin to 18 km at the center (Figure 4.16). Measuring the slope manually leads to even higher estimate of 27 km at the Utgard High - Træna Basin area outlined by a red window in the middle. Moreover, similar values are produced when using extreme window size of 300×300 km^2 (Figure 4.17). This indicates that DDMS could indeed lie between 10-13 km at the eastern and western margins of the profile and reach 20-30 km depth at the central part of the basin.

Other authors, however, reach different conclusions. Spectral analysis in Ebbing et al. (2009) shows that DDMS is shallowing from 20 km at the coastal region to 17-19 km at the Vøring margin and to 16 km further oceanwards. Thermal modelling in Gernigon et al. (2006), at the same time, indicates that Curie depth lies between 20-30 km beneath the Vøring Basin and deepens to 30-40 km under the Trøndelag Platform. Comparing these values with depths estimated here, reliability of spectral analysis results can be questioned. The method is affected by uncertainties related to technique and conditions which might not be satisfied. Moreover, the magnetic spectrum in this study area could rather be sensitive to the high magnetic middle crustal layer as opposed to relatively low and homogeneous magnetization in the lower crust. In this way, DDMS could represent the base of the middle crust instead of the actual Curie depth.

[3]The actual power spectrum and slopes are shown in Appendix B.

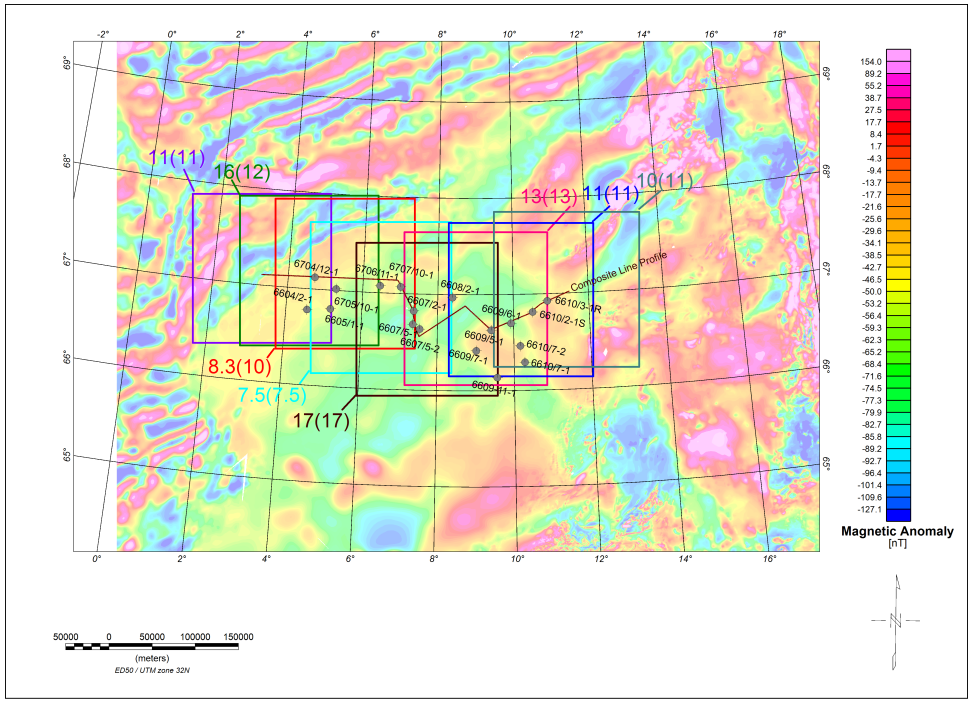

Figure 4.15: Depth to top of the deepest magnetic source in [km] using a window size of approximately 170×170 km^2. First number indicates the depth measured by the manual technique, while number in the brackets displays the value calculated automatically by Geosoft. Large scale elongated positive magnetic anomaly at the western part (wells 6704/12-1 and 6604/2-1) is correlated with the Gjallar Ridge, while smaller scale positive anomalies to the east indicate approximate locations of the Nyk High (well 6707/10-1) and the Utgard High (wells 6607/5-1, 6607/5-2). Anomalies at the eastern part of the profile show the Nordland Ridge (well 6609/5-1) and the Grønøy High (well 6610/2-1).

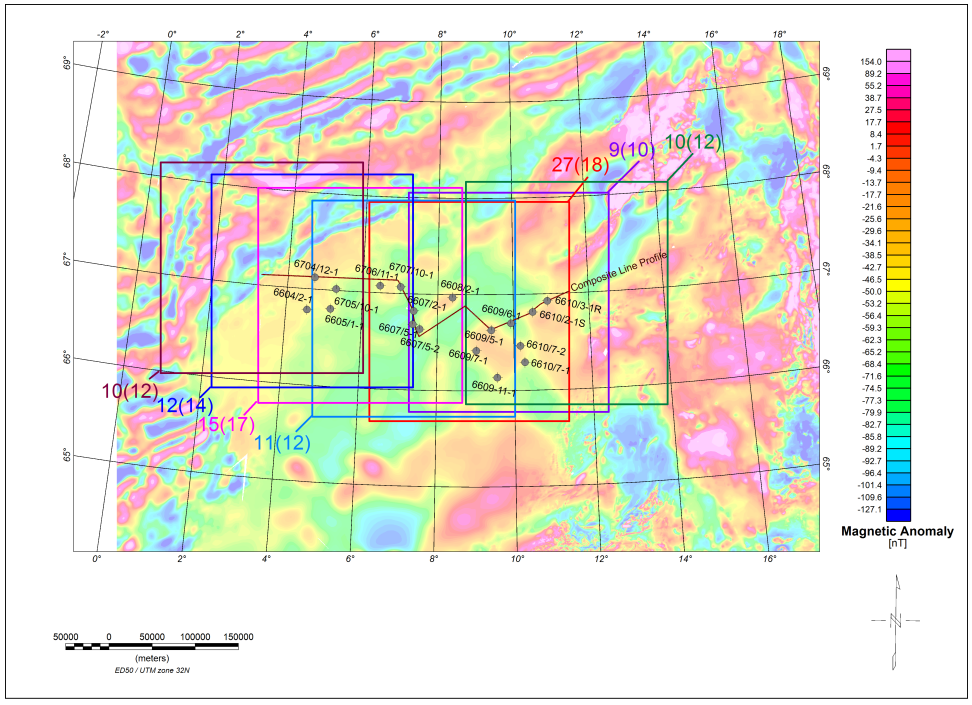

Figure 4.16: Depth to top of the deepest magnetic source in [km] using a window size of approximately 230×230 km^2. First number indicates the depth measured by the manual technique, while number in the brackets displays the value calculated automatically by Geosoft. Large scale elongated positive magnetic anomaly at the western part (wells 6704/12-1 and 6604/2-1) is correlated with the Gjallar Ridge, while smaller scale positive anomalies to the east indicate approximate locations of the Nyk High (well 6707/10-1) and the Utgard High (wells 6607/5-1, 6607/5-2). Anomalies at the eastern part of the profile show the Nordland Ridge (well 6609/5-1) and the Grønøy High (well 6610/2-1).

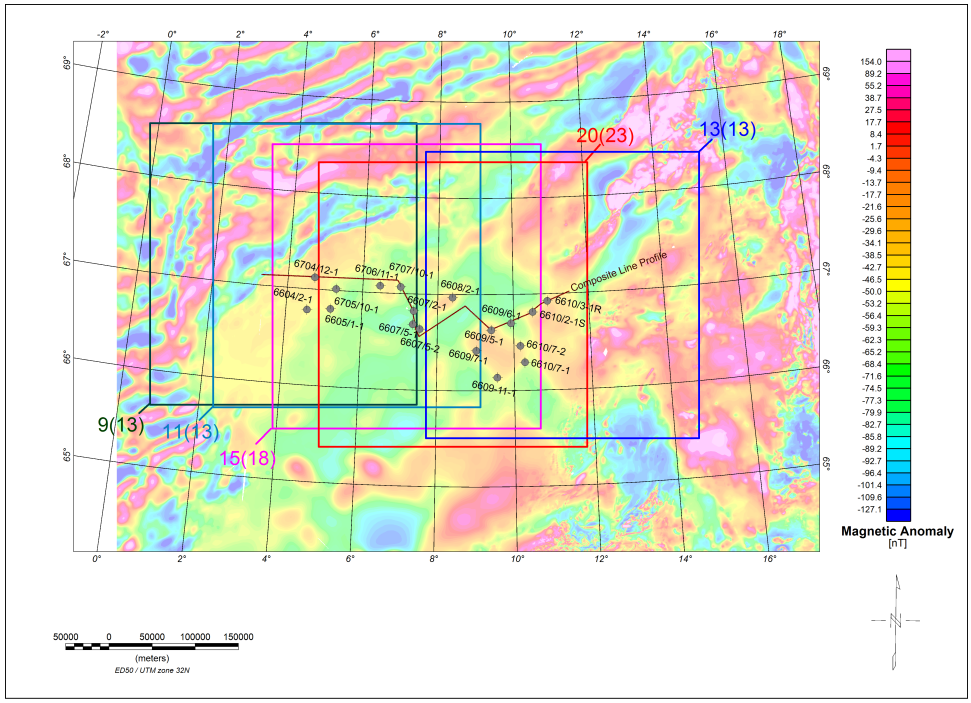

Figure 4.17: Depth to top of the deepest magnetic source in [km] using a window size of approximately 300×300 km^2. First number indicates the depth measured by the manual technique, while number in the brackets displays the value calculated automatically by Geosoft. Large scale elongated positive magnetic anomaly at the western part (wells 6704/12-1 and 6604/2-1) is correlated with the Gjallar Ridge, while smaller scale positive anomalies to the east indicate approximate locations of the Nyk High (well 6707/10-1) and the Utgard High (wells 6607/5-1, 6607/5-2). Anomalies at the eastern part of the profile show the Nordland Ridge (well 6609/5-1) and the Grønøy High (well 6610/2-1).

4.5 The Final Model

Current section presents the final density and magnetization model (Figures 4.18-4.19). This serves as an important step for understanding the crustal structure and subsequent choice of thermal parameters which are discussed in Chapter 5.

Geometry of the basalts at the Vøring Marginal High is modelled in accordance with the OBS data. Ocean Drilling Program (ODP) site 642E located 25 km from the western margin of the profile as shown on Figure 3.2 has drilled almost 1 km of those volcanic rocks and proved densities to range from 1.76 to 3 g/cm^3 in the upper seaward dipping reflectors (SDR) section and from 2.02 to 2.94 g/cm^3 in the lower basalt unit (Eldholm et al., 1987). The average values in this case are 2.66 g/cm^3 and 2.44 g/cm^3 accordingly. Choosing basalt's magnetic parameters is less straightforward. In total, there are identified 118 different flows, 7 dykes and 12 volcaniclastic sections from the ODP site, which result in complex magnetic properties outline (Schönharting et al., 1989). However, neither natural remanence magnetization nor susceptibility values observed in the well can create a sharp negative magnetic anomaly observed at the margin (Figures 3.3, 4.18). Therefore, it was decided to manipulate the properties to fit the observed anomaly.

Sediments are modelled according to the density study and choice of the parameters is described in Section 4.2. Except for the Naust and Kai formations showing lateral density changes, values are expected to increase with depth. At the same time, magnetic susceptibility of sedimentary cover is set to 0, as its contribution to magnetic anomaly is negligible.

Interpretation of the crustal structure relies heavily on the OBS data. The only definite crustal sign on reflection seismic data is a high amplitude T-reflector located beneath the Gjallar Ridge. This is interpreted as top of the high velocity lower crustal body (Gernigon et al., 2004; Abdelmalak et al., 2017). In addition to that, there are indications of shallower basement at the Utgard High and the Nordland Ridge-Grønøy High area. However, those are less certain.

Crustal densities are based on common igneous and metamorphic rock values (Hinze et al., 2013) and are matched with what has been used by other authors (Zastrozhnov et al., 2018; Ebbing et al., 2006; Maystrenko et al., 2018a). These densities are in a good agreement with the OBS velocity trends. Relatively low velocity and low density crust is likely to have felsic origin, and therefore could be interpreted as either upper or middle continental crust. Higher velocity units, on the contrary, are usually correlated with lower continental crust of mafic composition. Even though the HVLC has several alternative explanations as described in Chapter 2, most of these theories agree on mafic origin.

In contrast to density, magnetic susceptibility of the crustal rocks is a test variable. However, extensive onshore studies of Norwegian bedrock show that the upper crust is likely to be low magnetic (0.01-0.003 SI) Caledonian basement, while large anomalies are likely to be related to the high magnetic (0.03 SI) Precambrian basement (Olesen et al., 2010a). This concept is supported by testing the modelling variables. Due to its geometry the upper crust is unlikely to be the cause for variations in magnetic response. Similarly, geometry of the lower crust can not be correlated with magnetic anomaly shape. Consequently, magnetization has a different source - probably the Precambrian basement. In this way, the high magnetic middle crust is added to the basement structure and modelled according to measured magnetic anomaly.

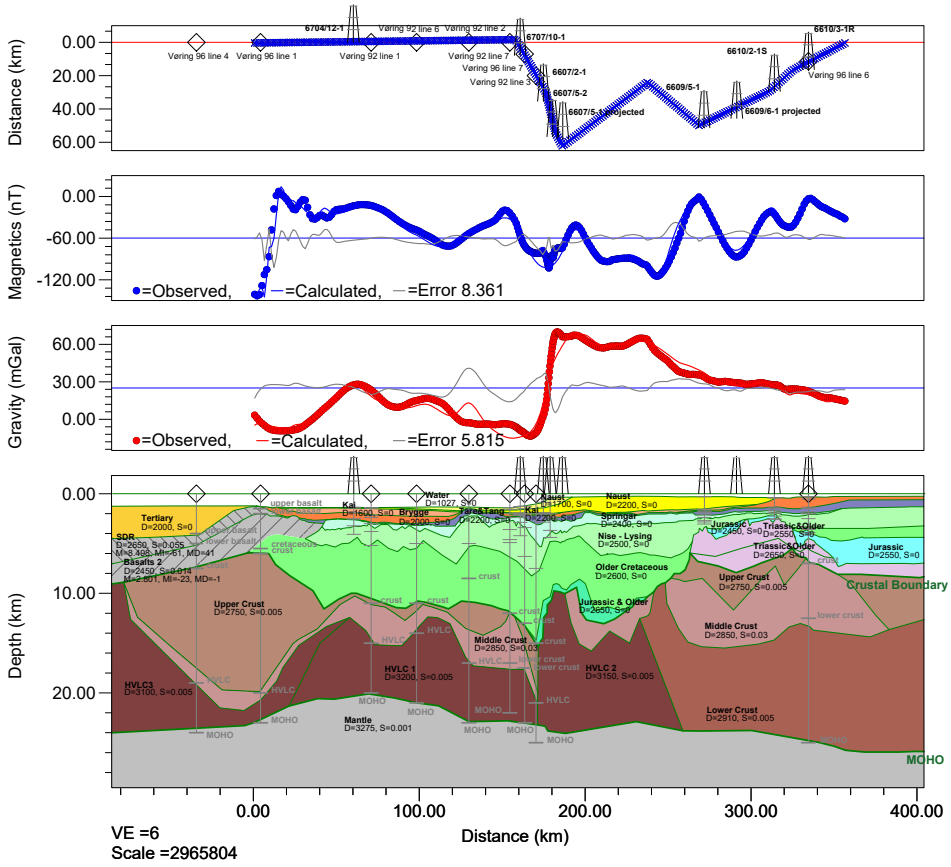

Figure 4.18: 2D density and magnetic model. The uppermost section shows profile location, wells and intersections with OBS profiles from Mjelde et al. (1997), Mjelde et al. (1998) and Mjelde et al. (2003). Panels in the middle present modelled and observed magnetic and gravity anomalies. Lowermost display gives an overview of modelled units and indicates their susceptibility and density. Interfaces interpreted from OBS data are displayed with grey color.

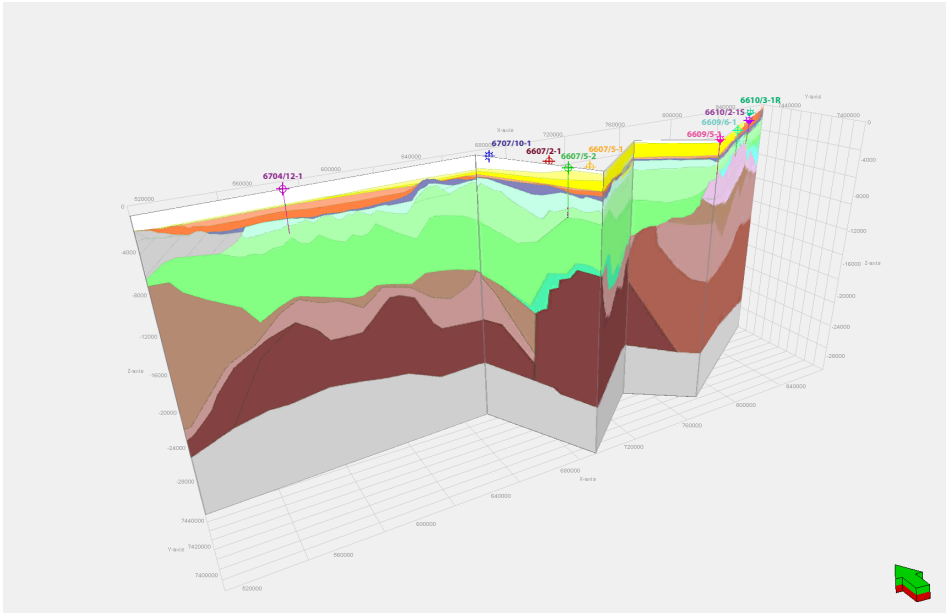

(a)

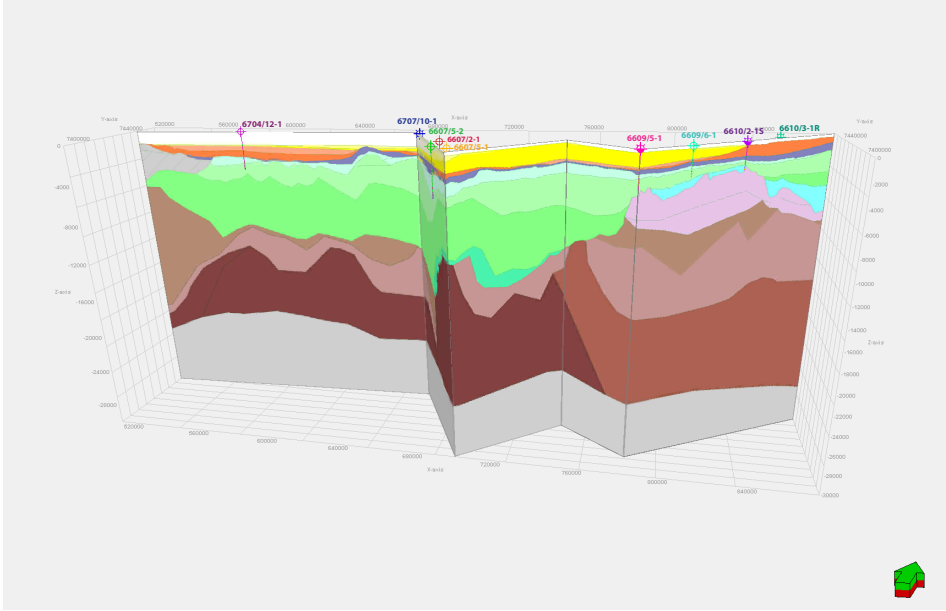

(b)

Figure 4.19: 2D model from Figure 4.18 displayed in 3D. Arrow points to North.

Mantle parameters are set to typical peridotite values (Hinze et al., 2013). Although it is common to believe that magnetic susceptibility of mantle rocks is close to 0, Ferré et al. (2014) argue against this assumption on the basis of mantle xenoliths analysis. In this way, mantle is considered to be low magnetic down to Curie depth.

Taking into account Curie isotherm depth estimated in previous section leads to slightly modified magnetic model (Figure 4.20). The model proves that high magnetization is likely to be constrained by the middle crust, as differences in calculated magnetic signals are minor. However, in order to resolve geological meaning of the spectral analysis results, they should be discussed in relation to the thermal modelling outcome.

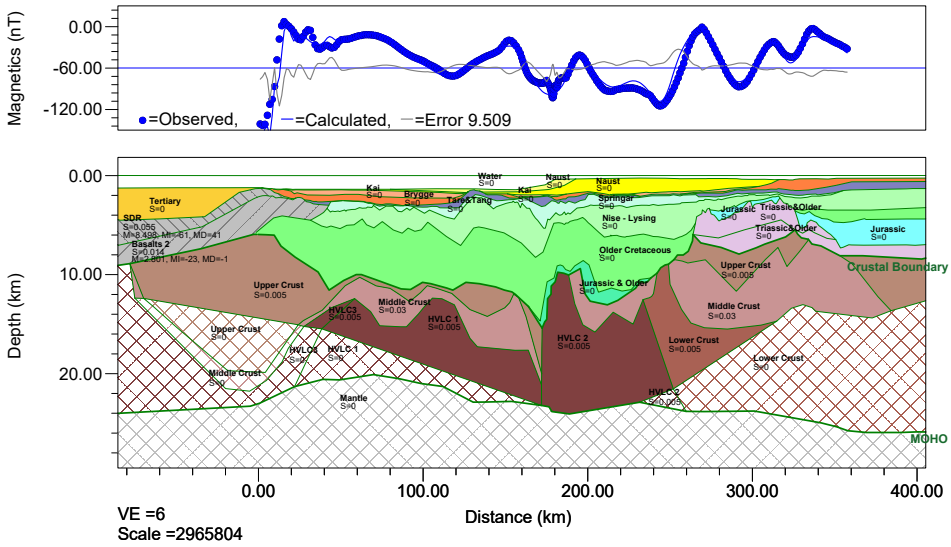

Figure 4.20: Alternative magnetic model. Uppermost panel presents modelled and observed magnetic anomaly. Lowermost display gives an overview of modelled units and indicates their susceptibility.

Chapter 5

Discussion and Thermal Profile

5.1 Crystalline Structure

Based on the results presented in Chapter 4, the crust is subdivided into four different units with properties listen in Table 5.1. In order to evaluate whether observed heat flow profile is related to crustal composition, it is important to have conceptual understanding of what lithologies those rocks are represented by and tectonic events leading to their formation.

Unit	ρ in [kg/m^3]	k in SI	V_{int} in [km/s]
Upper Crust	2750	0.005	6-6.2
Middle Crust	2850	0.03	6-6.5
Lower Crust	2900	0.005	6.8
HVLC	3000-3200	0.005	7.1-7.2

Table 5.1: Properties of the modelled crustal layers (Figure 4.18).

There are only few wells offshore Norway reaching basement rocks. Majority can be classified as metasediments, while few wells encounter intrusive igneous rocks such as granites and diorites (Slagstad et al., 2008). At the same time, uplifted basement rocks onshore have been researched extensively. Skilbrei et al. (1991) study Precambrian rocks of the Northern Vestranden and conclude that high susceptibility (0.03-0.08 SI) rocks are likely to be high grade (amphibolite to granulite facies) prograte metamorphism orthogneisses and migmatitic gneisses of granitic to tonalitic composition. Moreover, according to this work, gneisses which have undergone early retrogression during the Caledonian collapse exhibit high magnetization, while late retrogression leads to low magnetization rocks, where silicates have replaced magnetite. In addition to that, Olesen et al. (1991) study amphibolite-granulite facies transition of Precambrian intermediate gneisses at the Vesterålen area in northern Norway. The authors are able to define a location of the

the boundary between the two facies, as well as study differences in their petrophysical properties. It is concluded that amphibolite-granulite transition is represented by density and susceptibility increase from 2750 kg/m^3 to 2810 kg/m^3 and 0.0015 SI to 0.03 SI accordingly. Taking all this information into consideration, high magnetic middle crust is interpreted to contain high grade granulite facies granitoid gneisses, while low magnetic upper crust is assumed to be related to retrograde amphibolite facies gneisses and metasedimemts.

Due to high velocity values, the HVLC is supposed to have mafic origin. Moreover, it is likely to contain lenses of eclogite as those have extremely high pressure wave velocities (Fountain et al., 1994). This concept is supported by low magnetic susceptibility of eclogite rock (Clark and Emerson, 1991) and eclogites observed at several locations on Norwegian mainland. Studying these rocks in the Western Gneiss Region, Dewey et al. (1993) detect densities of 3.1-3.3 g/cm^3 and velocities of 7.8 to 8.1 km/s. In addition to that, the authors build a numerical model in order to explain the Caledonian orogeny and collapse, which involves formation of eclogite during the shortening phase, eclogite-granulite/amphibolite transform under the the extensional collapse, and vertical thinning bringing amphibolite and eclogite lenses to shallower levels.

It is unclear whether the lower crust should be considered separately from the lower crustal body. Even though modelled densities differ by almost 200 kg/m^3, susceptibility values are similar. It is possible that the HVLC is essentially similar to rocks of the "normal" lower crust, with velocities and densities elevated by higher eclogite and possibly peridotite content. Even though peridotite is ultramafic mantle rock, it is sometimes observed within crustal units, as evident from Leka, Trøndelag (Birkeland, 1958). Morover, velocities and densities are likely to be elevated by igneous intrusions. Several authors have discussed potential presence of younger mafic rocks injected into the lower crust of the western Vøring Basin either prior to or during the continental break-up (Abdelmalak et al., 2017; Gernigon et al., 2004; Mjelde et al., 2009). Sills and shallow basalts observed as prominent high amplitude positive reflections on seismic data can serve as important indicators (Figure 4.2). At the same time, it can not be excluded that the two rock facies formed under different conditions at different times and were juxtaposed against each other as a result of complex extensional tectonism.

5.2 Thermal Properties of Basement Rocks

Generally, thermal conductivity is related to mineralogy, where quartz, ore, ritule and spinel have high thermal conductivities, while biotite, nepheline and polyhalite express lower values (Schön, 2015). In this way, felsic rocks are considered to have higher k when compared to mafic rocks. However, complex temperature, pressure and porosity effects make this assumption frequently invalid.

The KONTIKI project carried out as a cooperation project of by NGU and StatoilHydro (now Eqiunor) presents the results of temperature logging and heat flow calculations for several onshore wells (Olesen et al., 2007). As thermal conductivity is essential parameter in this case, it was measured on numerous rock samples recovered from the subsurface. Of particular interest are wells Leknes, Drag, Sulitjelma and Bleikvassli located between latitudes of 68°N at Leknes, Lofoten and 66°N at Bleikvasslia. Drag has logged 800m of granitic gneisses with mean k of 2.8 W/mK, while Leknes has penetrated different orthogneisses with the majority showing k of 2.2 W/mK. However, deeper fine-grained gneisses and granodiorites in Leknes well exhibit higher values reaching a maximum of 3.6 W/mK. Silutjelma has mostly drilled through mica shists with highly anisotropic thermal conductivities varying from 1.9 to 3.6 W/mK and a mean of 2.4 W/mK. At the same time, Bleivassli discovered mica shists, mica gneisses and marbles showing k of 2.5 W/mK and graphite shists with occasionally extreme 6.7 W/mK. Several different lithologies and thermal conductivities are also encountered by four offshore wells reaching basement in the Norwegian Sea (Slagstad et al., 2008). While conductivites for metasediments are spread between 2.8 and 5.4 W/mK, granites and quartz diorites have k of 3.6 and 2.8-2.9 W/mK accordingly. In this way, it becomes evident that thermal conductivity varies tremendously between different rocks and should be set and tested according to expected lithology.

Radiogenic heat production is related to quantity of decaying isotopes of radioactive elements uranium, thorium and potassium (Bücker and Rybach, 1996). Čermák and Rybach (1982a) present practical results of estimating A in different rock samples. The main conclusion is that acidic rocks express much higher values when compared to basic rocks, while metamorphic rocks show lower estimates due to absorption and redistribution of radioactive elements.

Slagstad (2008) compiles a radiogenic heat production map of different Norwegian geological provinces (Figure 5.1). Assuming that the upper crust is mostly composed of Caledonian metasediments, A is expected to be between 1 and 2 μW/m^3. On the basis of spatial proximity and rock properties' similarities, the middle and lower crust could either be related to Lofoten anorthosite-mangerite-charnockite-granite complex or Western Gneiss Region, which have average A of 0.1-1 μW/m^3 and 1-1.5 μW/m^3 respectively.

Following this reasoning, A and k parameters are tested and discussed in the next section.

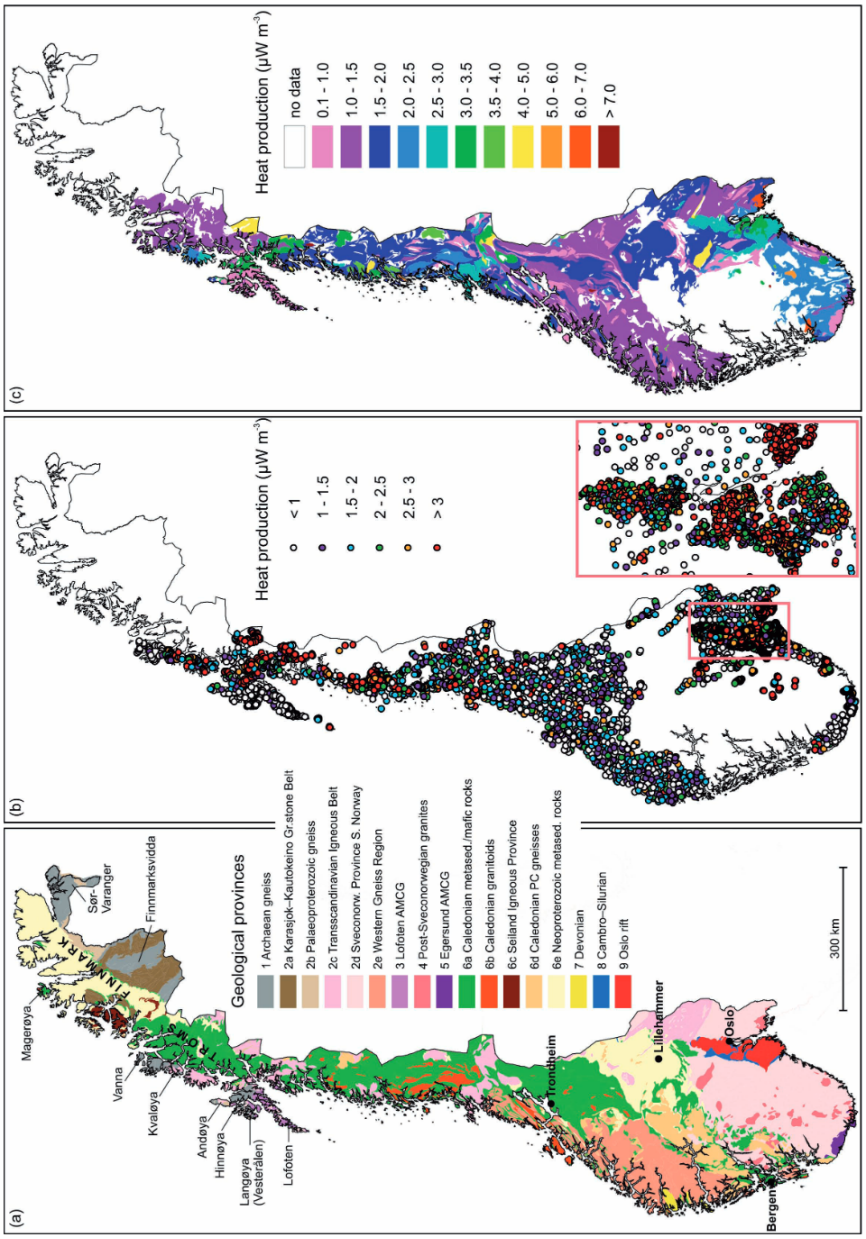

Figure 5.1: Geological provinces of Norway (a), their heat production from samples (b) and their average heat production (c), after Slagstad (2008).

5.3 Temperature and Heat Flow Trends

Thermal modelling is based on temperature and heat flow trends estimated previously during the Specialization Project (Chernyshova, 2018). As the modelling depends on crustal structure defined along the composite line (Figure 4.18), wells located in a close range to the profile are used: 6704/12-1, 6707/10-1, 6607/2-1, 6607/5-2, 6607/5-1, 6609/5-1, 6609/6-1, 6610/2-1S and 6610/3-1R. Consequently, calculations are extending from TD's through the lowermost sediments and down into the mantle with parameters summarized in Table 5.2, while k and A from the well logs remain intact. Values for deep Cretaceous and Triassic sediments and undifferentiated Jurassic and older rocks are set to 2.5 W/mK and 1.5 μW/m^3 as those are the terminate k and A for the majority of wells. Moreover, porosity in deepest sediments is expected to be 0 as a consequence of extensive compaction at such great depths.

Unit	k [W/mK]	A [μW/m^3]
Upper units	modelled in Chernyshova (2018)	
Older Cretaceous	2.5	1.5
Jurassic and Older	2.5	1.5
Triassic and Older	2.5	1.5
Upper Crust	2.7	2
Middle Crust	3	1.5
Lower Crust	3.1	0.5
HVLC	3.1	0.5
Mantle	4	0.025

Table 5.2: Thermal parameters used in the temperature and heat flow modelling.

As a first try, upper crustal k is chosen to be 2.7 W/mK based on the KONTIKI wells and Bücker and Rybach (1996). The middle crust is modelled with 3 W/mK as it is a common value for high grade metamorphic rocks (Bücker and Rybach, 1996). Lower crustal eclogites, at the same time, are expected to show 3.1 W/mK (Bücker and Rybach, 1996). A values are set to 2 and 1.5 μW/m^3 for the upper and middle crust following the discussion in Section 5.2 and to 0.5 μW/m^3 for the lower crust based on the experimental data for high grade mafic rocks (Bücker and Rybach, 1996). Mantle k and A are set to typical peridotite's 4 W/mK and 0.025 μW/m^3 (Čermák and Rybach, 1982a,b). The results for this case are shown on Figure 5.2. The uppermost curves indicate the values at 2249 m below the seabed as this is the minimum seabed-total depth distance among all the wells, while middle curve shows thermal trends at the MOHO. In addition to that, the modelling is extended to an arbitrary depth of 80 km in order to evaluate how temperature and heat flow profiles develop deeper in the mantle. It becomes clear that HF anomalies persist with depth, which leads to amplification of thermal anomalies. At 2249 m below the seabed maximum temperature difference across the profile is 50 °C, at the MOHO it rises to 262 °C, while at 80 km it reaches 672 °C. It is important to note that the LAB is expected to be shallower than 80 km depth at the western and eastern parts of the profile, assuming the LAB corresponds to roughly 1300 °C isotherm (Turcotte and Schubert, 2002).

This scenario shows that variation in crustal composition and consequently crustal heat

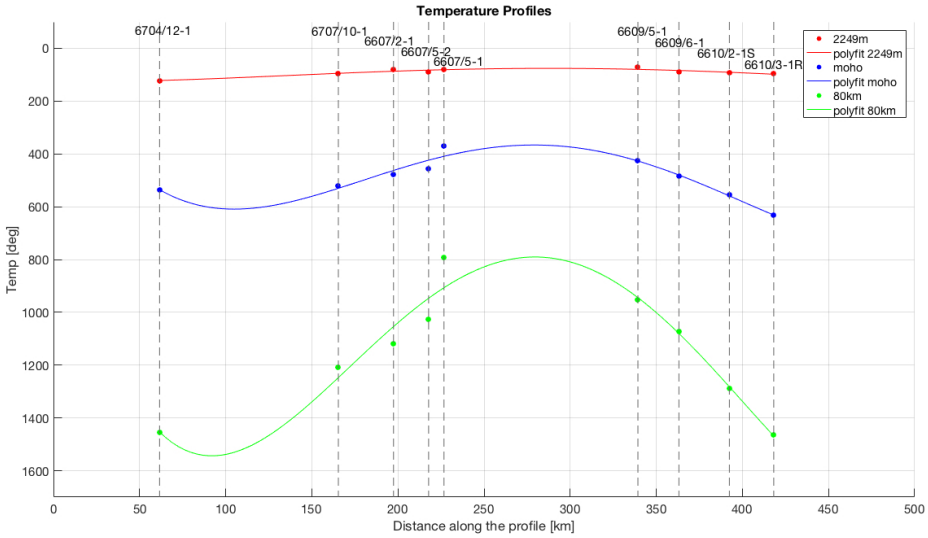

(a) Temperature

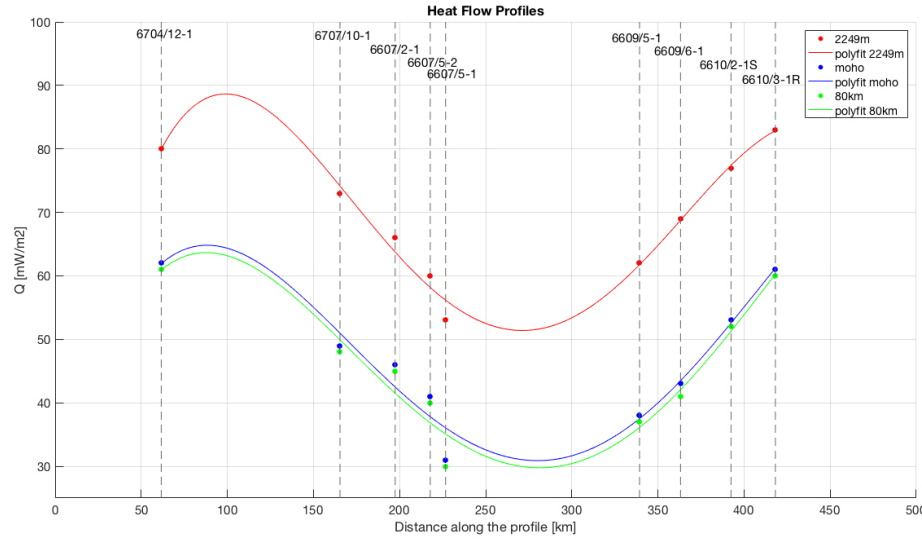

(b) Heat flow

Figure 5.2: Temperature and heat flow across the profile at 2249 MDSS, MOHO and 80 km depth. Modelled with parameters in Table 5.2.

production is unable to explain the particular thermal trends observed along the Vøring Basin. Moreover, source of the anomalies is likely to lie within the lithospheric mantle or the LAB position. Similar conclusion is reached by Maystrenko et al. (2018b), who observes that temperature deviations at the Lofoten-Vesterålen area are controlled by the LAB among other things. According to thermal model presented there, the LAB deepens from 60-70 km at the continent-ocean boundary (COB) (west of well 6704/12-1) to 90-95 km at the Nordland Ridge (well 6609/5-1). Moreover, the authors refer to an upper mantle low velocity anomaly beneath the Lofoten-Vestfjørden area (close to well 6610/3-1R) as observed by Hejrani et al. (2017) and Bannister et al. (1991). According to Hejrani et al. (2017), the Lofoten Slow Spot is associated with up to 2% S-wave velocity decrease, which in its turn can generate 200 °C temperature anomaly. In this case, temperature and HF decrease from the Vøring margin towards the Nordland Ridge can partly be attributed to deepening of the LAB, while elevation of temperatures towards the Vestfjørden Basin is correlated with a possible mantle anomaly, which is not indicated from the potential field modelling.

Maystrenko et al. (2018b) also point out that temperatures are heavily affected by Cenozoic erosional and depositional patterns. At the Utgard High modelled negative effect reaches 50-45 °C at 10 km depth, while at the Vestfjørden Basin temperatures are expected to be elevated by more than 25 °C at 10-25 km depth (Maystrenko et al., 2018b). This factor can influence borehole temperatures which can lead to under- and overestimation of deeper temperatures using the method described here. Looking at the effects modelled by (Maystrenko et al., 2018b) it is possible to assume that the bottomhole temperature in well 6610/3-1R is amplified by 10 °C due to erosion. Modelled surface HF, in this case, is expected to be 4 mW/m^2 higher than the thermal equilibrium value. Accounting for this effect leads to temperature of 597 °C and HF of 57 mW/m^2 at the MOHO, and to 1375 °C and 56 mW/m^2 at 80 km depth (Figure 5.3). At the same time, if temperature in well 6607/5-1 at the Utgard High is lowered by 10 °C due to active deposition, modelled surface HF is expected to be decreased by 7 mW/m^2. Calibration results in 434 °C temperature and 38 mW/m^2 HF at the MOHO and 955 °C and 37 mW/m^2 at 80 km depth (Figure 5.3). Similar adjustments for neighbouring well 6607/5-2 produce surface HF of 69.5 mW/m^2 as opposed to 64.5 mW/m^2. Moreover, deeper estimates are also modified showing T and HF of 507 ° C and 47 mW/m^2 at the MOHO and 1267 °C and 45 mW/m^2 at 80 km below the seabed (Figure 5.3). Thus, it is possible that deeper temperature anomalies are slightly exaggerated by unequilibrated shallower temperatures due to erosional and depositional effects. Nonetheless, as evident from Figure 5.3 regional temperature and HF trends showing lows at the Utgard High and highs at the Grønøy High are likely to remain even after the correction.

Another interesting fact is that modelled Curie temperature depths are much higher than what spectral analysis indicates (Figure 5.4). This assumes Curie temperature of 580 °C for magnetite, which is the most common magnetic mineral (Hunt et al., 1995). However, magnetite is expected to have high titanium content within mafic igneous rocks and some titanium in felsic igneous rocks (Grant, 1985). This will lower Curie temperature of the mineral within the crustal layers. It is unreasonable, however, to expect that Curie temperature can drop to 380-420 °C as required to match the DDMS estimated from the spectral analysis with the modelled temperatures. Consequently, the DDMS values are

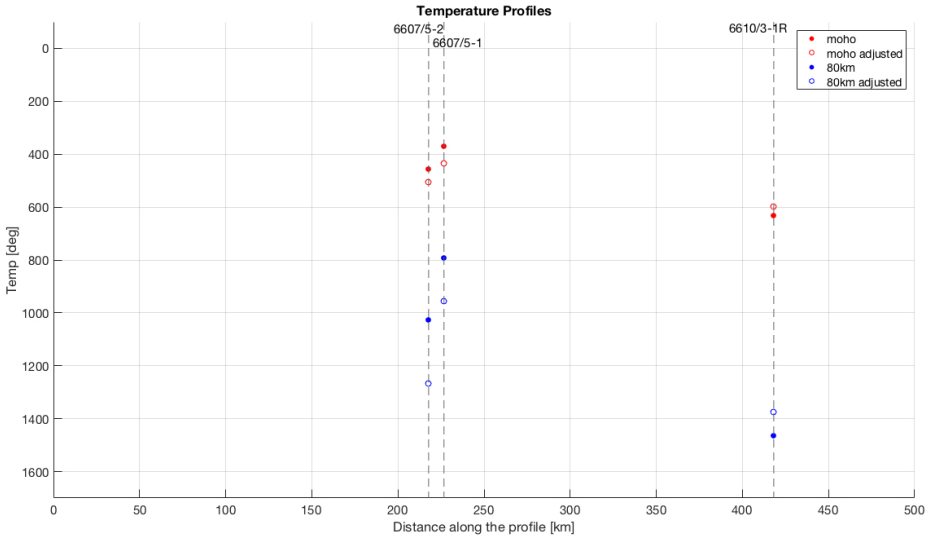

(a) Temperature

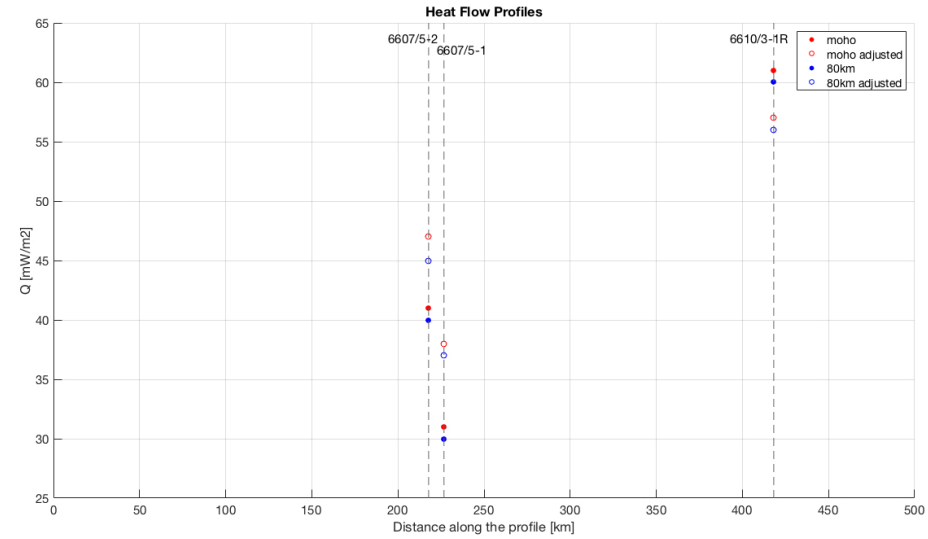

(b) Heat flow

Figure 5.3: Temperature and heat flow modelling adjusted for erosional and depositional effects. Equilibrium temperature is assumed to be 10 °C higher for wells 6607/5-2 and 6607/5-1 and 10 °C lower for well 6610/3-1R.

likely to show the base of the high magnetic middle crust and not the actual Curie depth.

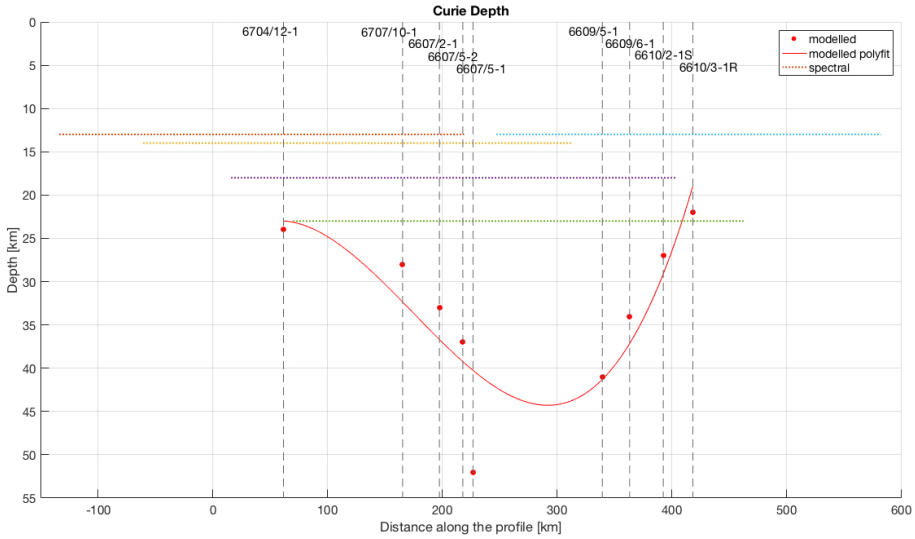

Figure 5.4: DDMS from spectral analysis and Curie depth modelled with parameters in Table 5.2.

5.4 Alternative Explanations

It is important to consider alternative scenarios. Possibly, real thermal properties are different from the ones used for the modelling. Perhaps, crustal inhomogenities and therefore variation in thermal parameters could explain observed temperature and HF trends.

Assuming roughly uniform 40 mW/m^2 HF from the mantle, crustal rocks are expected to produce approximately 20 mW/m^2 more heat at the eastern and western edges of the model in order to level out the MOHO HF curve (Figure 5.2). The lower crust and HVLC being deep basic rocks are unlikely to generate that amount of radiogenic heat. Consequently, analysis should focus on the upper and middle crustal units. As evident from Figure 5.1, A can vary by as much as 5 μW/m^3 between neighbouring geological provinces in Norway and even reach extreme levels locally (Slagstad, 2008).

At the Gjallar Ridge the model predicts 2680 m of upper and middle crust as evident from Figure 5.5, and to produce 20 mW/m^2 excess radiogenic heat, A is expected to be 7.5 μW/m^3 in contrast to modelled 1.5-2 μW/m^3. On the Grønøy High, on the contrary, model indicates 6600 m of middle crust below the sedimentary cover, whose A is expected to be 4.5 μW/m^3 to produce enough radiogenic heat to flatten MOHO HF. Similar analysis for wells 6707/10-1 and 6610/2-1S shows that upper and middle crustal A of 3.5-4 μW/m^3 is required to lower mantle HF to 40 mW/m^2. In this way, to constrain the model with constant basal heat flow and eliminate modelled MOHO temperature anomalies, average A in upper and middle crust is expected to vary from 7.5 μW/m^3 at the Gjallar Ridge to 3.5-4 μW/m^3 towards the center of the profile and increase again to 4.5 μW/m^3 at the Grønøy

High. Apart from the Svecononorwegian Province and Post-Sveconorwegian granites in Southern Norway, Slagstad (2008) observed values of that range in rocks of the Transscandinavian Igneous Belt as shown on Figure 5.1. Those are described as granitoid rocks formed in late Paleoproterozoic in relation to tectonism of convergent Baltica boundary (Åhäll and Larson, 2000). Even though granitoids belonging to Transscandinavian Igneous Belt and other Precambrian granitoids could compose significant part of the high magnetic middle crustal layer, it is unlikely that majority of rocks will show A above 4 μW/m^3.

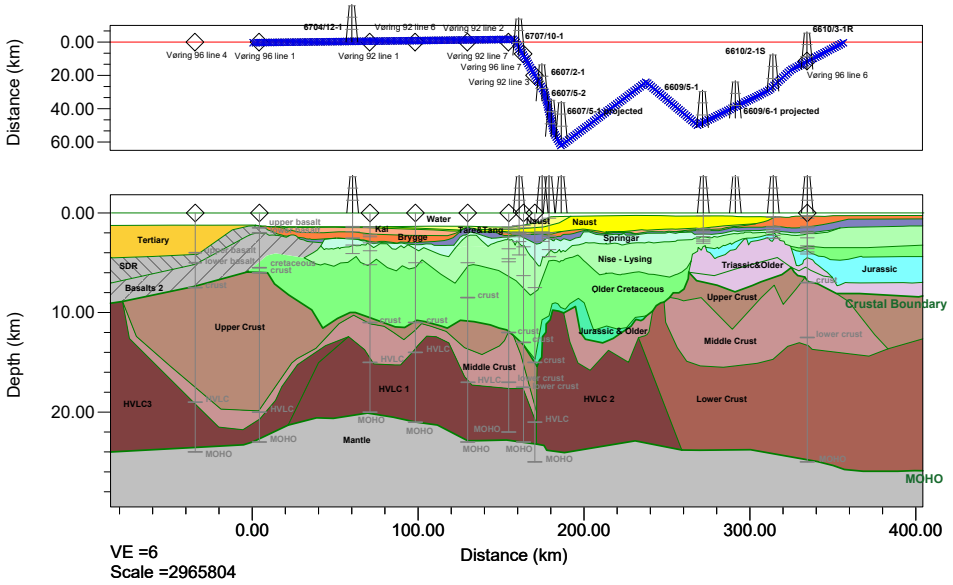

Figure 5.5: Crustal structure resulting from density and magnetic modelling. The uppermost section shows profile location, wells and intersections with OBS profiles from Mjelde et al. (1997), Mjelde et al. (1998) and Mjelde et al. (2003). Lowermost display gives an overview of modelled units. Interfaces interpreted from OBS data are displayed with grey color.

Chapter 6

Conclusion

The potential field modelling showed that the crustal structure of the Vøring Basin is likely to be composed of four different rock types. The upper crust is concluded to be low magnetic amphibolite facies felsic gneisses and Caledonian metasediments. Middle crust, at the same time, is expected to be higher grade Precambrian granitoid and tonalitic rocks having high magnetic susceptibility. Lower crust, on the contrary, is interpreted to be lower magnetic older continental crust of mafic composition subjected to high grade metamorphism during the Caledonian orogeny and collapse. Moreover, in the western part of the section the lower crust is expected to be heavily affected by igneous intrusions associated with the last stages of the continental rifting.

Correlating these crystalline rocks with onshore samples and relying on the experimental data assists in defying the thermal parameters for temperature and heat flow modelling. Based on the modelling results, it becomes evident that significant variations in crustal composition are unlikely to cause the positive thermal anomalies at the Gjallar Ridge, the Grønøy High and in the souther Vestfjorden Basin. Consequently, the source of the anomalies is expected to lie within the mantle. Deepening of the LAB from the COB towards the mainland and a slow spot within the mantle beneath the Lofoten-Vestfjørden area could create this particular thermal profile. Furthermore, the anomalies are likely to be amplified by erosional and depositional effects as introduced by Maystrenko et al. (2018b). It is interesting that Maystrenko et al. (2018b) also place the source of the anomalies within the mantle, as the authors did not base their model on the well data as opposed to the methodology presented here. The fact that different approaches lead to the similar conclusion makes this concept even more convincing. However, to confirm this hypothesis, the mantle structure should be investigated further. It is necessary to verify the LAB geometry, as well as study the Lofoten Slow Spot and its geological meaning.

At the same time, the upper and middle crust could potentially create enough radiogenic heat to produce the observed thermal anomalies, if it is almost entirely composed of granitoid rocks with high radiogenic heat production, as observed within the Transscandinavian Igneous Belt. Even though this amount of granite is possible when looking at the onshore provinces, nature of its locally high radiocative elements content should be

researched. Possibly, analysis of seismic sections joining the major granitoid batholiths with the basement of the Vøring Basin can give grounds for the connection between the two. This can be followed by potential field modelling justifying the scenario where upper and middle crust have density and magnetic properties similar to the onshore granite rocks with high radiogenic heat production.

This work also shows that the DDMS calculations based on the method introduced by Spector and Grant (1970) do not indicate the actual Curie depth. More likely, they show the base of the high magnetic middle crust or simply erroneous estimates due to numerous uncertainties. Nevertheless, spectral methods for Curie depth computation can not be completely discarded. Several other modified techniques exist, which can result in more accurate predictions. For example, as tested by Salazar et al. (2017), the Forward Modelling method gives more accurate estimates than the Centroid and the Spectral Peak methods.

In addition to that, in order to confirm that the thermal trends are caused by either crustal or lithospheric sources, it is necessary to controvert a scenario where high heat flow at the Gjallar Ridge and the Grønøy High is explained by fluid convection and advection. Modern seismic can assist in better fault interpretation and analysis, which can be used to model the fluid effect.

In this way, origin of the temperature and heat flow anomalies remains undetermined but the two possible explanations are suggested here. However, increased interest towards the tectonic development of the Norwegian Sea may lead to a better understanding of the crustal structure. Furthermore, better seismic and potential field data, as well as improved integration of various geophysical datasets can help to build a detailed picture of the litosh-peric structure and ensure a more conclusive thermal model.

Bibliography

Abdelmalak, M. M., Faleide, J. I., Planke, S., Gernigon, L., Zastrozhnov, D., Shephard, G. E., Myklebust, R., 2017. The T-Reflection and the deep crustal structure of the Vøring Margin, offshore mid-Norway. Tectonics 36 (11), 2497–2523.

Åhäll, K.-I., Larson, S. , 2000. Growth-related 1.85–1.55 Ga magmatism in the Baltic Shield; a review addressing the tectonic characteristics of Svecofennian, TIB 1-related, and Gothian events. GFF 122 (2), 193–206.

Bannister, S. C., Ruud, B. O., Husebye, E. S., 1991. Tomographic estimates of sub-Moho seismic velocities in Fennoscandia and structural implications. Tectonophysics 189 (1-4), 37–53.

Beardsmore, G. R., Cull, J. P., 2001. Crustal Heat Flow: A Guide to Measurement and Modelling. Cambridge University Press.

Birkeland, T., 1958. Geological and petrological investigations in northern Trøndelag, western Norway. Norsk Geologisk Tidsskrift 38, 328–420.

Blakely, R. J., 1996. Potential Theory in Gravity & Magnetic Applications. Cambridge University Press.

Blystad, P., Brekke, H., Færseth, R. B., Larsen, B. T., Skogseid, J., Tørudbakken, B., 1995. Structural elements of the Norwegian continental shelf. Part II: The Norwegian Sea Region. Norwegian Petroleum Directorate Bulletin 8.

Brekke, H., 2000. The tectonic evolution of the Norwegian Sea continental margin with emphasis on the Vøring and Møre Basins. Geological Society, London, Special Publications 167, 327–378.

Brekke, H., Dahlgren, S., Nyland, B., Magnus, C., 1999. The prospectivity of the Vøring and Møre basins on the Norwegian Sea continental margin. Geological Society, London, Petroleum Geology Conference series 5 (1), 261–274.

Bücker, C., Rybach, L., 1996. A simple method to determine heat production from gamma-ray logs. Marine and Petroleum Geology 13 (4), 373–375.

Čermák, V., Rybach, L., 1982a. Radioactive heat generation in rocks. In: Angenheister, G. (Ed.), Physical Properties of Rocks. Vol. 1 of Landolt-Bornstein Numerical Data and Functional Relationships in Science and Technology, Group V. *(Hellwege, K.-H., Series Editor)*. Springer, pp. 353–371.

Čermák, V., Rybach, L., 1982b. Thermal properties: thermal conductivity and specific heat of minerals and rocks. In: Angenheister, G. (Ed.), Physical Properties of Rocks. Vol. 1 of Landolt-Bornstein Numerical Data and Functional Relationships in Science and Technology, Group V. *(Hellwege, K.-H., Series Editor)*. Springer, pp. 305–343.

Chernyshova, A., 2018. Potential causes for varying temperature gradient in the Vøring Basin, Norwegian Sea, attached in Appendix D.

Clark, D. A., Emerson, D. W., 1991. Notes on rock magnetization characteristics in applied geophysical studies. Exploration Geophysics 22 (3), 547–555.

Dalland, A., Worsley, D., Ofstad, K., 1988. A lithostratigraphic scheme for the Mesozoic and Cenozoic succession offshore mid- and northern Norway. Norwegian Petroleum Directorate Bulletin 4.

Dewey, J. F., Ryan, P. D., Andresen, T. B., 1993. Orogenic uplift and collapse, crustal thickness, fabrics and metamorphic phase changes: the role of eclogites. Geological Society, London, Special Publications 76 (1), 325–343.

Duffaut, K., Hokstad, K., Rune Kyrkjebø, R., Wiik, T., 2018. A simple relationship between thermal conductivity and seismic interval velocity. The Leading Edge 37 (5), 381–385.

Ebbing, J., Gernigon, L., Pascal, C., Olesen, O., Osmundsen, P. T., 2009. A discussion of structural and thermal control of magnetic anomalies on the mid-Norwegian margin. Geophysical Prospecting 57 (4), 665–681.

Ebbing, J., Lundin, E., Olesen, O., Hansen, E. K., 2006. The mid-Norwegian margin: a discussion of crustal lineaments, mafic intrusions, and remnants of the Caledonian root by 3D density modelling and structural interpretation. Journal of the Geological Society 163 (1), 47–59.

Eidvin, T., Riis, F., Rasmussen, E. S., 2014. Oligocene to Lower Pliocene deposits of the Norwegian continental shelf, Norwegian Sea, Svalbard, Denmark and their relation to the uplift of Fennoscandia: a synthesis. Marine and Petroleum Geology 56, 184–221.

Eldholm, O., Thiede, J., Taylor, E., Barton, C., Bjørklund, K., Bleil, U., Ciesielski, P., Desprairies, A., Donnally, D., Froget, C., et al., 1987. Site 642: Norwegian Sea. In: Proceedings of the Ocean Drilling Program, Initial Reports. Vol. 104. pp. 53–453.

Ferré, E. C., Friedman, S. A., Martin-Hernandez, F., Feinberg, J. M., Till, J. L., Ionov, D. A., Conder, J. A., 2014. Eight good reasons why the uppermost mantle could be magnetic. Tectonophysics 624, 3–14.

Fittall, M. E., Foss, K. O., Hendrich, J. H., Johannesen, J., Meisingset, I., Strønen, L. K., 1988. Geological Completion Report. Well 6607/5-1. http://factpages.npd.no/pbl/wellbore_documents/1064_6607_5_1_COMPLETION_REPORT_AND_LOG.pdf, last accessed: 2019-25-03.

Fountain, D. M., Boundy, T. M., Austrheim, H., Rey, P., 1994. Eclogite-facies shear zones-deep crustal reflectors? Tectonophysics 232 (1-4), 411–424.

Fristad, P., Pettersen, R. M., Finnesen, L., 1994. Completion Report. Well 6610/7-1 6610/3-1R. http://factpages.npd.no/pbl/wellbore_documents/2193_6610_3_1_R_COMPLETION_REPORT_AND_LOG.pdf, last accessed: 2019-05-13.

Geosoft Oasis Montaj, 2004. GM-SYS Gravity and magnetic modeling software user's guide. Vol. 4.9. Northwest Geophysical Associates, Inc.

Gernigon, L., Lucazeau, F., Brigaud, F., Ringenbach, J.-C., Planke, S., Le Gall, B., 2006. A moderate melting model for the Vøring margin (Norway) based on structural observations and a thermo-kinematical modelling: implication for the meaning of the lower crustal bodies. Tectonophysics 412 (3-4), 255–278.

Gernigon, L., Ringenbach, J.-C., Planke, S., Le Gall, B., 2004. Deep structures and breakup along volcanic rifted margins: insights from integrated studies along the outer Vøring Basin (Norway). Marine and Petroleum Geology 21 (3), 363–372.

Gernigon, L., Ringenbach, J.-C., Planke, S., Le Gall, B., Jonquet-Kolstø, H., 2003. Extension, crustal structure and magmatism at the outer Vøring Basin, Norwegian margin. Journal of the Geological Society 160 (2), 197–208.

Grad, M., Tiira, T., ESC Working Group, 2009. The Moho depth map of the European Plate. Geophysical Journal International 176 (1), 279–292.

Grant, F. S., 1985. Aeromagnetics, geology and ore environments, I. Magnetite in igneous, sedimentary and metamorphic rocks: An overview. Geoexploration 23 (3), 303–333.

Halland, E. K., Wenche, T. J., Fridtjof, R., 2013. CO2 Storage Atlas: Norwegian Sea. Norwegian Petroleum Directorate.

Hejrani, B., Balling, N., Jacobsen, B. H., England, R., 2017. Upper-mantle velocities below the Scandinavian Mountains from P- and S-wave traveltime tomography. Geophysical Journal International 208 (1), 177–192.

Hellestrand, T., Larsen, M., n.d. Completion Report. Well 6610/7-1. http://factpages.npd.no/pbl/wellbore_documents/12_01_Completion_Report_and%20Completion_log.pdf, last accessed: 2019-05-13.

Hinze, W. J., Von Frese, R. R. B., Saad, A. H., 2013. Gravity and Magnetic Exploration: Principles, Practices, and Applications. Cambridge University Press.

Hunt, C. P., Moskowitz, B. M., Banerjee, S. K., 1995. Magnetic properties of rocks and minerals. Rock physics & phase relations: a handbook of physical constants 3, 189–204.

Maystrenko, Y. P., Gernigon, L., 2018. 3-D temperature distribution beneath the Mid-Norwegian continental margin (the Vøring and Møre basins). Geophysical Journal International 212 (1), 694–724.

Maystrenko, Y. P., Gernigon, L., Nasuti, A., Olesen, O., 2018a. Deep structure of the Mid-Norwegian continental margin (the Vøring and Møre basins) according to 3-D density and magnetic modelling. Geophysical Journal International 212 (3), 1696–1721.

Maystrenko, Y. P., Gernigon, L., Olesen, O., Ottesen, D., Rise, L., 2018b. 3-D thermal effect of late Cenozoic erosion and deposition within the Lofoten-Vesterålen segment of the Mid-Norwegian continental margin. Geophysical Journal International 213 (2), 885–918.

McElhinny, M. W., McFadden, P. L., 1999. Paleomagnetism: Continents and Oceans. Vol. 73. Academic Press.

Mjelde, R., Digranes, P., Shimamura, H., Shiobara, H., Kodiara, S., Brekke, H., Egebjerg, T., Sørenes, N., Thorbjørnsen, S., 1998. Crustal structure of the northern part of the Vøring Basin, mid-Norway margin, from wide-angle seismic and gravity data. Tectonophysics 293 (3-4), 175–205.

Mjelde, R., Faleide, J. I., Breivik, A. J., Raum, T., 2009. Lower crustal composition and crustal lineaments on the Vøring Margin, NE Atlantic: a review. Tectonophysics 472 (1-4), 183–193.

Mjelde, R., Kodiara, S., Shimamura, H., Kanazawa, T., Shiobara, H., Berg, E. W., Riise, O., 1997. Crustal structure of the central part of the Vøring Basin, mid-Norway margin, from ocean bottom seismographs. Tectonophysics 277 (4), 235–257.

Mjelde, R., Shimamura, H., Kanazawa, T., Kodiara, S., Raum, T., Shiobara, H., 2003. Crustal lineaments, distribution of lower crustal intrusives and structural evolution of the Vøring Margin, NE Atlantic; new insight from wide-angle seismic models. Tectonophysics 369 (3-4), 199–218.

National Institute of Geophysics and Volcanology in Italy/Instituto Nazionale di Geofisica e Vulcanologia, 2019. Elements of the geomagnetic field. http://roma2.rm.ingv.it/en/research_areas/1/earth-s_magnetic_field/8/elements_of_the_geomagnetic_field, last accessed: 2019-05-13.

Norwegian Petroleum Directorate, 2019a. Well 6604/2-1, General Information. http://factpages.npd.no/ReportServer?/FactPages/PageView/wellbore_exploration&rs:Command=Render&rc:Toolbar=false&rc:Parameters=f&NpdId=6568&IpAddress=129.241.64.249&CultureCode=nb-no, last accessed: 2019-05-06.

Norwegian Petroleum Directorate, 2019b. Well 6704/12-1, General Information. http://factpages.npd.no/ReportServer?/FactPages/PageView/wellbore_exploration&rs:Command=Render&rc:Toolbar=false&rc:Parameters=f&NpdId=3759&IpAddress=84.215.249.15&CultureCode=en, last accessed: 2019-05-06.

Olesen, O., Ballling, N., Barrère, C., Breiner, N., Davidsen, B., Ebbing, J., Elvebakk, H., Gernigon, L., Koziel, J., Lutro, O., Midttømme, K., Nordgulen, , Olsen, L., Osmundsen, P. T., Pascal, C., Ramstad, R. K., Rønning, J. S., Skilbrei, J. R., Slagstad, T., Wissing, B., 2007. KONTIKI Final Report, CONTInental Crust and Heat Generation In 3D. NGU Report 2007.042.

Olesen, O., Brönner, M., Ebbing, J., Gellein, J., Gernigon, L., Koziel, J., Lauritsen, T., Myklebust, R., Pascal, C., Sand, M., Solheim, D., Usov, S., 2010a. New aeromagnetic and gravity compilations from Norway and adjacent areas: methods and applications. In: Petroleum Geology Conference Proceedings. Vol. 7. Geological Society of London, pp. 559–586.

Olesen, O., Ebbing, J., Gellein, J., Kihle, O., Myklebust, R., Sand, M., Skilbrei, J. R., Solheim, D., Usov, S., 2010b. Gravity anomaly map, norway and adjacent areas, scale 1:3 million. Norges geologiske undersøkelse, Trondheim.

Olesen, O., Gellein, J., Gernigon, L., Kihle, O., Koziel, J., Lauritsen, T., Mogaard, J. O., Myklebust, R., Skilbrei, J. R., Usov, S., 2010c. Magnetic Anomaly Map, Norway and Adjacent Areas, Scale 1:3 Million. Norges geologiske undersøkelse, Trondheim.

Olesen, O., Henkel, H., Kaada, K., Tveten, E., 1991. Petrophysical properties of a prograde amphibolite-granulite facies transition zone at Sigerfjord, Vesterålen, northern Norway. Tectonophysics 192 (1-2), 33–39.

Ottesen, D., Rise, L., Sletten Andersen, E., Bugge, T., Eidvin, T., 2009. Geological evolution of the Norwegian continental shelf between 61° N and 68° N during the last 3 million years. Norwegian Journal of Geology/Norsk Geologisk Forening 89 (4), 251–265.

Pascal, C., 2015. Heat flow of Norway and its continental shelf. Marine and Petroleum Geology 66, 956–969.

Rasmussen, A., Larsen, M., n.d. Completion Report. Well 6610/7-2. http://factpages.npd.no/pbl/wellbore_documents/26_01_Completion_Report_and%20Composite_log.pdf', last accessed: 2019-05-20.

Ritter, U., Zielinski, G. W., Weiss, H. M., Zielinski, R. L. B., Sættem, J., 2004. Heat flow in the Vøring Basin, mid-Norwegian shelf. Petroleum Geoscience 10 (4), 353–365.

Salazar, J. M., Vargas, C. A., Leon, H., 2017. Curie point depth in the SW Caribbean using the radially averaged spectra of magnetic anomalies. Tectonophysics 694, 400–413.

Schönharting, G., Abrahamsen, N., Eldholm, O., Thiede, J., Taylor, E., 1989. Paleomagnetism of the volcanic sequence in Hole 642E, ODP Leg 104, Vøring Plateau, and correlation with early Tertiary basalts in the North Atlantic. In: Proceedings of the Ocean Drilling Program, Scientific Results. Vol. 104. pp. 911–920.

Schön, J. H., 2015. Physical Properties of Rocks: Fundamentals and principles of petrophysics. Vol. 65. Elsevier.

Skilbrei, J. R., Skyseth, T., Olesen, O., 1991. Petrophysical data and opaque mineralogy of high-grade and retrogressed lithologies: Implications for the interpretation of aeromagnetic anomalies in norhern Vestranden, central Norway. Tectonophysics 192 (1-2), 21–31.

Skogseid, J., Pedersen, T., Larsen, V. B., 1992. Vøring Basin: subsidence and tectonic evolution. In: Structural and Tectonic Modelling and its Application to Petroleum Geology. Elsevier, pp. 55–82.

Slagstad, T., 2008. Radiogenic heat production of Archean to Permian geological provinces in Norway. Norwegian Journal of Geology/Norsk Geologisk Forening 88 (3), 149–166.

Slagstad, T., Barrére, C., Davidsen, B., Ramstad, R. K., 2008. Petrophysical and thermal properties of pre-Devonian basement rocks on the Norwegian continental margin. Norges geologiske undersøkelse Bulletin 448, 1–6.

Spector, A., Grant, F. S., 1970. Statistical models for interpreting aeromagnetic data. Geophysics 35 (2), 293–302.

Talwani, M., Heirtzler, J. R., 2010. Computation of magnetic anomalies caused by two-dimensional bodies of arbitrary shape. In: Parks, G. A. (Ed.), Computers in the mineral industries, Part 1. Vol. 1. Stanford Univ. Publ., pp. 559–586.

Talwani, M., Worzel, J. L., Landisman, M., 1959. Rapid gravity computations fro two-dimensional bodies with application to the Mendocino submarine fracture zone. Journal of Geophysical Research 64 (1), 49–59.

Turcotte, D., Schubert, G., 2002. Geodynamics. Vol. 2. Cambridge University Press.

Urpi, L., Rinaldi, A. P., Rutqvist, J., 2017. Fault reactivation induced by temperature and pressure changes in the life of a deep geological repository. In: 51st U.S. Rock Mechanics/Geomechanics Symposium. American Rock Mechanics Association.

Won, I. J., Bevis, M., 1987. Computing the gravitational and magnetic anomalies due to a polygon: Algorithms and Fortran subroutines. Geophysics 52 (2), 232–238.

Zastrozhnov, D., Gernigon, L., Gogin, I., Abdelmarak, M. M., Planke, S., Faleide, J. I., Eide, S., Myklebust, R., 2018. Cretaceous-Paleocene evolution and crustal structure of the northern Vøring Margin (offshore Mid-Norway): results from integrated geological and geophysical study. Tectonics 37 (2), 497–528.

Appendix A

Thermal Modelling Panels

This section presents the results of temperature and heat flow modelling performed for two additional wells: 6607/5-1 located at the Utgard High and 6609/6-1 located a the southern Grønøy High. The modelling is based on gamma ray, density, and sonic logs and done similar to Chernyshova (2018). Theoretical background for the modelling is shown in Chapter 2. Along with several other wells located at and close to the composite seismic section, the calculated temperature and heat flow profiles are used further to extend the thermal modelling to deeper levels.

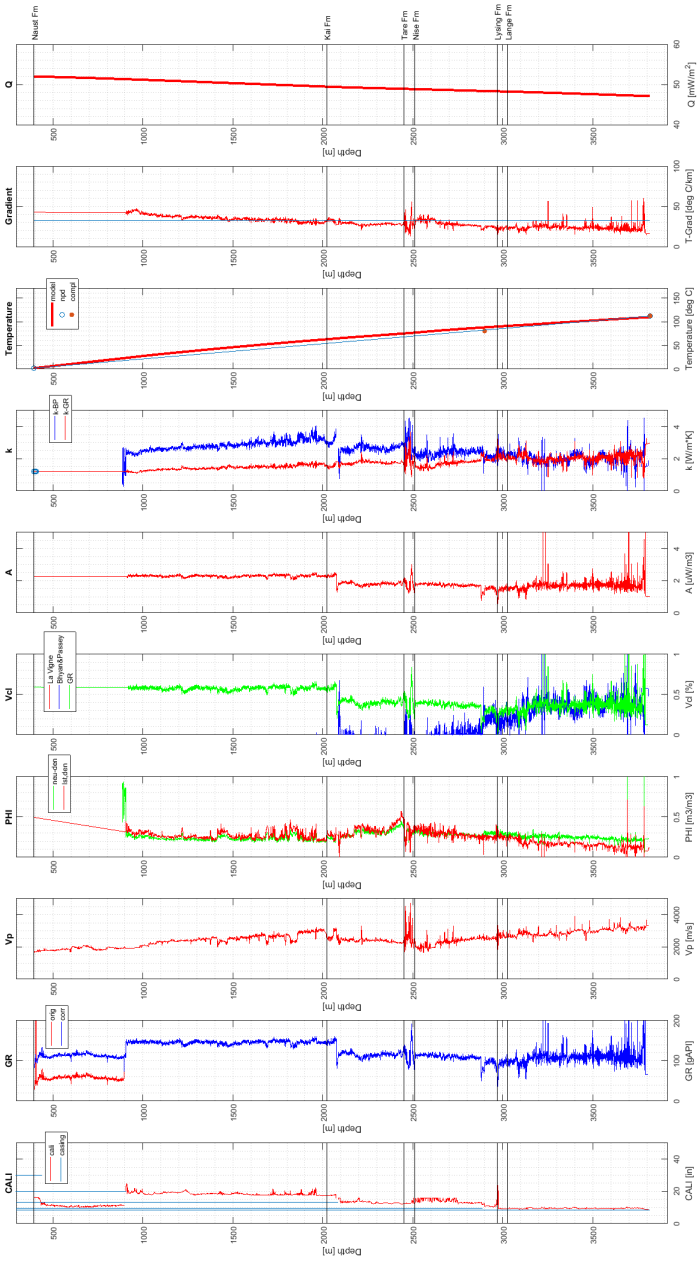

Figure A.1: Thermal modelling results for well 6607/5-1.

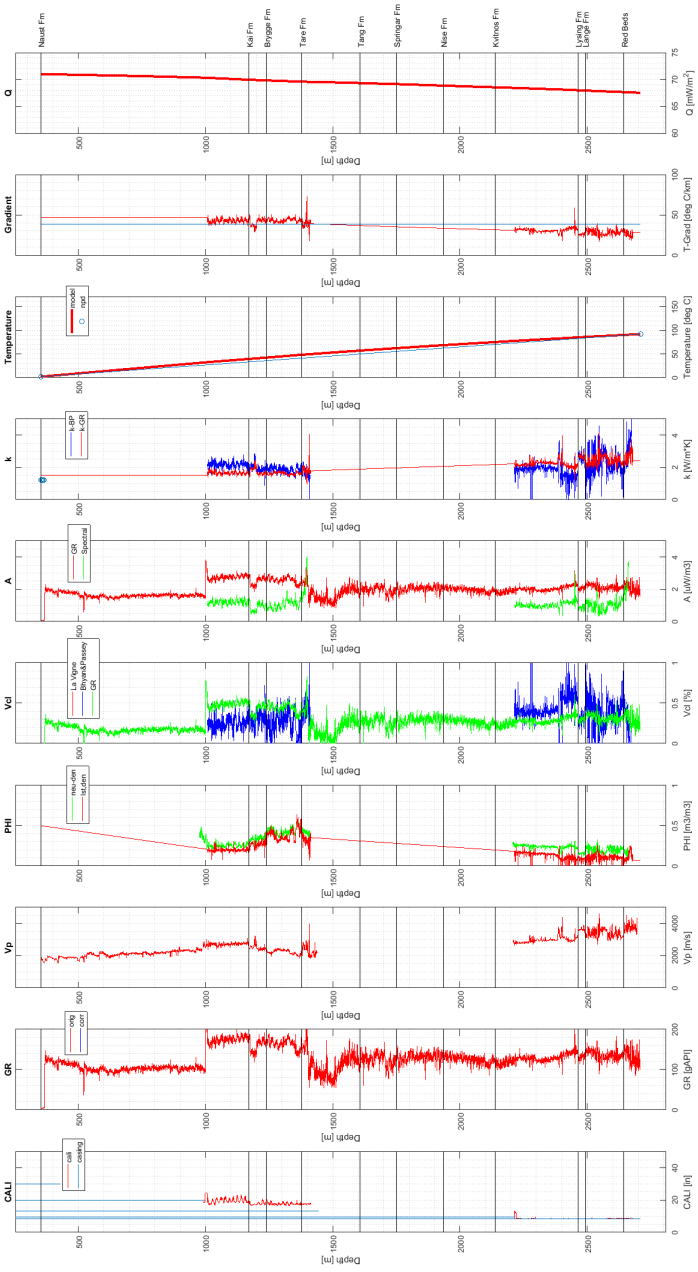

Figure A.2: Thermal modelling results for well 6609/6-1.

Appendix B

DDMS Estimation

This section shows the calculation of the DDMS form the average radial power spectrum. Figures B.1, B.2, B.3 correspond to Figures 4.15,4.16 and 4.17 in Chapter 4. The windows are oriented in W-E direction from the left to the right and stacked vertically. Upper plots within each window show the logarithm of the spectrum and manually fitted tangent line, while lower plots indicate the values calculated automatically by Geosoft.

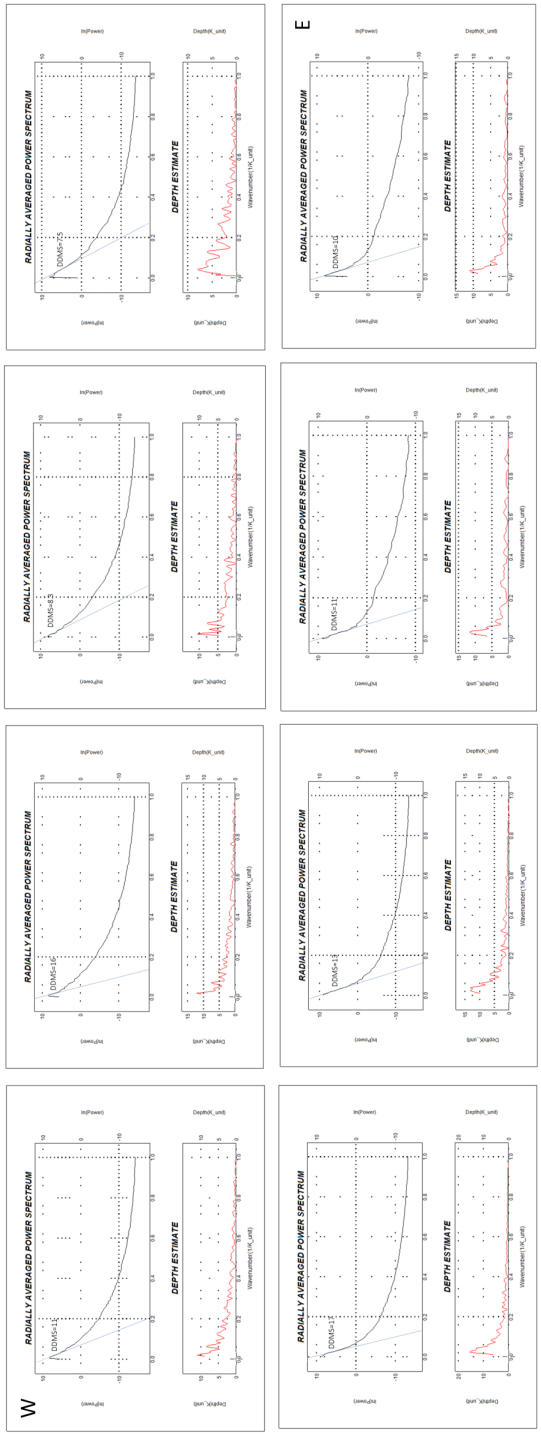

Figure B.1: DDMS estimation for 170 km window length. Plots correspond to windows shown on Figure 4.15 from W to E.

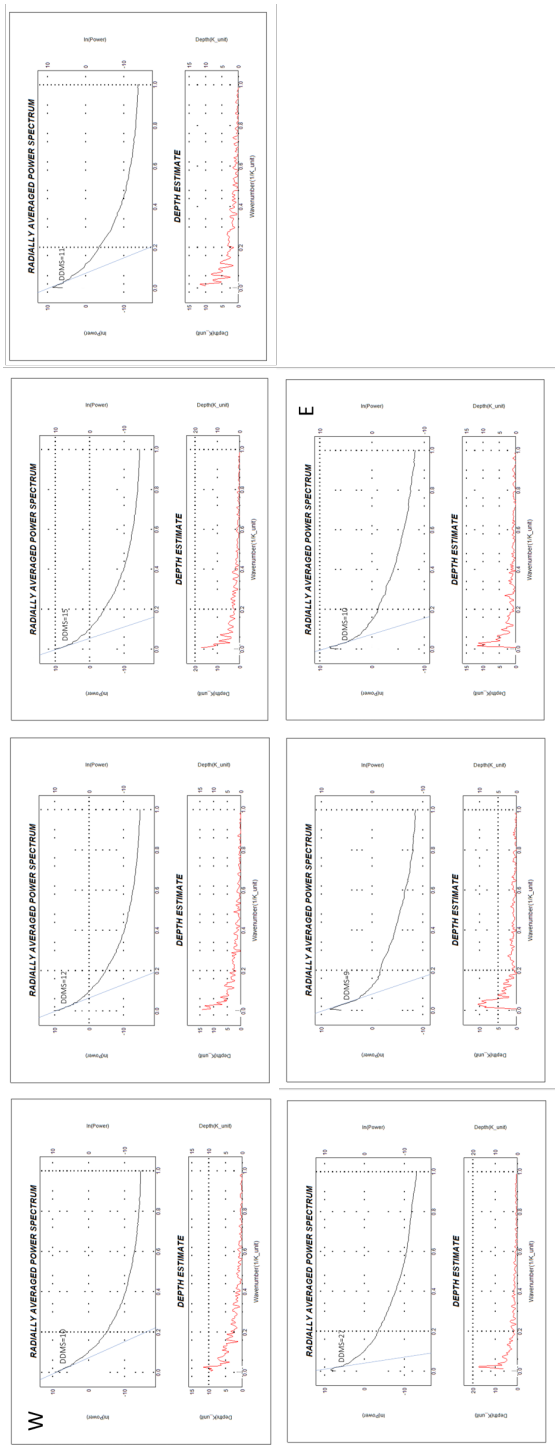

Figure B.2: DDMS estimation for 230 km window length. Plots correspond to windows shown on Figure 4.16 from W to E.

Figure B.3: DDMS estimation for 300 km window length. Plots correspond to windows shown on Figure 4.17 from W to E.

Appendix C

Expanded Magnetic Grid

This sections shows larger magnetic grid extracted from Olesen et al. (2010c) for DDMS calculations.

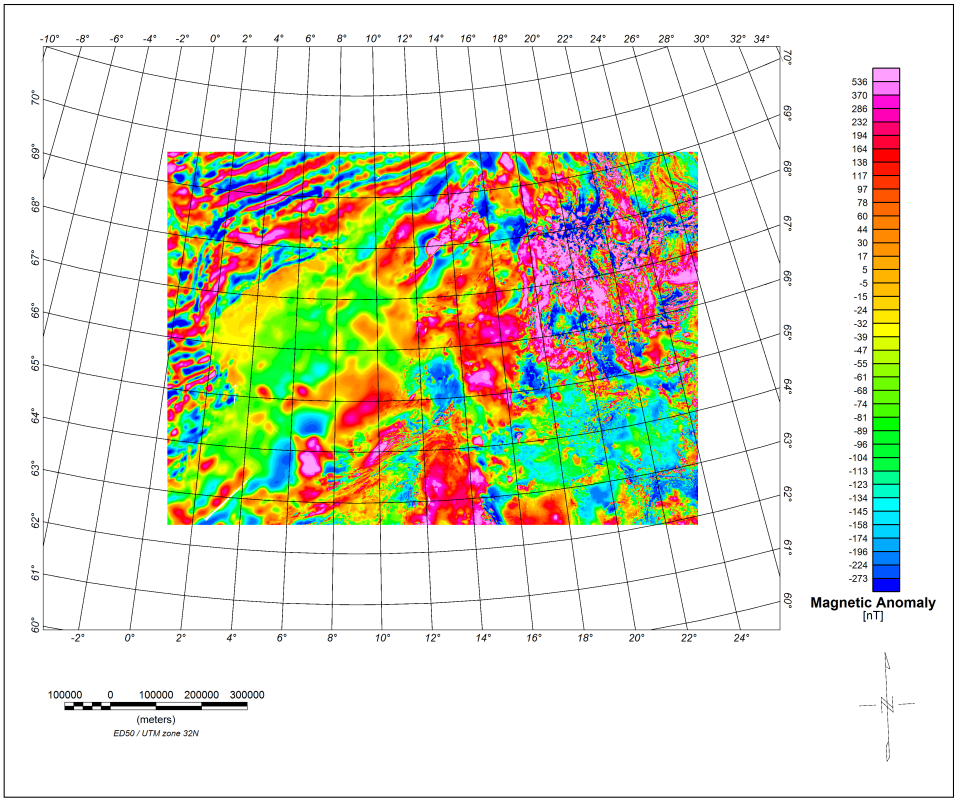

Figure C.1: Magnetic anomaly modified after Olesen et al. (2010c).

Appendix D

Specialization Project Report

The unpublished Specialization Project referred in the text as Chernyshova (2018) is attached in the following section.

Potential causes for varying temperature gradient in the Vøring Basin, Norwegian Sea

Alena Chernyshova

January 2019

SPECILIZATION PROJECT

Department of Geoscience and Petroleum
Norwegian University of Science and Technology

Supervisor 1: Kenneth Duffaut
Supervisor 2: Marco Brönner

Preface

This document is a Project Specialization work done during autumn semester of 2018, which represents a prephase for Master Thesis planned for spring 2019. The idea was brought to me by my supervisors, Kenneth Duffaut and Marco Brönner, who discovered the temperature anomaly at the Gjallar Ridge, Norwegian Sea, while working with other projects in this area. Project is written together with Norwegian University of Science and Technology, and the data was kindly provided by Diskos National Data Repository and Norwegian Petroleum Directorate.

Trondheim, 2018-1-1

Alena Chernyshova

Acknowledgment

I would like to thank my supervisors, Kenneth Duffaut and Marco Brönner, for sharing their ideas and knowledge as well as providing enormous amount of help and encouragement. I also would like to thank Dicky Harishidayat for helping with gathering of necessary data and many fruitful discussions. In addition, I would like to take this opportunity to thank Diskos National Data Repository and Norwegian Petroleum Directorate for providing both seismic and well data, and The Geological Survey of Norway for sharing with me their magnetic data, all of which were essential for this work.

Alena Chernyshova

Executive summary

The project attempts to find a reason for temperature anomalies across the Vøring Basin. Thermal modelling performed on the basis of well log data coupled with seismic data interpretation showed that variations in sediment thickness and net-to-gross ratio do not have a primary effect on temperature gradient. Furthermore, it was discovered that heat flow from basement or deepest sediments is the main contributor to high gradient at the Gjallar Ridge and North of the Trøndhelag Platform. Even when considering possible uncertainties related to modelling of thermal conductivity, elevated gradients at some parts of the basin can only be explained by high heat flow input. Consequently, conclusions and suggestions for further work are presented, which is planned to continue as a part of the Master Thesis during spring 2019.

Contents

Chapter 1

Introduction

1.1 Background

Problem formulation

The Vøring Margin experienced various tectonic events since the Caledonian Orogeny. Main processes shaping current geomorphology are three rifting episodes which can be traced back to Carboniferos - Permian, Middle Jurassic - Early Cretaceous and Late Cretaceous - Early Eocene accordingly (Brekke (2000)). While first two events are associated with continental rifting, the last one is correlated with continental break-up. As a result, the Vøring Basin presents a thick package of Cretaceous infill sediment with many extensional and compressional features as well as numerous intrusive bodies (Figure 1.1). Such extensive and complex tectonic history of the basin makes it hard to predict the thermal state. At the same time, understanding and predicting temperatures is crucial for petroleum industry. While working on potential prospects, it is important to estimate what temperature is expected at the reservoir zone, as well as anticipate past and current heat flows (HF). These factors govern the extent of maturity of source rock. Difference of few degrees over a long time window can alter hydrocarbon phase and change financial outcome. That is why, understanding thermal state of the area improves basin modelling processes and affects the accuracy of prospect evaluations.

To be able to predict temperature ranges at depths, gradients can be used. However, predicting temperature gradient (TG) is a challenging task as it can be related to a number of exogenic and endogenic factors, such as heat input or thermal properties of rocks. Therefore, it is common that temperature-depth relationships vary from one area to another. The Vøring Basin is a good example of such phenomenon. Well data shows that temperatures at the Gjallar Ridge increase much faster with depth than at the center of the basin (Figure 1.1). The value is also slightly elevated at the eastern margin of the basin, north of the Trøndelag Platform. Wells $6704/12-1$, $6604/2-1$ and $6605/1-1$ on the Gjallar Ridge have temperature gradi-

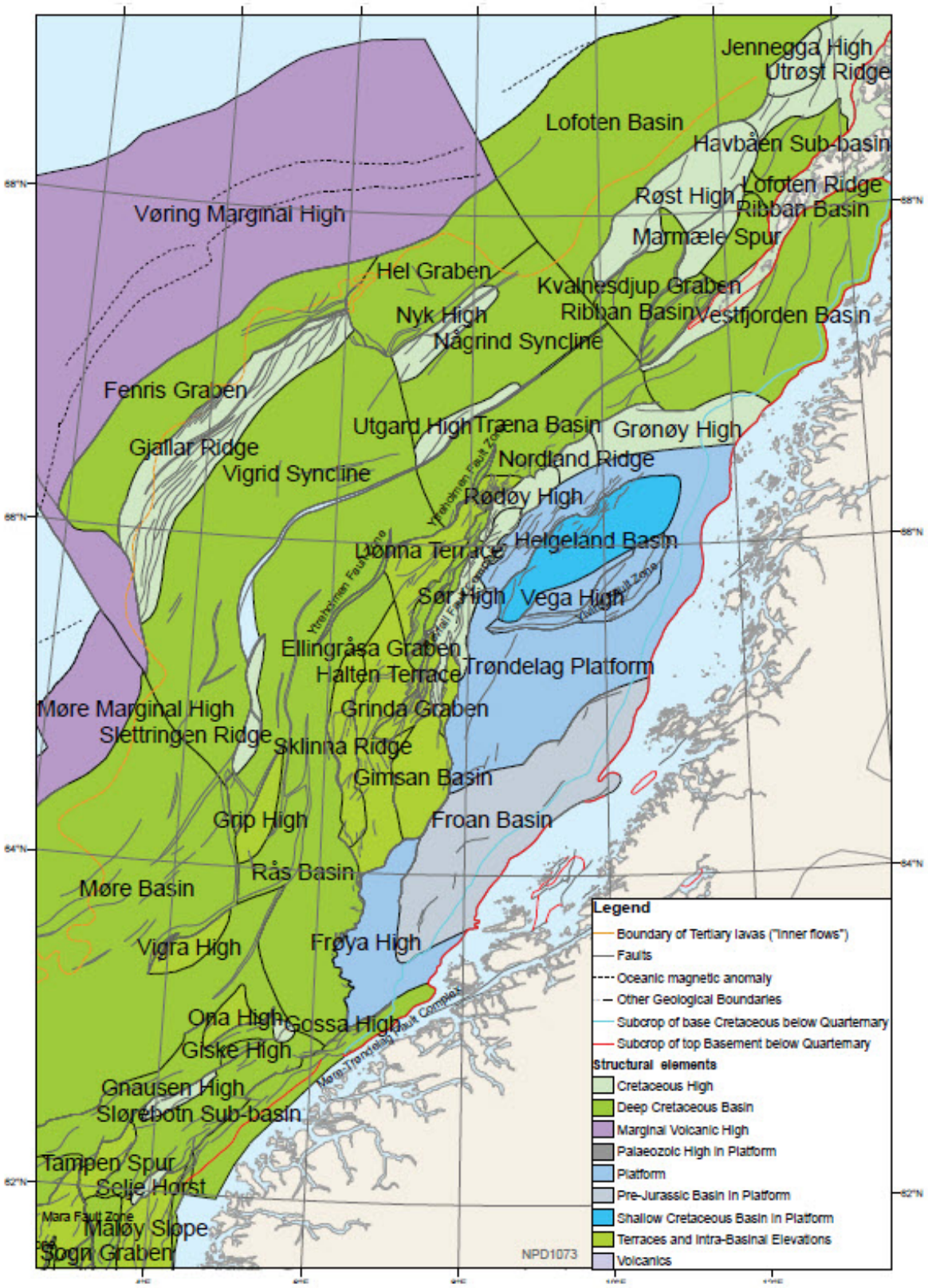

Figure 1.1: Structural elements, Norwegian Sea, from Halland et al. (2013)

ents around $50°C/km$ ($53°C/km$, $52°C/km$ and $48°C/km$ respectively), while wells $6707/10-1$, $6607/2-1$, $6607/5-2$ and $6609/5-1$ in the center of the basin have temperature gradients between $29°C/km$ and $37°C/km$ ($37°C/km$, $34°C/km$, $33°C/km$ and $29°C/km$ respectively). Wells $6610/2-1S$ and $6610/3-1R$ near the Grønøy High have gradients of $40-41°C/km$. In this way, the Vøring Basin becomes a good candidate for exploring temperature variations throughout the area and examining potential causes affecting the thermal state.

Based on the Steady State 1D Heat Flow Equiation (Section 1.4), main factors affecting gradient are heat flow input, thermal conductivity of rocks and radiogenic heat generation. In this work, an attempt will be made to assess the influence of these three factors on temperature gradient values, and conclusions will be made for what could be the main cause for elevated temperatures.

Related work

There are many articles discussing relationship between geological and thermal properties of rocks. Some of them are focusing specifically on the Vøring Basin. One extensive study is presented by Ritter et al. (2004). In the article, authors compile heat flow studies done previously together with heat flow calculated from rock conductivity and thermal gradient measurements performed at 159 sites in the basin. Authors do not present any apparent trend for heat flow values, but at some locations measurements vary drastically between neighbouring points. Potential causes for heat flow variations are also presented in their work. Among the most important ones are sediment rate, focusing of heat flow through topographic highs, decrease of heat flow generation from crust due to crustal thinning, and hydrothermal effects. Ritter states that rapid sedimentation leads to lower geothermal gradient and heat flow, which becomes evident at the Utgard High, where low heat flow values correspond to very thick Pliocene-Pleistocene sediment accumulation. He also admits that heat flow difference of about $20\%-30\%$ is expected from interiors of the basins towards adjacent highs, which can partially explain low heat flow in the Någrind Syncline . In addition to measuring heat flow, article models heat flow across one cross-section, which shows that heat flow is expected to decrease at the deepest part of the basin due to the fact that this is where crystalline basement is stretched to a higher extent. At those locations, thinner basement is compensated by sediments which have lower heat generating capacity. However, this does not seem to conform with practical results, except for the Någrind Syncline. One important conclusion is that large variability of heat flow can be caused by hot fluid migration through faults. However, this theory is hard to put into practical context as it requires some fluid properties and fault specifics to be known. At the same time, authors suggest that this phenomenon can stand behind high variation of heat flow at the Nyk High and the Hel Graben.

Another important work related to this topic is heat flow study performed by Christophe

Pascal (Pascal (2015)). This is a much larger study, which includes heat flow calculations based on drill stem test temperatures and measured rock conductivities for 63 wells across the whole Norwegian continental shelf. Unfortunately none of those wells are from the Vøring Basin, they mostly cover the Trøndelag Platform and adjacent terraces. However, author compiles his estimates with previously collected data and creates a regional heat flow map which shows low heat flow values at the center of the Vøring Basin and gradual increase towards the Trøndelag Platform. In this work, he also relates such variations to low crustal heat generation due to extreme thinning of basement at the centers of the basins. Sedimentation and erosion as potential influences on heat flow values are also discussed, however, the conclusion is that regional trends would remain the same even after correction.

Both Ritter et al. (2004) and Pascal (2015) complement their research with previous heat flow studies. Among those are works of Haenel (1974), Langseth and Zielinski (1974), Eldholm et al. (1987), Sundvor et al. (1989), who measured heat flow in this area. In addition to that, a study by Closs and Haenel (2003) also provides estimates which are relevant for this analysis. Those measurements are discussed in Section 2.2 in a context of this project's results.

Furthermore, there are articles which are tangentially related to this topic. For example, in the paper by Ebbing et al. (2009) authors model Curie depth isoterm based on magnetic data and attempt to compare it with thermal model. This model was based on geometry of the basin and supplied with thermal conductivity and radiogenic heat generation values. It is interesting to see, that in order to match the two models, basal heat flow values have to be increased by a factor of 2 from the Froan Basin towards the Gjallar Ridge. As a consequence, thermal gradient is also increased along the section. Despite the fact that authors discard this assumption based on uncertainty related to Curie depth modelling in the western part of the area, the trend is similar to the one predicted in the following project. Another comprehensive work by Maystrenko et al. (2018) investigates the relationship between Cenozoic erosion and deposition and thermal state within Lofoten-Vesterålen zone. The area of interest is located North-East of the Vøring Basin, but covers some parts of it. In this paper, it becomes evident that erosion and deposition can have substantial effect on temperatures as deep as 60 km, however, authors predict no siginificant eriosion at the North-Eastern part of the Vøring Basin.

What remains to be done?

It seems like there is a lot of interest around heat flow values in the area. Nevertheless, none of the studies discuss abnormal thermal state of the Gjallar Ridge in particular and elevated values north of the Trøndhelag Platform. This project will focus on this issue, attempting to establish whether there is a connection between sediment thickness and type and temperature gradient in the section from the Gjallar Ridge and towards North of the Grønøy High. The approach includes petrophysical analysis and sedimentary heat generation prediction performed for 9

wells, along with interpretation of 1 2D composite seismic line.

1.2 Objectives

The main objectives of this project are

1. Testing whether there is a connection between temperature gradient and thickness of sedimentary package
2. Testing whether there is a connection between temperature gradient and sediment type
3. Testing whether there are reasons for assuming varying heat flow input from basement to sediment column

1.3 Approach

First step of the project is Petrel based seismic interpretation of the line stretching from North of the Gjallar Ridge to North of the Trøndhelag Platform (Figure 1.2). This will help to estimate whether depth to basement can be correlated with temperature gradient. Next step involves studying local variations in sediment column and how these can be related to temperature gradient in the wells. This will be done by modelling temperature gradient based on well data, which will show to what extend temperature gradient is affected by radiogenic heat or formation thermal conductivity. This in turn will be coupled back to seismic section, if necessary, where individual sediment packages can be traced along the whole section. Last step includes extrapolation of thermal gradient and heat flow calculations to top basement, involving simplifications of thermal properties of deepest sedimentary rocks.

Seimsic interpretation is performed for 2D line created on the basis of several 2D seismic surveys ($NPD-VB-89\_PROC\_WESTERN$, $SL99$, $TBS2000$, $N1N3C-94$, $N5-94$) and coupled with 9 wells: $6704/12-1$, $6604/2-1$, $6605/1-1$, $6707/10-1$, $6607/2-1$, $6607/5-2$, $6609/5-1$, $6610/2-1S$ and $6610/3-1R$. Interpretation is done for tops of the main packages in the area: Top Neogene and Quaternary, Top Paleogene, Top Paleocene, Base Tertiary Unconformity and Base Createous. Corresponding lithostratigraphic units are shown on Figure 1.3. As understanding the sedimentary column thickness is crucial, Top Crystalline Basement is also mapped where possible.

Thermal modelling is based on well logs and involves calculations of thermal conductivity and radiogenic heat generation for sedimentary column, as well as computations of thermal gradient and heat flow. Since well logs are not always available across the whole interval from

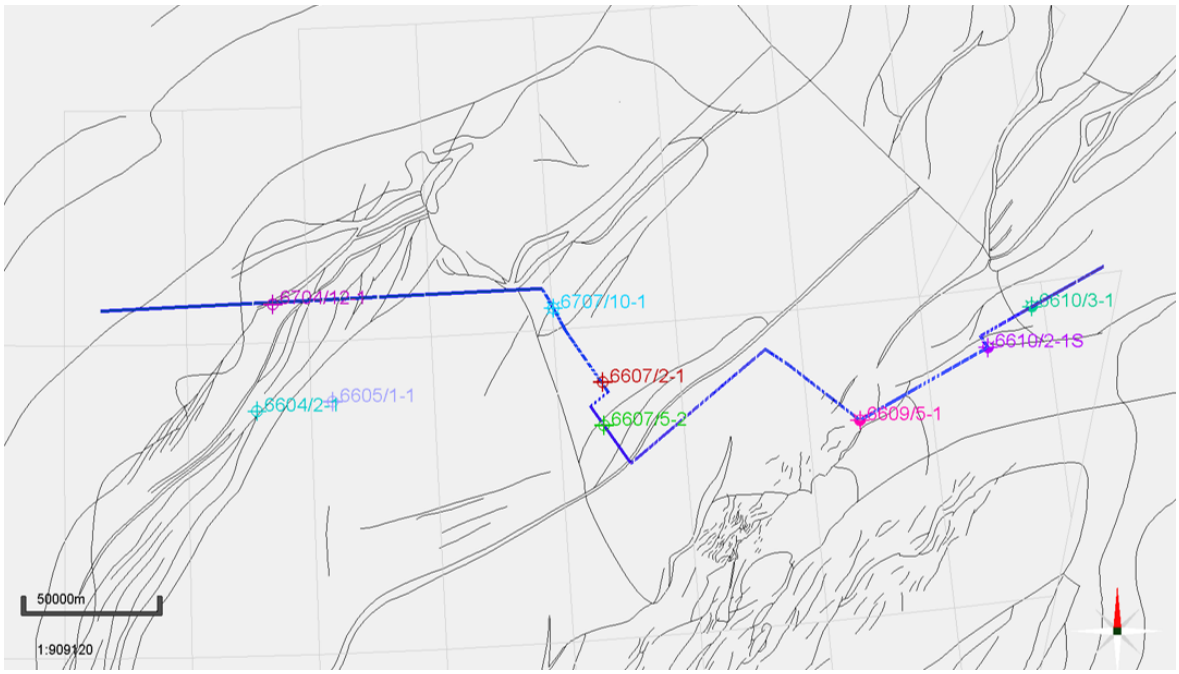

Figure 1.2: Composite seismic line and wells

seabed to total depth, many interpolations and extrapolations are required. Generally, log quality check was done before thermal modelling, as this process is very sensitive to unrealistic values, especially thermal conductivity variations.

It is important to mention that thermal modelling requires surface heat flow and temperatures as inputs. Even though, from previous studies average regional heat flow is concluded to be around $60 mW/m2$ (Ritter et al. (2004)), it seemed appropriate to calibrate heat flow values relative to temperatures in the wells in order to fit the trends.

1.4 Theoretical background: equations

Thermal gradients and temperatures are modelled in accordance with 1D heat conductive equation. The following section presents the formulas which were used to calculate all necessary variables and inputs.

1D heat conductive equation

The starting point is 1D heat flow equation for heat flowing through a body with surface area s and height Δz, assuming that heat goes from z at the top to $z + \Delta z$ at the bottom.

The equation originates from Fourier's Law (1D):

$$Q(z) = -k\frac{\partial T}{\partial z}, \tag{1.1}$$

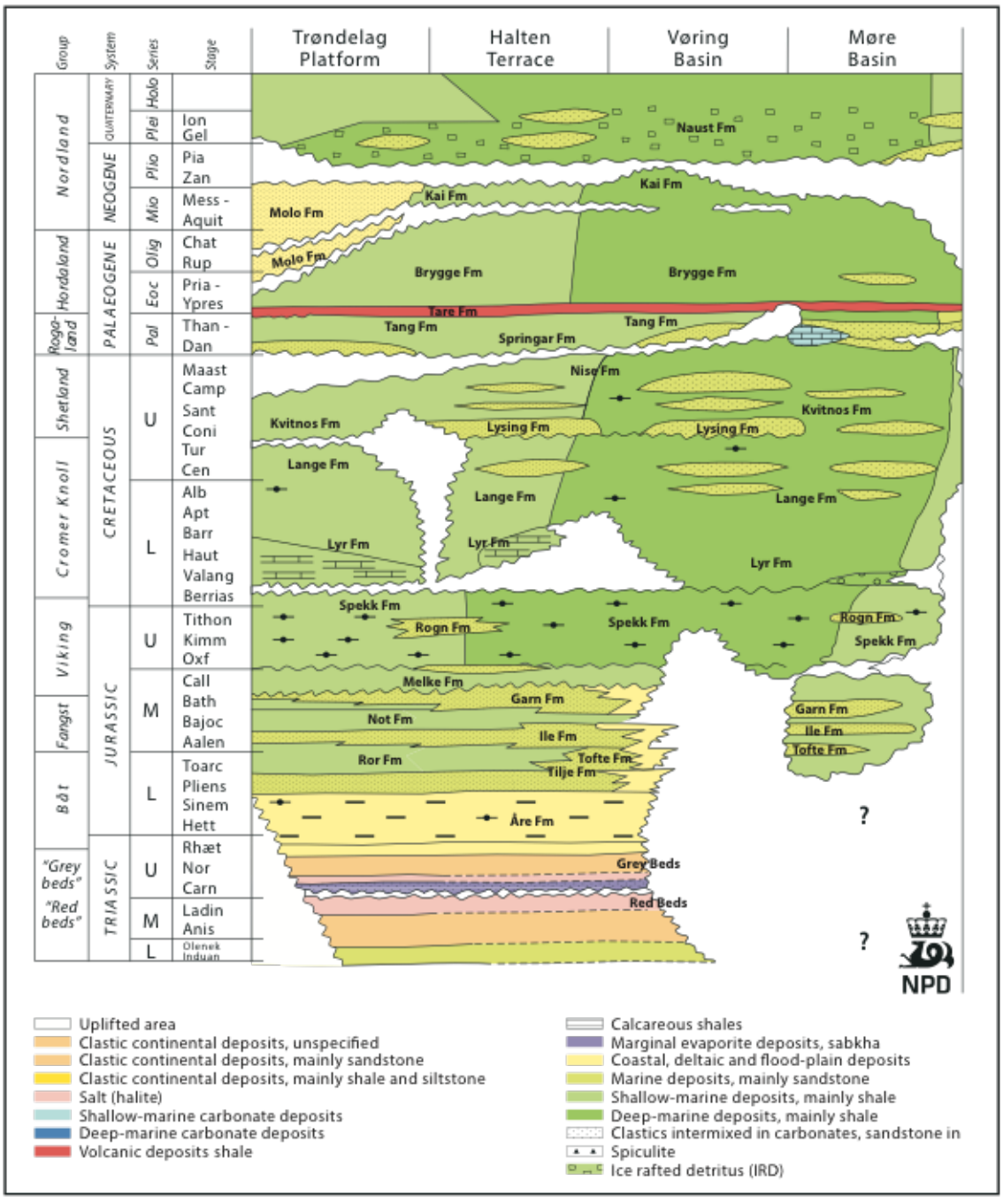

Figure 1.3: Lithostratigraphic chart, Norwegian Sea, from Halland et al. (2013)

where k is thermal conductivity, Q is heat flow and T is temperature.

Heat energy of this body is described by

$$Q(z,t) = c_p m T(z,t) = c_p \rho s \Delta z T(z,t), \tag{1.2}$$

where c_p is specific heat capacity and ρ is density.

According to energy conservation law, energy change in time should be equal to difference between heat energy in and heat energy out, plus radiogenic heat energy generated within the body:

$$\Delta Q_{time} = Q_{in} - Q_{out} + Q_{rad}. \tag{1.3}$$

Inserting Equation 1.1 and Equation 1.2 into Equation 1.3 gives

$$c_p \rho s \Delta z T(z,t+\Delta t) - c_p \rho s \Delta z T(z,t) = \Delta t s Q(z) - \Delta t s Q(z+\Delta z) + \Delta t s \Delta z A,$$

$$c_p \rho s \Delta z T(z,t+\Delta t) - c_p \rho s \Delta z T(z,t) = \Delta t S(-k\frac{\partial T}{\partial z})_z - \Delta t S(-k\frac{\partial T}{\partial z})_{z+\Delta z} + \Delta t s \Delta z A,$$

and dividing by $\Delta t \Delta z s$ results in

$$c_p \rho (\frac{T(z,t+\Delta t) - T(z,t)}{\Delta t}) = k(\frac{(\frac{\partial T}{\partial z})_{z+\Delta z} - (\frac{\partial T}{\partial z})_z}{\Delta z}) + A, \tag{1.4}$$

where A represents radiogenic heat generation.

In this way, assuming $\Delta t, \Delta x \to 0$, Equation 1.4 becomes

$$c_p \rho \frac{\partial T}{\partial t} = k\frac{\partial^2 T}{\partial z^2} + A, \tag{1.5}$$

while for steady state it takes form of

$$\frac{\partial^2 T}{\partial z^2} = -\frac{A}{k}, \tag{1.6}$$

where boundary conditions at the surface are

1. $T(z=0) = T_0$,
2. $Q(z=0) = -k\frac{\partial T}{\partial z} = -Q_0$.

Solving Equation 1.6 results in the following formulas for T and $\frac{\partial T}{\partial z}$:

$$\frac{\partial T}{\partial z} = -\frac{A}{k}z + \frac{Q_0}{k}, \tag{1.7}$$

$$T = T_0 - \frac{A}{2k}z^2 + \frac{Q_0}{k}z. \tag{1.8}$$

Finally, given surface heat flow, heat profile can be modelled by

$$Q = Q_0 - Az. \tag{1.9}$$

Thermal conductivity

Thermal conductivity is principal variable in the equations used for temperature modelling. Therefore, it is important to present how this value is obtained.

In the paper by Duffaut et al. (2018)), authors present empirical relationship between thermal conductivity, clay volume and pressure wave velocity as following

$$k = a_0(1 - V_{cl}(1 - \phi))V_P, \tag{1.10}$$

where a_0 is scaling factor typically chosen to be 1, V_{cl} is clay volume relative to bulk volume, ϕ is porosity and V_P is P-wave velocity.

At the same time, porosity can be calculated by the well-known formula (AAPG):

$$\phi = \frac{\rho_{ma} - \rho_{reading}}{\rho_{ma} - \rho_{fluid}}, \tag{1.11}$$

where ρ_{ma} is matrix density, which is chosen to be 2.7 $\frac{kg}{m^3}$ here, $\rho_{reading}$ is density log response and ρ_{fluid} is fluid density which is set to be 1 $\frac{kg}{m^3}$. To check this result, ϕ is also calculated from density and neutron logs with the following formula (Asquith and Gibson (1982))

$$\phi = \sqrt{\frac{\phi_N^2 + \phi_D^2}{2}}, \tag{1.12}$$

where ϕ_N is neutron porosity from neutron log and ϕ_D is density porosity calculated with Equation 1.11.

In order to compute clay volume the common formula was applied:

$$V_{sh} = \frac{GR_{reading} - GR_{min}}{GR_{max} - GR_{min}}, \tag{1.13}$$

where $GR_{reading}$ is gamma ray log response, while GR_{min} and GR_{max} are sand and shale gamma ray readings in the sediment column. This relationship is usually used to calculate V_{sh}, so the value is multiplied by a factor of 0.6, as most of the shales are around 60% clay on average (Bhuyan and Passey (1994)).[1]

Gamma ray values used for Equation 1.13 are corrected for mud weight and borehole size

[1] It is important to note that Equation 1.13 results in V_{cl} relative to matrix volume and not bulk volume.

with the formula given in Crain's Petrophysical Handbook (Crain (2015)):

$$GR_{corr} = GR_{reading}(1 + 0.000322 * (MWT - 1000)) * (1.0 + 0.0024 * (CAL - 203)), \tag{1.14}$$

where MWT is mud weight given in $[\frac{kg}{m^3}]$ and CAL is caliper log in $[mm]$.[2]

For comparison V_{cl} is also calculated from neutron and density logs as described by La Vigne et al. (2018) and Bhuyan and Passey (1994). However, in many cases those seem to correspond well with V_{cl} from GR. Since neutron and density coverage is limited, it was decided to proceed with V_{cl} from GR in the calculations.

Equation given in La Vigne et al. (2018) is as follows

$$V_{cl} = \frac{\phi_{neu} - \phi_{den}}{\phi_{neu,dryClay}}, \tag{1.15}$$

where ϕ_{neu} is neutron log reading, ϕ_{den} is density porosity calculated by Equation 1.11 and $\phi_{neu,dryClay}$ is neutron log reading in dry clay, chosen to be 0.4.

While equation in Bhuyan and Passey (1994) is

$$V_{cl} = \frac{\phi_{neu} - \phi_{den}}{\phi_{neu,sh} - \phi_{den,sh}} 0.6, \tag{1.16}$$

where $\phi_{neu,sh}$ is neutron log reading in shale zone and $\phi_{den,sh}$ is density porosity in shale zone.

Radiogenic heat generation

Radiogenic heat generated in a rock also plays an important role when it comes to temperature modelling. This value was calculated based on the following formula introduced by Bücker and Rybach (1996)

$$A = 0.0158(GR - 0.8). \tag{1.17}$$

Alternative formula is also given by Bücker and Rybach (1996) and is based on spectral GR:

$$A = \rho_{ma}(9.52C_U + 2.56C_{Th} + 3.48C_K)10^{-5}, \tag{1.18}$$

where C_U is concentration of Uranium given in [ppm],C_{Th} is Thorium concentration in [ppm] and C_K is Potassium concentration in weight percent.

[2]Final GR log released by the oil companies is sometimes already corrected for borehole size and mud weight, however, correction does not change GR considerably, so it is safe to apply the adjustment where it is hard to trace the origin of GR log. In addition, where GR is overcorrected, Vcl is estimated relative to new minimum and maximum bounds which gives a similar result.

1.5 Limitations

Main shortcoming of this project is a limited amount of data available for public use in the petroleum industry. Moreover, the Vøring Basin is rather unexplored area when compared to, for example, the Trøndelag Platform. In order to cover the section from the Gjallar Ridge to North of the Trøndelag Platform, a composite 2D line had to be constructed on the basis of several 2D surveys, which have varying coverage depths, polarity and data quality. Wells had to be chosen based on location relative to the line and not on quality or variability of logs. Some of the wells had questionable log responses in certain intervals, while many did not penetrate sequences below Cretaceous level. Consequently, many approximations and presuppositions had to be made which can affect the certainty of the results.

Quality of seismic interpretation was also affected by quality of seismic data. Sequences located below Cretaceous package appear to be very noisy, which made it challenging to track stratigraphic tops. That is why, Base Cretaceous is the deepest reflector interpreted above the basement. At many locations, such as the Vigrid Syncline, basement appears to be below seismic penetration depth and its position could only be assumed.

Another important limitation is the unreliable temperature data for certain wells. Since results are very dependent on surface heat flow, which is in turn calibrated to fit well temperatures, those temperatures become the key data. Generally, it is common to use drill stem test (DST) temperatures as valid measurements, however, none of the wells used in this project had available DST data. For some wells, temperatures were taken from Norwegian Petroleum Directorate (NPD) homepage and could not be traced back to its original source due to lack of public reports. Other wells had corrected temperatures present in completion reports (CR), which were different from those stated on NPD. In those cases, CR data was preferred. As a result, this temperature data introduces addition uncertainty related to the results of this study.

It is worth mentioning that this project is only a prephase to the Master Project, so the available time is rather limited. There is a lot of work which remains to be done in order to verify the results of this project as well as understand the problem from other angles.

Chapter 2

Results and discussion

2.1 Results

Formulas presented in Section 1.5 are used for thermal modelling in Matlab. Temperature is calculated by Equation 1.8, temperature gradient by Equation 1.7 and heat flow by Equation 1.9.

General workflow for all wells is:

1. Gamma ray log correction for mud weight and borehole size (Equation 1.14) and GR shift of anomalous trends
2. Clay volume calculation based on GR (Equation 1.13) and combination of neutron and density logs (Equation 1.15, Equation 1.16)
3. Radiogenic heat generation calculated in accordance with Bücker and Rybach (1996) (Equation 1.17)[1]
4. Thermal conductivity calculation as presented in Equation 1.10 with V_{cl} based on GR and Bhuyan and Passey (1994) for comparison
5. Density porosity calculation (Equation 1.11), examined in contrast with density-neutron porosity (Equation 1.12)
6. Temperature modelling in accordance with Equation 1.8
7. Temperature gradient modelling as suggested by Equation 1.7
8. Heat calculation based on Equation 1.9

[1] Spectral gamma ray is only available for well 6704/12 – 1, so for this well radiogenic heat generation is also calculated based on Equation 1.18.

As stated previously, surface heat flow is an important input variable for thermal modelling. The value varies between wells, as it was corrected in order to fit measured well temperatures.

Following subsections present the results of thermal modelling for each individual well. All depths used in the project are given in meters below rotary table (mRKB), as this is the most common depth measurement used in the industry.

2.1.1 Well panels

6704/12-1

The result is presented on Figure 2.1. **CALI** panel is used for caliper log and casing diameter in inches. **GR** panel is employed for original gamma ray log and corrected GR in $[gAPI]$. **Vp** panel is applied for pressure wave velocity in $[\frac{m}{s}]$ inferred from sonic log. **PHI** panel is used for porosity as a fraction of bulk volume derived from density log and density-neutron combination. **Vcl** panel illustrates matrix clay volume calculated by three different methods. **A** panel shows radiogenic heat generation in $[\frac{\mu W}{m^3}]$ from both spectral and corrected conventional GR. **k** panel showcases thermal conductivity in $[\frac{W}{mK}]$ calculated based on two different V_{cl} logs (from Bhuyan and Passey (1994) and from GR). **Temperature** panel depicts temperature log in $[^{\circ}C]$ modelled in Matlab, as well as bottom hole temperature which is given at NPD homepage. **Gradient** panel shows modelled temperature gradient in $[\frac{^{\circ}C}{km}]$ and average temperature gradient represented by a straight line. Finally, **Q** panel is used for modelled heat flow in $[\frac{mW}{m^2}]$. Note that circles at **k** panel represent shallow measurements of rock thermal conductivity performed by Ritter et al. (2004) in the Vøring Basin.

It is easy to notice the large separation of original GR log and corrected GR above 2400 m. A sudden drop at this depth does not seem to be related to variation in lithology, more likely a shift in applied correction or change of a logging tool. That is why, for some of the wells, including well $6704/12-1$, a constant shift for GR log was applied on shallow intervals.

Another important observation is the fact that all three methods for calculating V_{cl} give roughly the same k log. Therefore, it is convenient to use k derived from V_{cl} based on GR as it usually has a better depth coverage compared to neutron and density logs. In addition to that, limestone porosity can give slight underestimation when compared to neutron-density method, especially for shaly intervals. However, the difference is insignificant for modelling purposes.

Generally, it becomes evident that due to high GR the well is dominated by mudstones with the exception of Springar Formation and lower Nise Formation. In the article by Peltonen et al. (2008), which investigates mineralogy for some of the wells in the Vøring Basin, clay volumes for well $6704/12-1$ are around 0.5, based on X-Ray Diffracion method. Authors predict an average of 49.1% clays of total matrix volume for Hordaland Group, 43.5% for Rogaland Group and 54.0% for Shetland Group. Average clay volumes estimated in this project are approximately 50% for

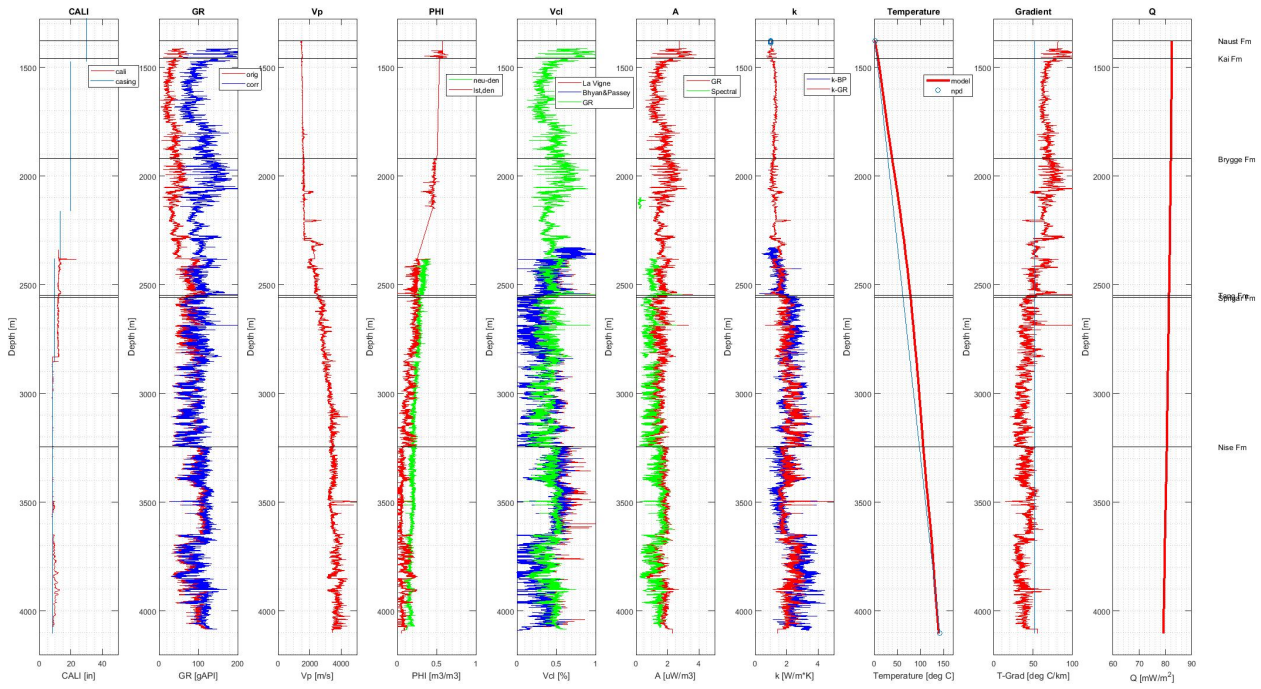

Figure 2.1: Temperature modelling for well 6704/12 – 1

Hordaland Group, 45% for Rogaland Group and 50% for Shetland Group, which are relatively close to the ones presented in the article. In addition to that, thermal conductivity measurements for shallow sediments from Ritter et al. (2004) closely correspond with modelled thermal conductivity values.

As expected, thermal conductivity is high for sandy intervals and low for shaly intervals. For sediments above Base Tertiary Unconformity (BTU) k is very low, around 1.5 $\frac{W}{mK}$ on average, which results in very high thermal gradient of 60 $\frac{^\circ C}{km}$ (Figure 2.1). On the contrary, Springar Formation seems to have a much higher N/G and a thermal conductivity of about 2.5 $\frac{W}{mK}$, resulting in thermal gradient of 40 $\frac{^\circ C}{km}$. Nise Formation can be interpreted as more homogeneous than Springar Formation, and to have both interchanging sand/shale thin layers and a thicker shale interval. This gives low conductivity and high gradient above 3650 m and the opposite - below.

Resulting heat flow becomes 82.5 $\frac{mW}{m^2}$.

6604/2-1

Same procedure was followed for well 6604/2 – 1. The result is shown on Figure 2.2. What strikes the eye here is highly variable V_{cl} logs caused by irregular neutron log. However, by looking at thermal conductivity it becomes evident that k logs are rather similar and V_{cl} from GR can be used.

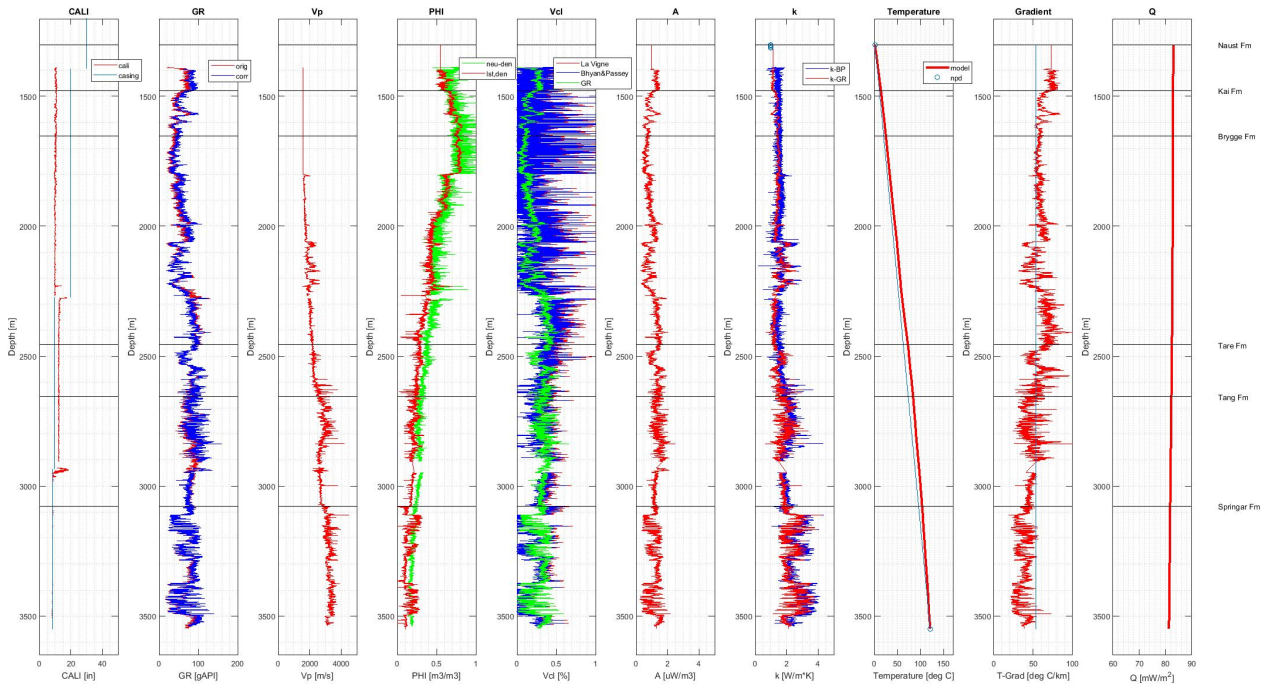

Figure 2.2: Temperature modelling for well 6604/2 – 1

Three sand units can be interpreted within the Springar Formation. These have very high conductivity of about 3 $\frac{W}{mK}$ and a thermal gradient of 30 $\frac{^{\circ}C}{km}$. Conductivity values are also high for some intervals within Tare Formation and Tang Formation, however, the average gradient there is about 50 $\frac{^{\circ}C}{km}$ due to low N/G. Brygge Formation contains some siliceous ooze sections (NPD (a)), which elevate thermal conductivity values and degrade thermal gradient, but the general trend for Hordaland Group is represented by low thermal conductivity and high temperature gradient.

Modelled surface heat flow is 83 $\frac{mW}{m^2}$ which is quite similar to the result from well 6704/12–1.

6605/1-1

Figure 2.3 presents the results of thermal modelling for well 6605/1–1. There is a noticeable difference in GR logs. It can be questioned, whether the method used to correct GR gives reliable estimates. However, resulting A does not seem to be anomalous, with 2 $\frac{\mu W}{m^3}$ for shale, which seem to be corresponding to values given in Hantschel and Kayerauf (2009). On the contrary, thermal conductivity at the surface seems to be higher than the one measured by Ritter et al. (2004). The reason for that could be the fact that modelling just below the seabed is very uncertain as most of the logs have been interpolated above 1270 m. Nevertheless, it is believed that this does not affect the modelling significantly.

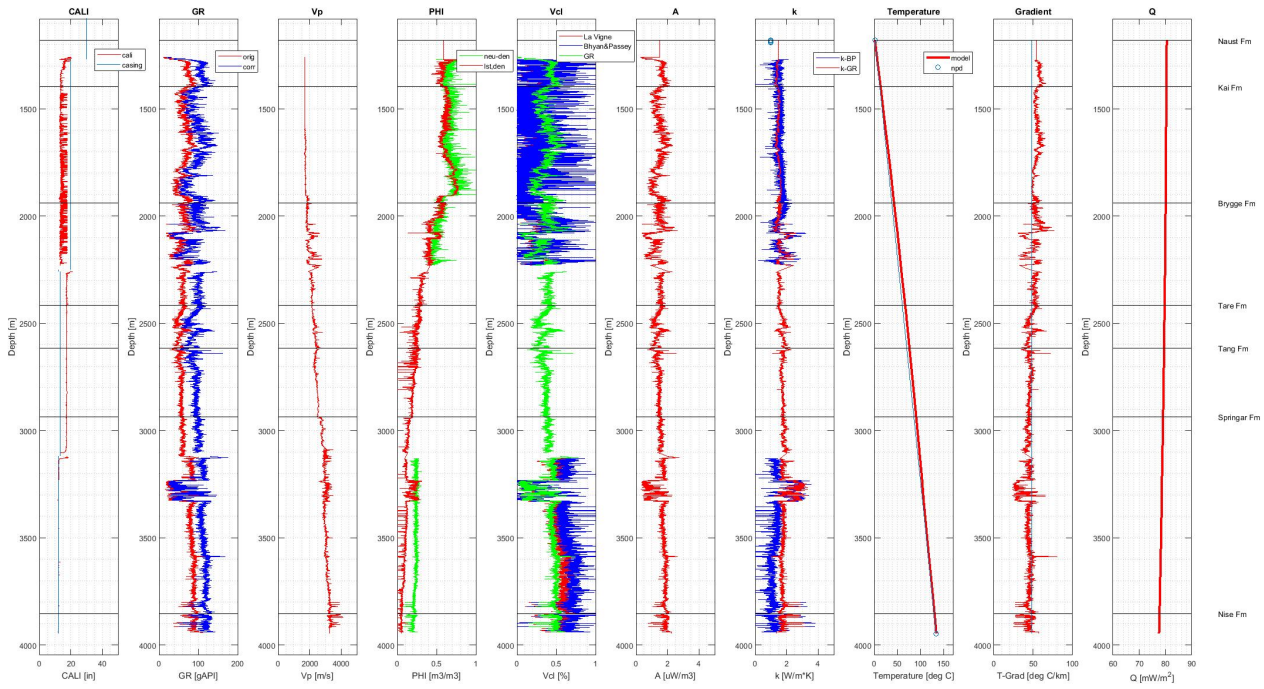

Figure 2.3: Temperature modelling for well 6605/1 – 1

Thermal gradient is relatively constant, around 50 $\frac{^{\circ}C}{km}$, although it is slightly higher above BTU. Two sand intervals are interpreted within Springar Formation with thermal conductivity of 3 $\frac{W}{mK}$ and temperature gradient of 30 $\frac{^{\circ}C}{km}$, similar to the well 6604/2 – 1. The rest of the well contains mudstones, possibly with few thin sand or ooze layers within Brygge Formation. Thermal conductivity of those mudstones is increasing from 1.5 $\frac{W}{mK}$ at the seabed to 2 $\frac{W}{mK}$ at TD.

This results in a surface heat flow of 80.5 $\frac{mW}{m^2}$.

6707/10-1

From Figure 2.4 it can be seen that there is a very high separation between GR logs, but again, corrected GR gives A values which correspond with Hantschel and Kayerauf (2009). It also becomes evident that modelled k is very different from the values measured by Ritter et al. (2004). As previously, the shallowest estimates can be discarded.

It is important to note, that this well has available data on corrected wellbore temperatures from completion report (Rydningen and Cade), which are plotted on the **Temperature** panel. These estimates are very different from bottom hole temperature given by NPD (b). It was decided to trust CR numbers, as it is hard to trace back where NPD values come from.

This well has higher sand content in comparison to the wells on the Gjallar Ridge. Tang Formation, Nise Formation and Lysing Formation can all be interpreted as sands, while the re-

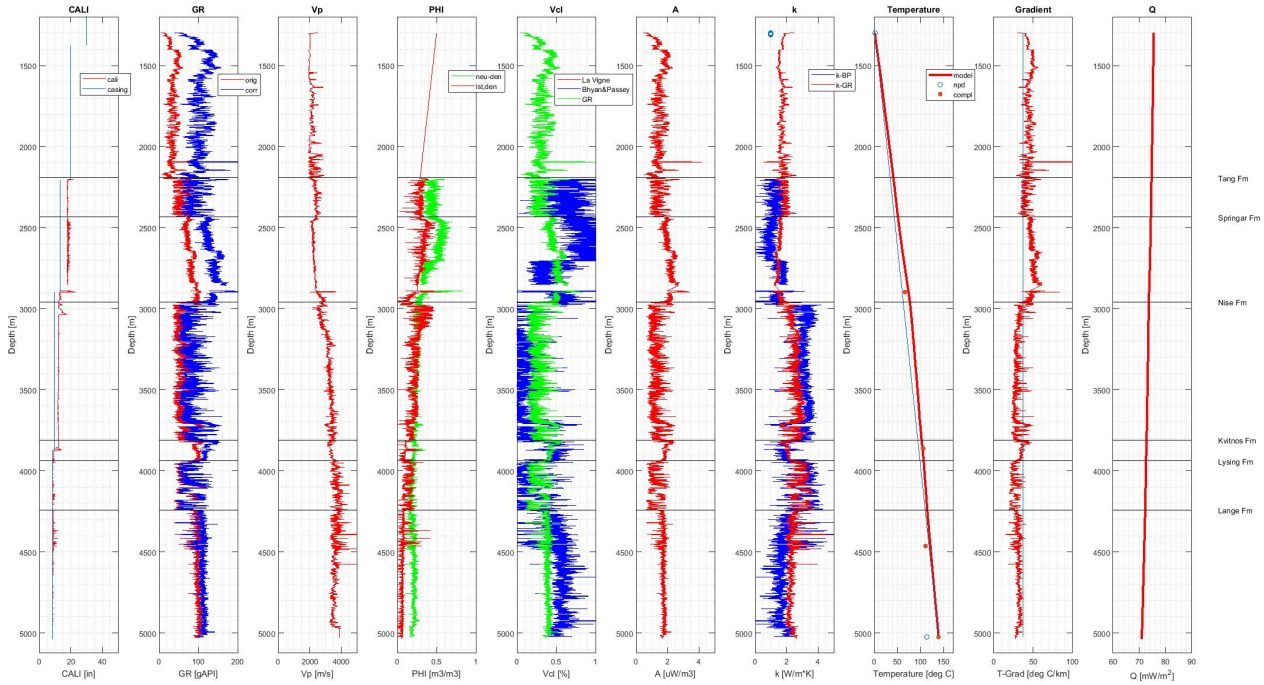

Figure 2.4: Temperature modelling for well 6707/10 – 1

maining part is likely to be shale. Sands in Tang Formation have k of 2 $\frac{W}{mK}$ and TG of 45 $\frac{^\circ C}{km}$, while both Nise Formation and Lysing Formation show k of 3 $\frac{W}{mK}$ and extremely low TG of 25 $\frac{^\circ C}{km}$. Shaly intervals have k between 1.5 and 2 $\frac{W}{mK}$, and TG in a range of 30 to 40 $\frac{^\circ C}{km}$.

Resulting heat flow is 75.5 $\frac{mW}{m^2}$, which is noticeably lower than heat flow on the Gjallar Ridge.

6607/2-1

Well panel is given on Figure 2.5. Separation between corrected GR and original GR is positive below 1950 m and negative above. It is hard to deduce whether correction gives optimal values, as this would imply gradual increase in sand content towards the seabed, which is not likely in this setting. However, correction was performed for all wells in this project, and consistency in calculations needs to be maintained. On the contrary, thermal conductivity of rocks under the seabed is not very different from the values measured by Ritter et al. (2004), however, a small difference is still present.

The well column mostly consists of shales, with thin sand interval under BTU. TG and k are rather constant, with an average of 35 $\frac{^\circ C}{km}$ and 2 $\frac{W}{mK}$ accordingly. While conductivity values are in agreement with typical shale conductivities from Hantschel and Kayerauf (2009), temperature gradient is much lower than expected. At the same time, TG is also affected by HF, and the resulting surface heat flow for this well is 68 $\frac{mW}{m^2}$.

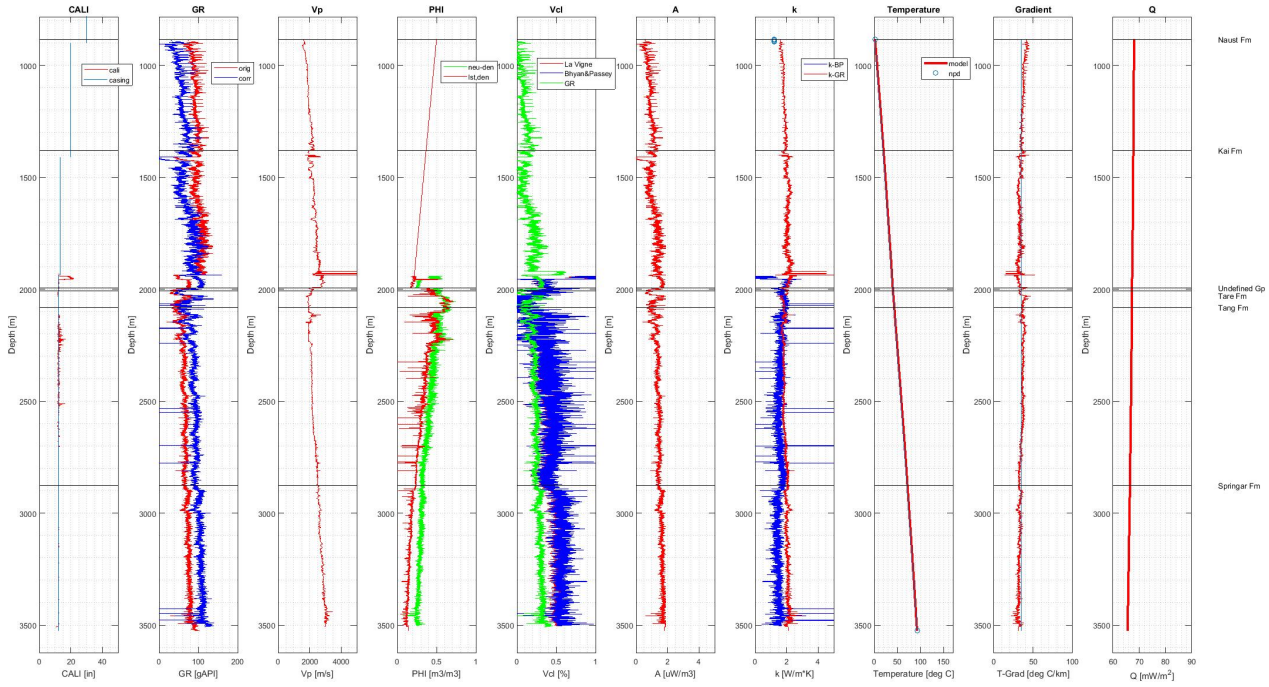

Figure 2.5: Temperature modelling for well 6607/2 – 1

6607/5-2

Well logs for well 6607/5−2 are shown on Figure 2.6. Here, GR seems to be overcorrected: it gives unreasonably high GR values at shallow depths. Within Naust Formation, A reaches 3 $\frac{\mu W}{m^3}$, which is typical for organic-rich shales in accordance with Hantschel and Kayerauf (2009). Moreover, the result is the opposite of what is seen in the neighbouring well 6607/2 – 1, where Naust Formation has relatively low GR. Using original GR instead of corrected one only has an effect on A log, it does not influence resulting HF and TG remarkably. In this way, it was decided to proceed with aforementioned methodology, but to treat these A values with caution. Comparing thermal conductivity values with Ritter et al. (2004), there is a difference of approximately 0.5 $\frac{W}{mK}$. However, it is hard to judge whether it is due to uncertainty in Ritter's measurements or erroneous shallowest GR log.

The well contains two sand layers of Late Cretaceous age, as well as two dolerite sills (Lyons and Millen). The remaining part mainly consists of shales. Thermal conductivity is increasing from 1.5 to 3 $\frac{W}{mK}$, while temperature gradient is decreasing from approximately 40 to 30 $\frac{^\circ C}{km}$. Exceptions from this trend are sands layers, which have k of about 3.5 and sills which seem to have elevated k. On the contrary, thermal conductivity for dolerite is expected to be between 1.5 and 2 $\frac{W}{mK}$ based on Hantschel and Kayerauf (2009). This means that the method used for k estimation is not optimal for magmatic intrusion rocks. However, after adjusting the sill intervals,

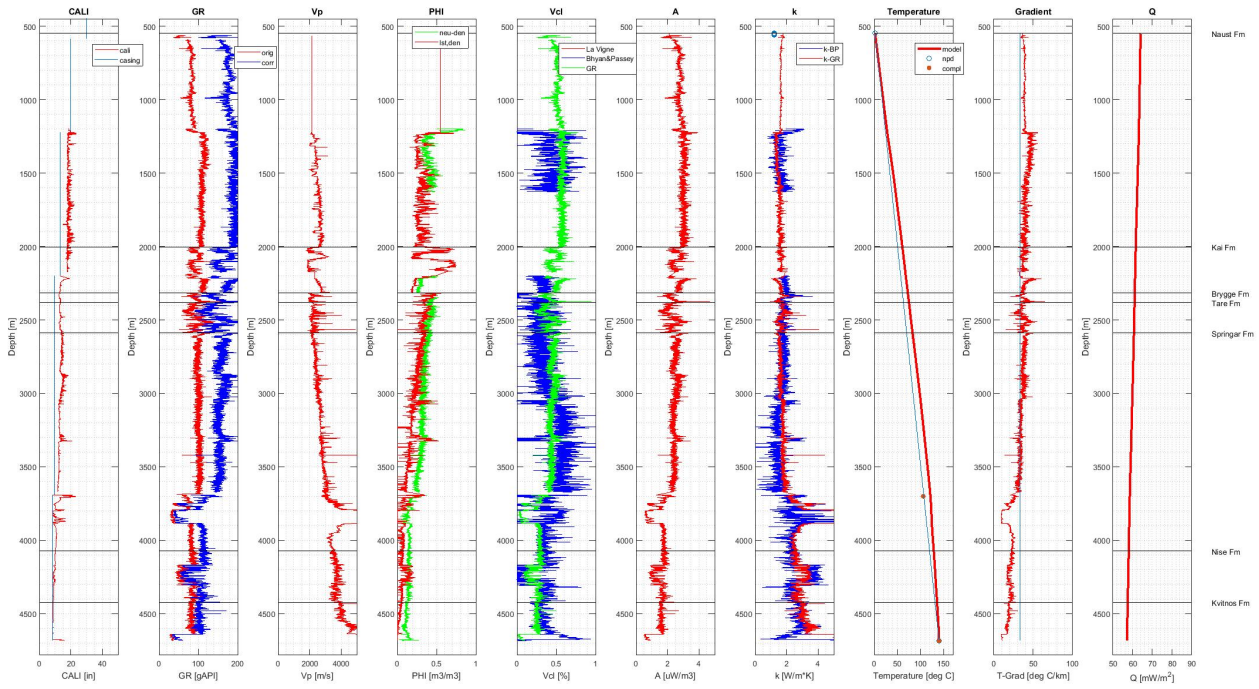

Figure 2.6: Temperature modelling for well 6607/5 – 2

temperature and heat flow profiles remain the same, as those rocks represent a small fraction of sediment column.

Notice that HF is calibrated with wellbore temperatures from CR (Lyons and Millen). Estimated heat flow in this case is 64 $\frac{mW}{m^2}$.

6609/5-1

The well is interpreted as mostly shale with exception of some thin layers in Early Cretaceous and some sands within Triassic sediments. Therefore, k and TG are rather monotonous with the average values 1.5-2 $\frac{W}{mK}$ and 30 $\frac{^\circ C}{km}$ accordingly, as can be seen on Figure 2.7. Thermal conductivity log has numerous peaks in Springar Formation and Red/Grey Beds and is reaching the values of 3.5 $\frac{W}{mK}$. At the same time, those values do not affect thermal gradient drastically as their thickness is insignificant. Consequently, estimated heat flow is 64 $\frac{mW}{m^2}$.

Even though average conductivity measurements from Ritter et al. (2004) are plotted for this well, there is little meaning in comparing those numbers with the modelled ones, as published measurements do not cover areas to the East of 8° parallel.

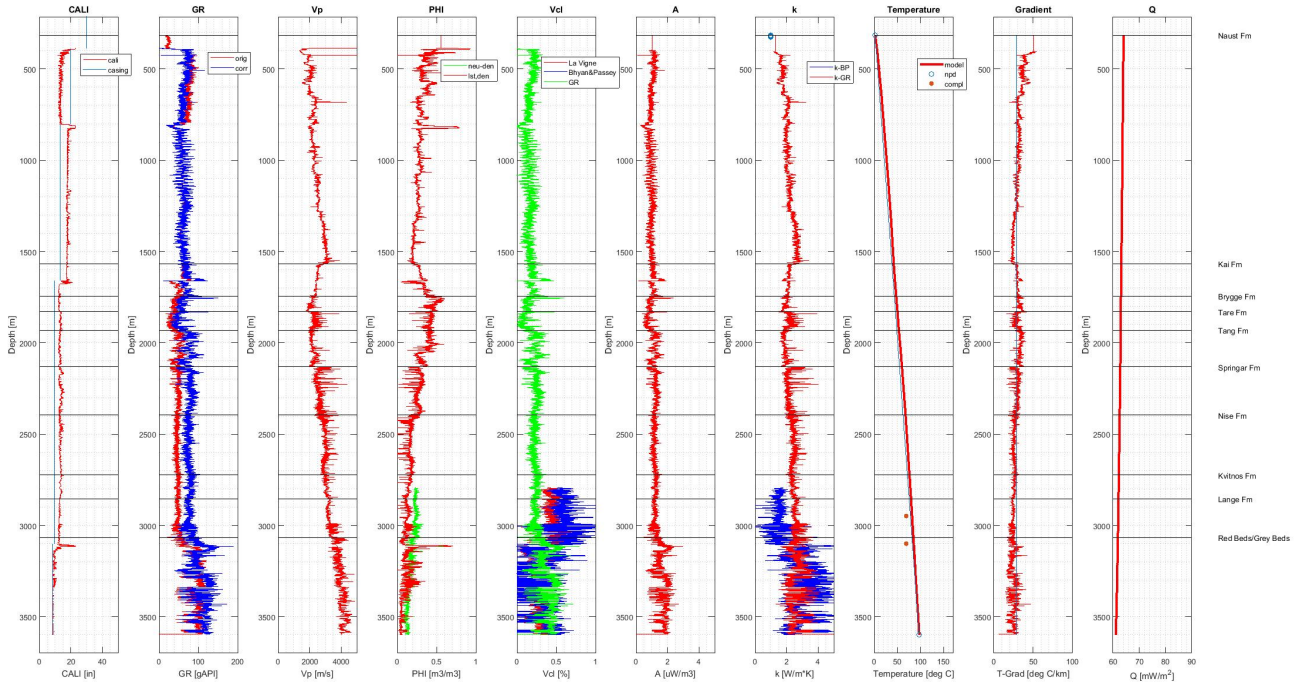

Figure 2.7: Temperature modelling for well 6609/5 – 1

6610/2-1S

Based on modelling shown on Figure 2.8, this well has sands in Lysing Formation in addition to Tilje Formation and Åre Formation. Due to that, k values for those formations are on average higher than for the rest of the well. Thermal conductivity for shale intervals is 2 $\frac{W}{mK}$, while Jurassic sands and sands of Tilje Formation reach k of 3 $\frac{W}{mK}$. Thermal gradient is varying between 45-40 $\frac{^\circ C}{km}$ for shales and 30 $\frac{^\circ C}{km}$ for the remaining lithologies.

When looking at the shallow Brygge Formation, corrected GR response indicates shale as a main lithology, however, according to CR (Alm et al. (1994)) there is an increase in N/G towards the seabed, and sand becomes dominant lithology above 800m. This does not correspond to GR response. It is hard to apply a consequent correction to fit the expected sand response, so it was decided to proceed with accepted methodology, while keeping in mind such incompatibilities when evaluating the results.

When HF is calibrated for CR temperatures and BHT, it becomes 80 $\frac{mW}{m^2}$.

6610/3-1R

Figure 2.9 shows the results for well 6610/3 – 1. Sediment column contains both sand and shale layers. There are 3 source rocks present: hot shales of Spekk Formation, shales of Melke For-

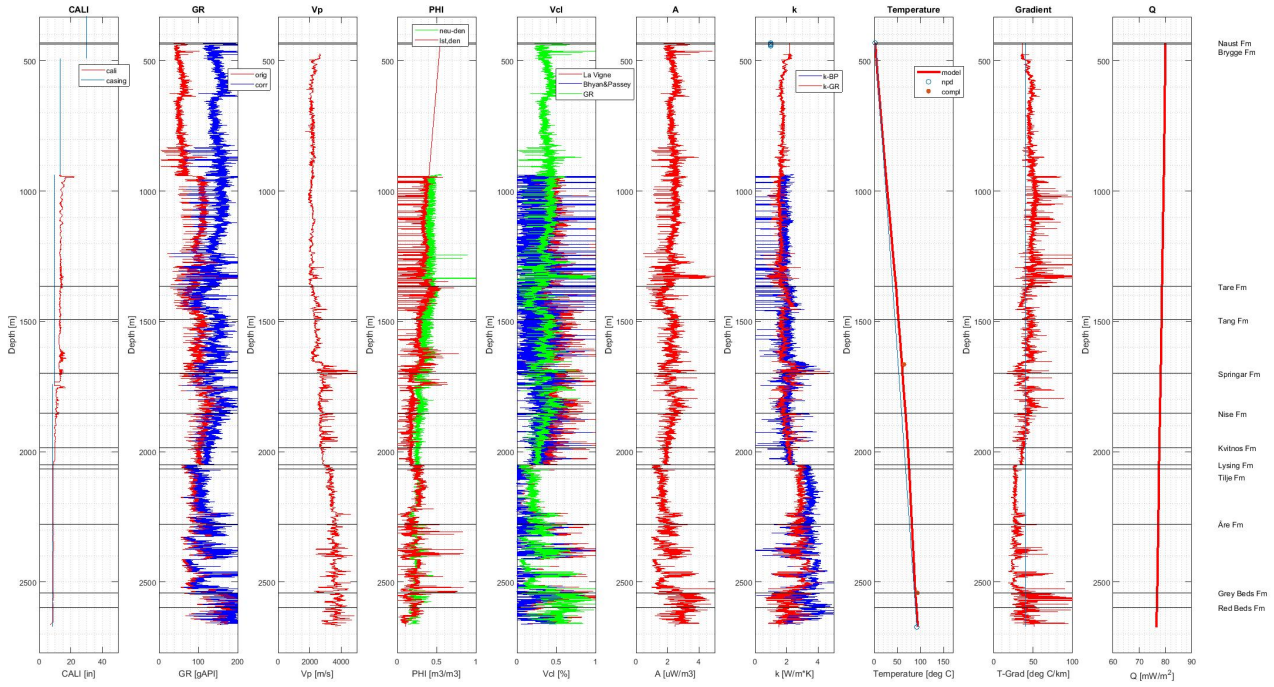

Figure 2.8: Temperature modelling for well 6610/2 – 1*S*

mation and coals of Åre Formation (Fristad et al.). Sands are located within Tang Formation and Nise Formation clays. There are also massive sandstone intervals within Lysing Formation and within Lange and Lyr Formation. Thin sands are also present in both Jurassic and Triassic sediments.

Most of the shales have thermal conductivity from 1.5 to 2 $\frac{W}{mK}$, while sands and mixed layers reach k of 3.5 $\frac{W}{mK}$. Thermal gradient with an average of 40 $\frac{^\circ C}{km}$ fluctuates between 60 for the more shaly intervals and 30 for the more sandy layers. Thermal gradient is very high for hot shale - over 70 $\frac{^\circ C}{km}$.

Heat flow is estimated to be 86 $\frac{mW}{m^2}$ in accordance with CR temperatures (Fristad et al.).

2.2 Discussion

An important issue to consider is the fact that estimated heat flow values are on average much higher than the ones measured in the area. For example, on the Gjallar Ridge surface heat flow from Ritter et al. (2004) does not exceed 62 $\frac{mW}{m^2}$. Close to well 6604/2 – 1 authors report 48 $\frac{mW}{m^2}$ and near well 6074/12 – 1 they measure 62 $\frac{mW}{m^2}$. Those values are significantly lower than the ones derived from the modelling. On the Nyk High Ritter's measurements show variation between 52 and 76 $\frac{mW}{m^2}$, while within the Någrind Syncline in the proximity of wells 6607/2 – 1

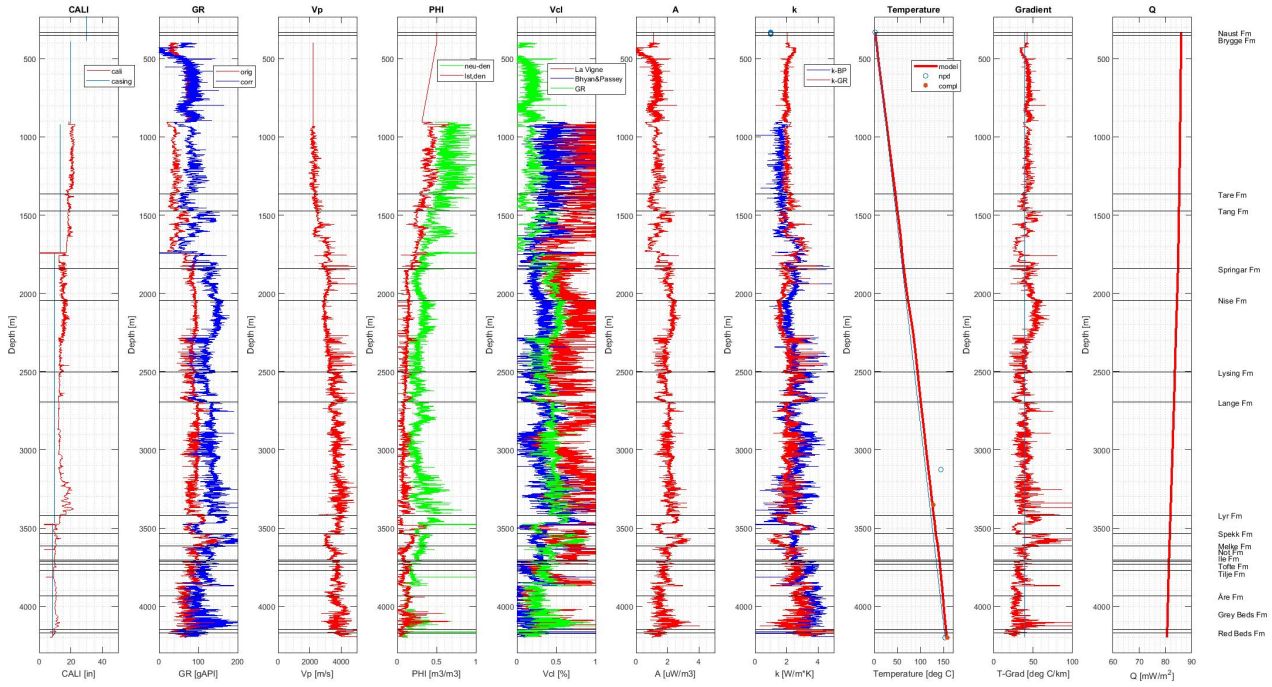

Figure 2.9: Temperature modelling for well $6610/3-1R$

and $66607/5-2$ the numbers are 47 and 75 $\frac{mW}{m^2}$. This trend is the opposite of what is proposed in this report, where surface heat flow is elevated on the Nyk High and depressed within the syncline.

Closs and Haenel (2003) propose HF of 67.4 $\frac{mW}{m^2}$ north of the Gjallar Ridge, which is also much lower than suggested in this work. Similar estimate is reported by Langseth and Zielinski (1974): surface heat flow is 41 $\frac{mW}{m^2}$ close to the Gjallar Ridge in the northern part of the Vigrid Syncline. Moreover, near well $6604/2-1$, Ocean Drilling Program site 644 shows average HF of 61 $\frac{mW}{m^2}$ (Eldholm et al. (1987).

Sundvor et al. (1989) measures heat flow of 53 $\frac{mW}{m^2}$ close to southern margin of the Utgard High, 65 and 74 $\frac{mW}{m^2}$ in the northern part of the Vigrid Syncline, and 70 and 67 $\frac{mW}{m^2}$ on the northern tip of the Gjallar Ridge. Those values are higher than presented by other authors, however, they are still low compared to the estimates proposed here.

What becomes evident, is that heat flow values vary significantly in different studies. This is likely to be caused by sensitivity of the results to exogenic factors such as water temperatures, submarine slides and sedimentation rate. Surface heat flow is also affected by thermal conductivities of seabed rocks which can vary from one site to another and cause rapid variation of HF measurements.

As conductivities used in this project are not computed in the lab for specific rock samples,

this represent a significant uncertainty when it comes to thermal modelling. With this in mind, it is important to see how sensitive the results are to changes in this variable.

2.2.1 Uncertainty

As mentioned previously, TG is very sensitive to bottom hole temperatures and rock conductivities. BHT was adopted from NPD homepages and completion reports, while k was estimated based on empirical formula by Duffaut et al. (2018) and well logs. A good method to quantify this uncertainty could be the Monte Carlo simulation. However, due to time constraints, a simpler and less scientific method was chosen. It is possible to calculate mean and standard deviation for conductivities of each formation and estimate upper and lower boundaries as $k - 1SD$ and $k + 1SD$. Figure 2.10 shows the result for well $6704/12 - 1$. If this is a good estimate for sensitivities, k uncertainty can reach a value of $\pm$ 0.43 $\frac{W}{mK}$. This leads to Q uncertainty of $\pm$ 13 $\frac{mW}{m^2}$. For simplicity, it can be assumed that the same values can be applied for the remaining wells.

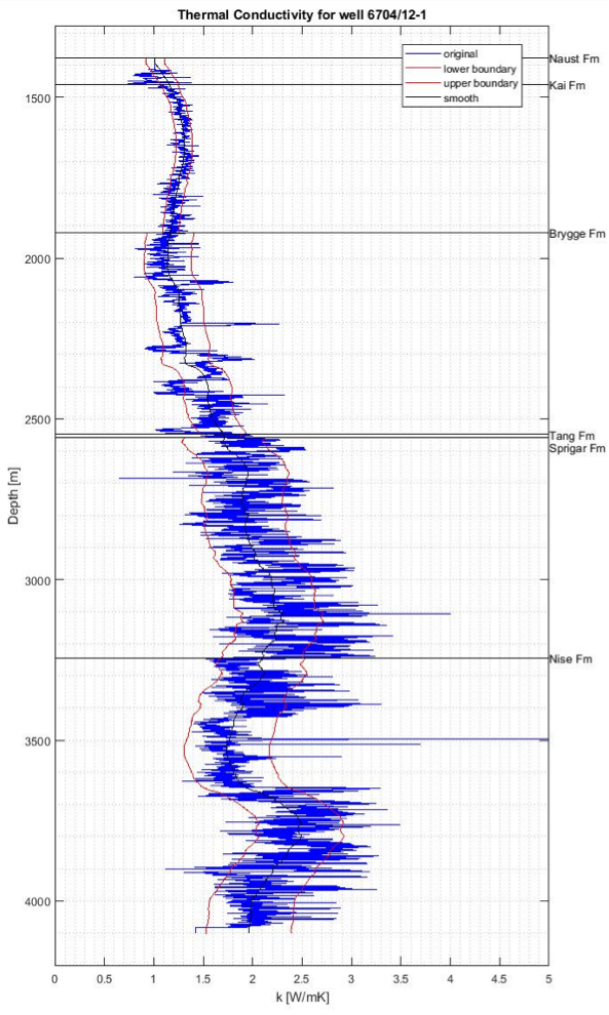

Figure 2.10: Thermal conductivity log and its boundaries for well 6704/12-1

2.2.2 Plots

Referring back to earlier sections of this report, parameters affecting thermal gradient are heat flow and rock conductivity. Moreover, heat flow incorporates several components: heat generated within sediments, heat generated within crust, and heat input from mantle.

Without further analysis it is possible to plot surface heat flow and thermal gradient along the profile to investigate if the trend is similar for both. Plots are oriented with North to the left, and indicated distance is measured along the line at Figure 1.2. Important to note that analysis is limited to a sediment column of 2249 m, as this corresponds to minimal

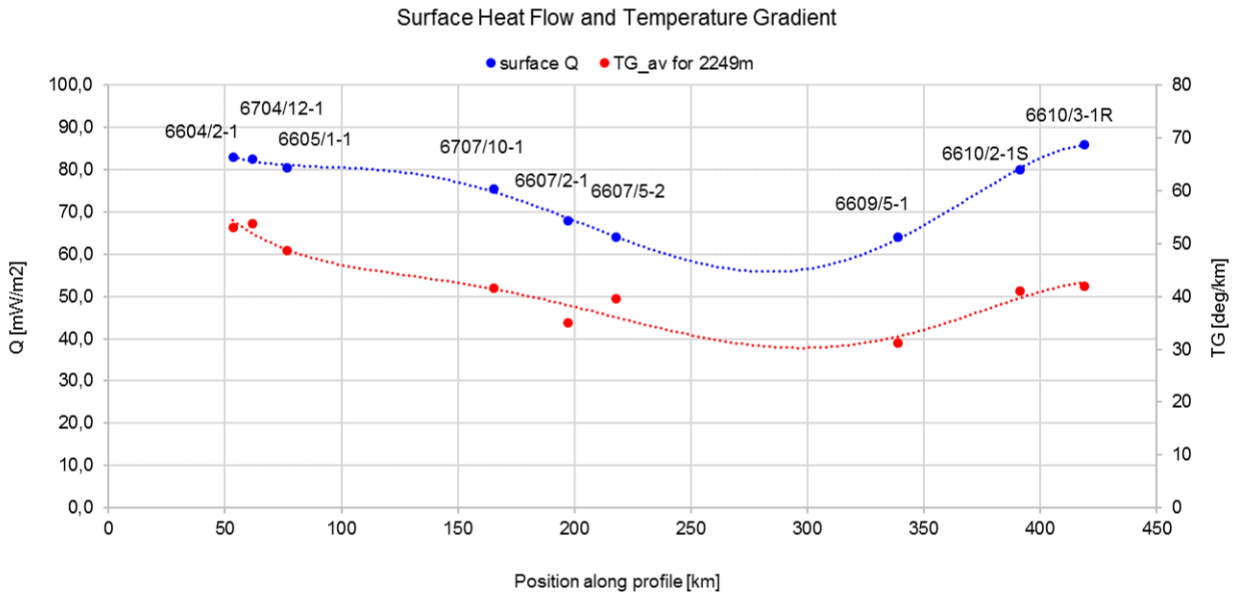

Figure 2.11: Surface heat flow and average temperature gradient for 2249m of sediments below the seabed, displayed along the profile

seabed - total depth among all the wells. As can be seen from Figure 2.11, where Q is elevated, TG is also relatively high, and where Q drops - TG follows. This is expected based on Equation 1.7. From the same relationship, correlation between $\frac{1}{k}$ and TG is anticipated. However, from Figure 2.12 the dependency is less apparent, which makes it possible to suggest that heat flow has the primary effect on the gradient.

Same analysis can be performed for radiogenic heat produced in sedimentary column. A along the profile is shown on Figure 2.13. Average value is around 1.5 $\frac{\mu W}{m^3}$, except for anomalously high values for well $6607/5-2$ and $6610/2-1S$, which were discussed in Section 2.1.1. Generally, A does not have such a large effect on thermal modelling results, so these unusual numbers can be ignored. In this way, taking A as 1.5 $\frac{\mu W}{m^3}$ for given depths, relationship between TG, k and Q can be investigated further.

Considering a possibility that heat flow estimates performed in this project are incorrect, and Q is constant in the area, it is possible to see what average thermal conductivities are required to match the existing temperature gradient.

Assuming surface heat flow of 64 $\frac{mW}{m^2}$ and A of 1.5 $\frac{\mu W}{m^3}$ it is possible to calculate new average temperature gradient for 2249 m of sediments. The result is shown on Figure 2.14 together with original average thermal gradient. It is clear that the difference is substantial in the areas of high heat flow, namely the Gjallar Ridge and north of the Trøndelag Platform. Figure 2.15 shows average thermal conductivities required to match the new temperature gradient. Uncertainty in k is also shown. Even with uncertainty, required k values are too low to reach the estimated thermal gradient. Moreover, conductivity values below 1.25 $\frac{W}{mK}$ are only viable for organic-rich shales (Hantschel and Kayerauf (2009), Allen and Allen (2013)), while sedimentary columns for

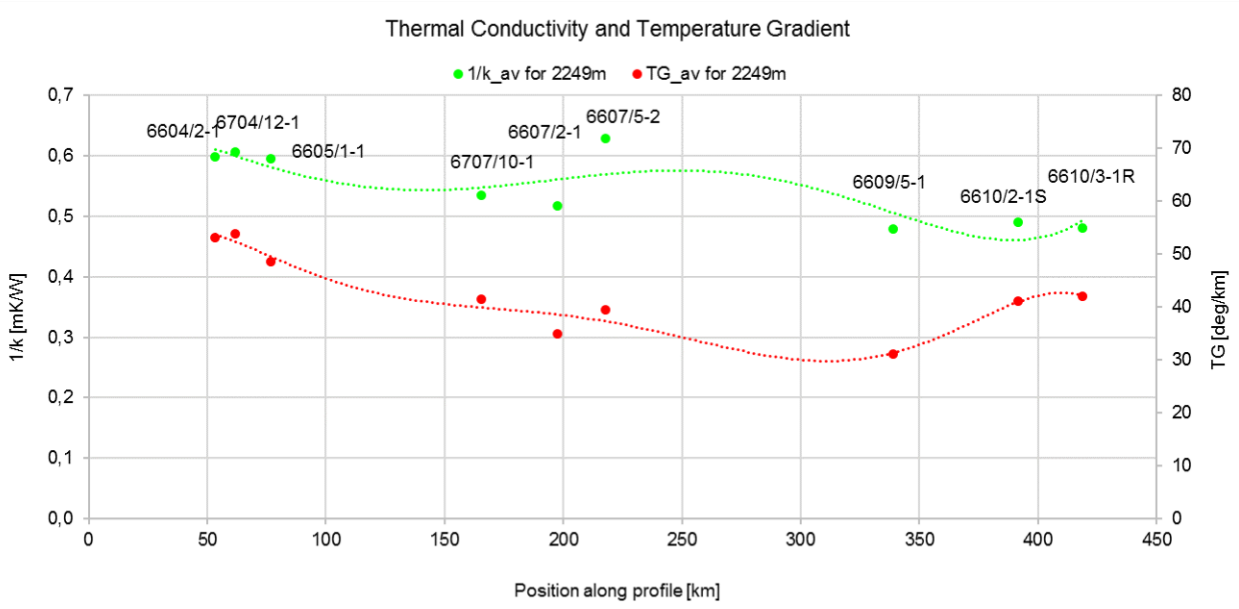

Figure 2.12: Average thermal conductivity and average temperature gradient for 2249m of sediments below the seabed, displayed along the profile

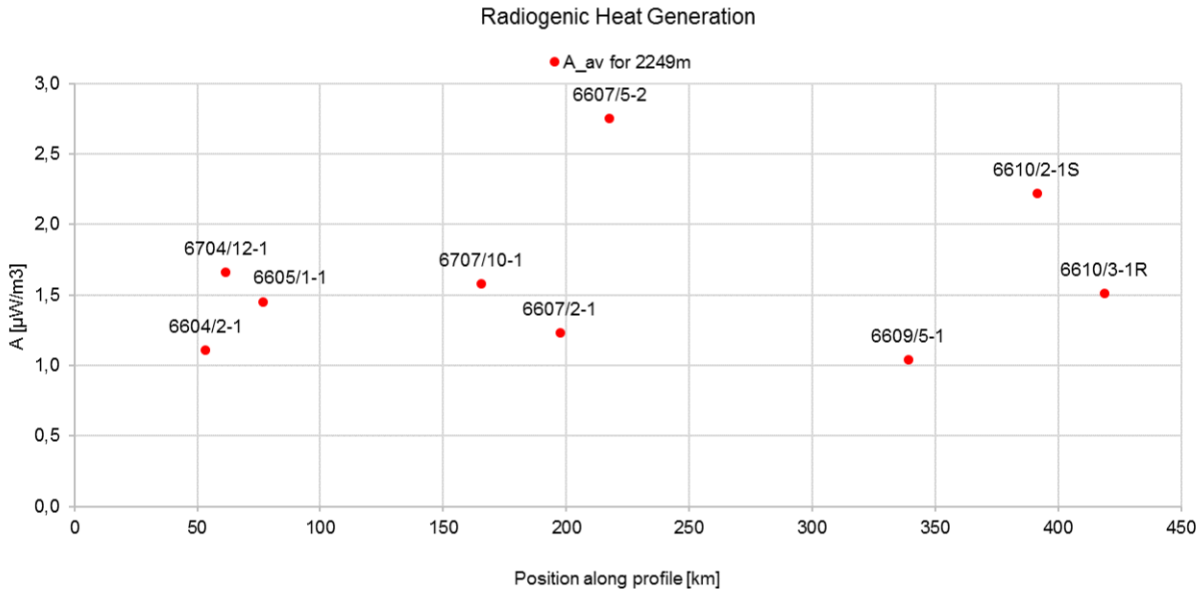

Figure 2.13: Radiogenic heat generation for 2249m of sediments below the seabed, displayed along the profile

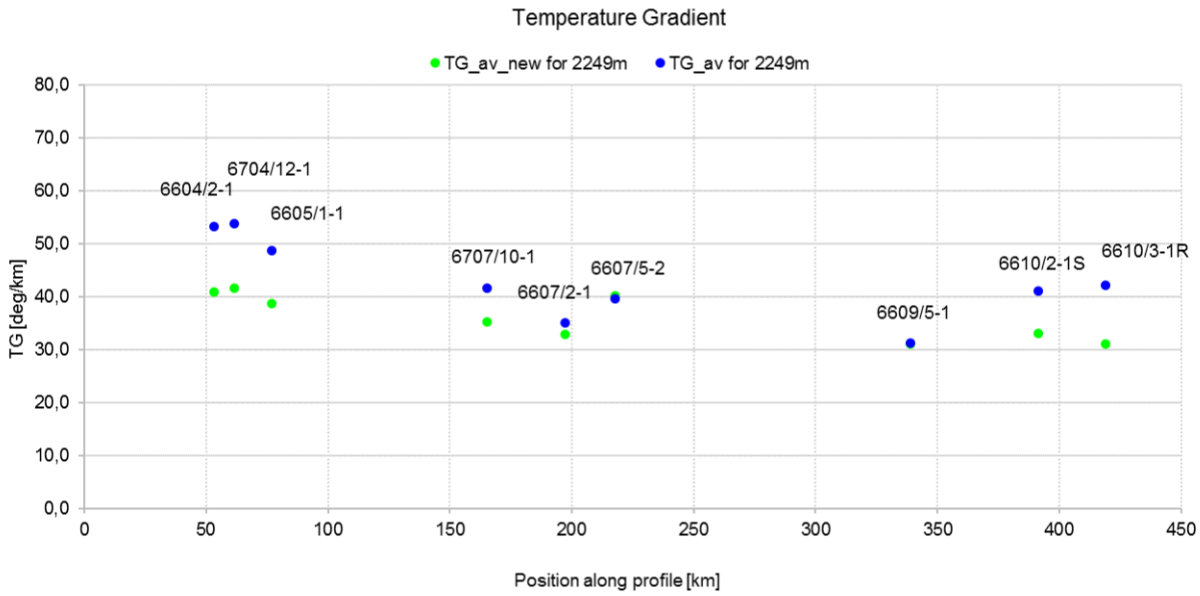

Figure 2.14: Original thermal gradient and new thermal gradient with $Q = 64 \frac{mW}{m^2}$ and $A = 1.5 \frac{\mu W}{m^3}$ for 2249m of sediments below the seabed, displayed along the profile

most of the wells consist of typical organic-lean shales and silty/shaly sandstones. At the same time, for eastern part of the cross section, conductivites required to fit the thermal gradient are around 1.5 $\frac{W}{mK}$, which are plausible. However, those wells are considered to be sand rich and such low k for more than 2 km of sediments remains unlikely.

2.2.3 Lithostragiraphic variations

Results of seismic interpretation are shown on Figure 2.16. Where basement is not interpreted, it is expected to be located at or deeper than Base Cretaceous reflector. Consequently, even though some packages seem to have substantial variations in thickness across the basin, it is unlikely to affect TG profile as proven by cross-plots. Moreover, basin infill thickness seem to have no correlation with heat flow values. For example, at the locations of well $6609/5-1$ and well $6610/2-1S$, sedimentary column is expected to be equally thick. However, their temperature gradient is very different as shown on Figure 2.11. Similarly, thermal anomaly along the Gjallar Ridge does not seem to be associated with shallow basement, as this is interpreted to be located relatively deep when compared to eastern margin of the basin.

2.2.4 Heat flow

Taking all information into consideration, it can be suggested that even though thermal conductivities estimated in this work remain the main uncertainty factor, heat flow has the primary effect on temperature gradient.

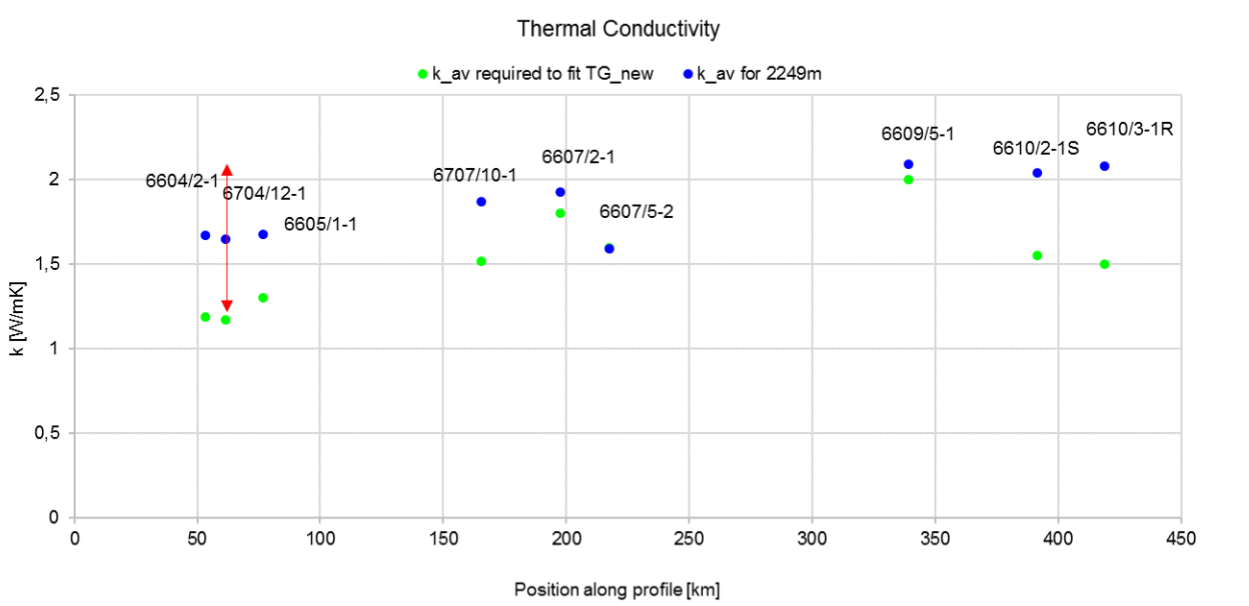

Figure 2.15: Original thermal conductivity (with uncertainty) and new thermal conductivity to fit the new thermal gradient for 2249m of sediments below the seabed, displayed along the profile

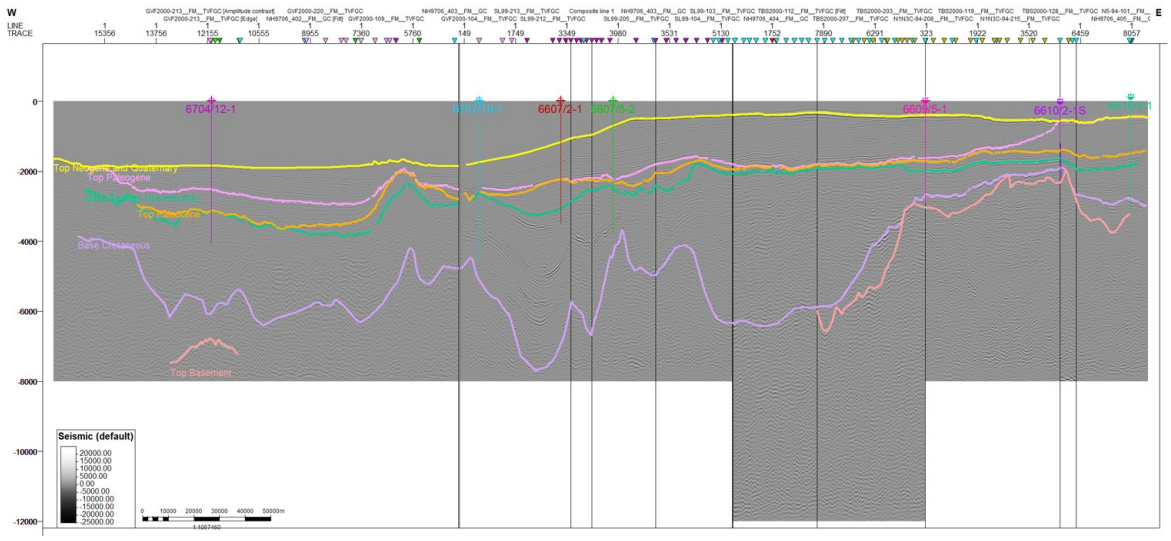

Figure 2.16: Composite seismic line interpretation

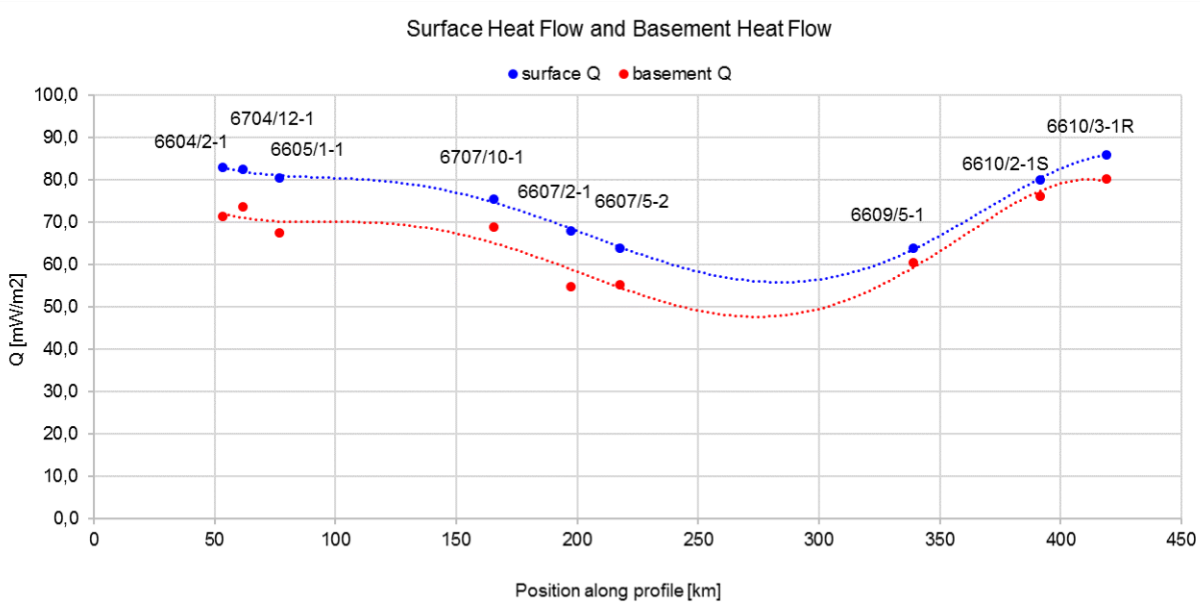

Figure 2.17: Heat flow at the Top Basement surface

Assuming A of 1.5 $[\frac{\mu W}{m^3}]$, k of 2 $\frac{W}{mK}$ and ϕ of 5 % heat flow can be interpolated to Top Basement depth. Interpreted basement location is converted from time to depth based on average V_p from well logs and V_p of 4000 $\frac{m}{s}$ below TD.

Figure 2.17 presents the estimated heat flow input from basement to sediments. Looking at the plots, it can be concluded that HF trend prevails with depth.

Chapter 3

Conclusions and recommendations for further work

3.1 Summary and conclusions

Analysis shows that there is no connection between sedimentary column thickness and temperature gradient. Furthermore, lithological composition across the section does not have primary effect on temperature gradient, even though it affects the values to some extent. The main cause for elevated thermal gradient is high heat flow values.

Estimated surface heat flow at the Gjallar Ridge is above 80 $\frac{mW}{m^2}$, which brings average gradient for 2249 m of sediments close to 50 $\frac{^\circ C}{km}$. On the opposite margin of the basin, surface HF also reaches values of 80 $\frac{mW}{m^2}$. For those wells, TG is still relatively high, but much lower than the one at the Gjallar Ridge. This is related to differences in rock conductivites, which is specified by lithology type. Lower HF and TG levels are expected at the center of the basin, according to the trends shown on Figure 2.11.

It is important to mention that heat flow estimates in this work are much higher than indicated by other literature. However, many works such as article by Ritter et al. (2004) and study by Pascal (2015) observe that heat flow is lowest at the centers of the basins and highest at the local highs. This conclusion is similar to what this project conveys.

This verdict is only valid if methods and formulas used for the thermal analysis are correct. Sensitivity in k remains to be an important issue. A rough analysis in Section 2.2.1 showed that while uncertainty in k for well 6704/12 – 1 is about 0.43 $\frac{W}{mK}$, uncertainty in Q becomes 13 $\frac{mW}{m^2}$. If same reasoning can be applied for other wells across the section, the results can be questioned. However, with the exception of some shallow intervals, modelled k logs are in a good agreement with expected shale and sand conductivites as presented by Hantschel and Kayerauf (2009). This is a convincing argument for vailidity of the results. Another important remark is that temperatures used for calibration are based on combination of values given by NPD and Completion

Reports. Wells on the Gjallar Ridge, for example, only had available NPD temperatures, which could be uncorrected. However, the fact that adjusting for mud effect usually gives even higher numbers, makes it safe to assume that those temperatures are accurate. Large part of the remaining wells had available completion reports, where BHT temperatures were given, however, it is still unclear whether the temperatures are revised. Only for well 6707/10 – 1 it was explicitly stated that the temperatures are corrected. This fact remains to be an important question when it comes to reliability of the estimates.

3.2 Recommendations for further work

Given the main conclusion of this work, which states that primary cause of varying temperature gradient is heat flow input from basement, it is essential to consider whether or not it is possible and what causes the deviation of heat flow levels at the top basement surface. Theoretically, this can either be related to differences in heat generation within basement rocks or fluctuations of mantle heat flow.

This phenomenon can be investigated by studying gravity and magnetic data to build a model of crustal composition. As for sedimentary rocks, crystalline rocks have different facies and therefore different characteristics. According to Slagstand (2008), who studied properties of Archean and Permian geological provinces onshore Norway, mafic rocks generate much less heat when compared to granitic rocks. Resolving basement rock properties for the Vøring Basin can be used to correlate offshore and onshore bedrock types, which in its turn may be used to build a thermal model of the deepest parts of the Vøring Basin.

In this way, this project is intended to be continued as master thesis in Spring 2019. The plan is to integrate gravity and magnetic data together with seismics in order to perform a study of the deepest parts of the basin, as well as revisit seismic interpretation of the shallower intervals. This will help to extent the thermal modelling to crustal levels and will give an insight into what causes the heat flow variations.

Bibliography

AAPG. Densitu-neutron log porosity. https://wiki.aapg.org/Density-neutron_log_porosity. Last Accessed: 2018-22-12.

Allen, P. A. and Allen, J. R. (2013). *Basin Analysis, Principles and Application to Petroleum Play Assessment*. Wiley-Blackwell, 3rd edition.

Alm, D., Møgster, T., and Jenssen, L. (1994). Completion report. well 6610/2-1s. chrome-extension://oemmndcbldboiebfnladdacbdfmadadm/http://www.npd.no/engelsk/cwi/pbl/wellbore_documents/2874_6610_2_1_S_COMPLETION_REPORT_AND_COMPLETION_LOG.pdf. Last Accessed: 2018-28-12.

Asquith, G. B. and Gibson, C. R. (1982). *ME3: Basic Well Log Analysis for Geologists*. AAPG Publications, Tulsa, Oklahoma.

Bhuyan, K. and Passey, Q. (1994). Clay estimation from gr and neutron-density porosity logs. *SPWLA 35th Annual Logging Symposium, Society of Petrophysicists and Well-Log Analysts*.

Brekke, H. (2000). The tectonic evolution of the norwegian sea continental margin with emphasis on the vøring and møre basins. *Geological Society London Special Publications*, 167(1):327–378.

Bücker, C. and Rybach, L. (1996). A simple method to determine heat production from gamma-ray logs. *Marine and Petroleum Geology*, pages 373–375.

Closs, H. and Haenel, R. (2003). Thermal conductivity and heat flow measurements from cruise planet69, 4-21 august 1969, norwegian sea. https://doi.org/10.1594/PANGAEA.112756. Last Accessed: 2018-22-12.

Crain, E. R. (2015). Shale volume from gamma ray log models. https://www.spec2000.net/11-vshgr.htm. Last Accessed: 2018-26-12.

Duffaut, K., Hokstad, K., Kyrkjebø, R., and Wiik, T. (2018). A simple relationship between thermal conductivity and seismic interval velocity. *The Leading Edge*, pages 381–385.

Ebbing, J., Gernigon, L., Pascal, C., Oleseb, O., and Osmundsen, P. T. (2009). A discussion of structural and thermal control of magmatic anomalies on the mid-norwegian margin. *Geophysical Prospecting*, 57:665–681.

Eldholm, O., Thiede, J., Taylor, E., and et.al. (1987). Proceedings of the ocean drilling program. 104:617–747.

Fristad, P., Pettersen, R. M., and Finnesen, L. Completion report. well 6610/3-1 3-1r. chrome-extension://oemmndcbldboiebfnladdacbdfmadadm/http://www.npd.no/engelsk/cwi/pbl/wellbore_documents/1864_6610_3_1_COMPLETION_REPORT_AND_LOG.pdf. Last Accessed: 2018-28-12.

Haenel, R. (1974). Heat flow measurements in the norwegian sea. *Meteor Forschungsergebnisse, Deutsche Forschungsgemeinschaft, Reihe C Geologie und Geophysik*, C17:74–78.

Halland, E. K., Johansen, W. T., and Riis, F. (2013). *CO2 Storage Atlas, Norwegian Sea*. Norwegian Petroleum Directorate, P.O. Box 600 NO-4003 Stavanger.

Hantschel, T. and Kayerauf, A. I. (2009). *Fundamentals of Basin and Petroleum Systems Modeling*. Springer, Hoboken, NJ, 1st edition.

La Vigne, J., Herron, M., and Hertzog, R. (2018). Density-neutron interpretation in shaly sands. *SPWLA 35th Annual Logging Symposium, Society of Petrophysicists and Well-Log Analysts*, pages 381–385.

Langseth, G. M. and Zielinski, G. W. (1974). Marine heat flow measurements in the norwegian-greenland sea and in the vicinity of iceland. *Geodynamics of Iceland and the North Atlantic area: proceedings of the NATO Advanced Study Institute held in Reykjavik, Iceland, Reidel Verlag*, pages 277–295.

Lyons, R. J. and Millen, R. V. Geological completion report. well 6607/5-2. chrome-extension://oemmndcbldboiebfnladdacbdfmadadm/http://www.npd.no/engelsk/cwi/pbl/wellbore_documents/1789_6607_5_2_COMPLETION_REPORT.pdf. Last Accessed: 2018-22-12.

Maystrenko, Y. P., Gernigon, L., Olesen, O., Ottesen, D., and Rise, L. (2018). 3-d thermal effect of late cenozoic erosion and deposition within the lofoten-vesterålen segment of the mid-norwegian continental margin. *Geophysical Journal International*, 213:885–918.

NPD. Well 6604/2-1, general information. http://factpages.npd.no/ReportServer?/FactPages/PageView/wellbore_exploration&rs:Command=Render&rc:Toolbar=false&rc:Parameters=f&NpdId=6568&IpAddress=129.241.64.249&CultureCode=nb-no. Last Accessed: 2018-22-12.

NPD. Well 6707/10-1, general information. http://factpages.npd.no/ReportServer?/FactPages/PageView/wellbore_exploration&rs:Command=Render&rc:Toolbar=false&rc:Parameters=f&NpdId=3075&IpAddress=85.142.208.223&CultureCode=en. Last Accessed: 2018-28-12.

Pascal, C. (2015). Heat flow of norway and its continental shelf. *Marine and Petroleum Geology*, 66:956–969.

Peltonen, C., Øyvind Marcussem, Bjørlykke, K., and Jahren, J. (2008). Mineralogical control on mudstone compaction: a study of late cretaceous to early tertiary mudstones of the vøring and møre basins, norwegian sea. *Petroleum Geoscience*, 14:127–138.

Ritter, U., Zielisnki, G. W., Weiss, H. M., Zielinski, R. L., and Sættem, J. (2004). Heat flow in the vøring basin, mid-norwegian shelf. *Petroleum Geoscience*, 10(4):353–365.

Rydningen, H. and Cade, C. Geological completion report. well 6707/10-1. http://www.npd.no/engelsk/cwi/pbl/wellbore_documents/3075_6707_10_1_COMPLETION_REPORT_GEOLOGY.pdf. Last Accessed: 2018-22-12.

Slagstand, T. (2008). Radiogenic heat production of archean to permian geological provinces in norway. *Norwegian Journal of Geology*, 88:149–166.

Sundvor, E., Myhre, A. M., and Eldholm, O. (1989). Heat flow measurements on the norwegian continental margin during the flunorge project. *University of Bergen, Seismological Observatory, Seismo-series No .27*.

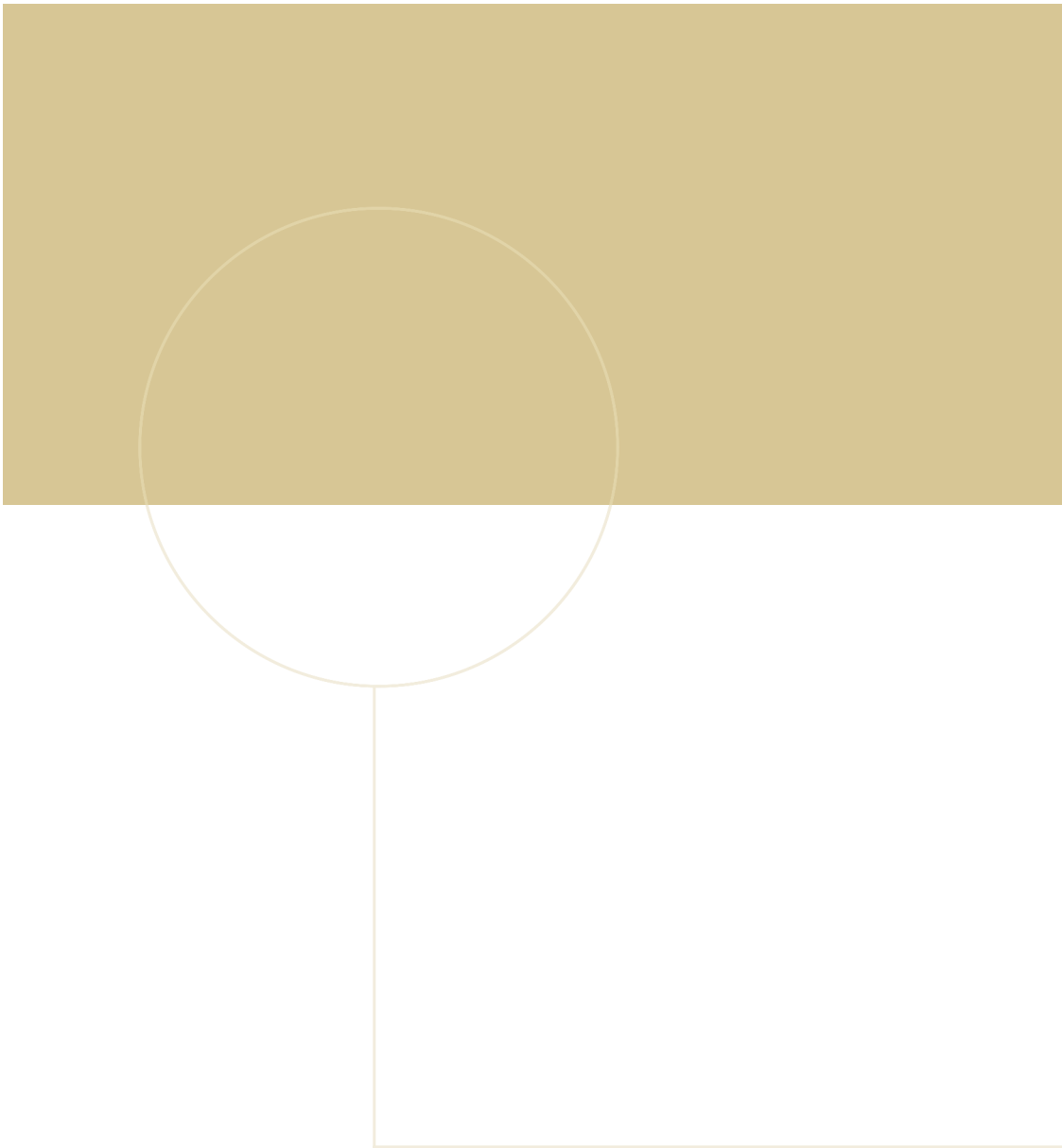

NTNU
Norwegian University of
Science and Technology